

ISSN en trámite



Geofísica Internacional

Revista Trimestral Publicada por el Instituto de Geofísica de la
Universidad Nacional Autónoma de México



México

Volume 51 Number 4
October - December
2012

— Geofísica Internacional —

Dr. José Francisco Valdés Galicia
Director of Instituto de Geofísica

Dr. Avto Gogichaishvili
President of Unión Geofísica Mexicana

Editor Chief

Dr. Servando De la Cruz-Reyna
Instituto de Geofísica, UNAM
sdelacrr@geofisica.unam.mx

Technical Editor

Mtra. Andrea Rostan Robledo
Instituto de Geofísica, UNAM
arostan@igeofisica.unam.mx

Editorial Board

Donald Bruce Dingwell
Earth and Environment
Ludwig Maximilian University of Munich,
Germany

Eric Desmond Barton
Departamento de Oceanografía
Instituto de Investigaciones Marinas, Spain

Jorge Clavero
Amawta Consultores, Chile

Gerhardt Jentzsch
Institut für Geowissenschaften
Friedrich-Schiller-Universität Jena, Germany

Peter Malischewsky
Institut für Geowissenschaften
Friedrich-Schiller-Universität Jena, Germany

François Michaud
Géosciences Azur
Université Pierre et Marie Curie, France

Olga Borisovna Popovicheva
Scobeltzine Institute of Nuclear Physics
Moscow State University, Rusia

Jaime Pous
Facultad de Geología
Universidad de Barcelona, Spain

Joaquín Rui
UA Science
University of Arizona, United States

Angelos Vourlidis
Solar Physics Branch
NASA Goddard Space Flight Center, United States

Théophile Ndougsa Mbarga
Department of Physics
University of Yaounde I, Cameroon

Associate Editors
José Agustín García Reynoso
Atmospheric Science Centro de Ciencias de la
Atmósfera UNAM, Mexico

Tereza Cavazos
Atmospheric Science
Departamento de Oceanografía Física CICESE,
Mexico

Dante Jaime Morán-Zenteno
Geochemistry
Instituto de Geología, UNAM, Mexico

Margarita López
Geochemistry
Instituto de Geología UNAM, Mexico

Avto Gogichaisvili
Geomagnetism And Paleomagnetism
Instituto de Geofísica UNAM, Mexico

Jaime Urrutia-Fucugauchi
Geomagnetism And Paleomagnetism
Instituto de Geofísica, UNAM, Mexico

Felipe I. Arreguín Cortés
Hydrology
Instituto Mexicano de Tecnología del Agua IMTA,
Mexico

William Lee Bandy
Marine Geology And Geophysics
Instituto de Geofísica UNAM, Mexico

Fabian García-Nocetti
**Mathematical And Computational
Modeling**
Instituto de Investigaciones en Matemáticas
Aplicadas y en Sistemas UNAM, Mexico

Graciela Herrera-Zamarrón
Mathematical Modeling
Instituto de Geofísica, UNAM, Mexico

Ismael Herrera Revilla
**Mathematical And Computational
Modeling**
Instituto de Geofísica UNAM, Mexico

Rene Chávez Segura
Near-Surface Geophysics
Instituto de Geofísica UNAM, Mexico

Juan García-Abdeslem
Near-Surface Geophysics
División de Ciencias de la Tierra CICESE, Mexico

Alec Torres-Freyermuth
Oceanography
Instituto de Ingeniería, UNAM, Mexico

Jorge Zavala Hidalgo
Oceanography
Centro de Ciencias de la Atmósfera UNAM,
Mexico

Shri Krishna Singh
Seismology
Instituto de Geofísica, UNAM, Mexico

Xyoli Pérez-Campos
Seismology
Servicio Sismológico Nacional, UNAM, Mexico

Blanca Mendoza Ortega
Space Physics
Centro de Ciencias de la Atmósfera, UNAM,
Mexico

Inez Staciari Batista
Space Physics
Pesquisador Senior Instituto Nacional de Pesquisas
Espaciais, Brazil

Roberto Carniel
Volcanology
Laboratorio di misure e trattamento dei segnali
DPIA - Università di Udine, Italy

Miguel Moctezuma-Flores
Satellite Geophysics
Facultad de Ingeniería, UNAM, Mexico

Assistance

Elizabeth Morales Hernández,
Management
eliedit@igeofisica.unam.mx



GEOFÍSICA INTERNACIONAL, Año 51, Vol. 51, Núm. 4, octubre - diciembre de 2012 es una publicación trimestral, editada por la Universidad Nacional Autónoma de México, Ciudad Universitaria, Alcaldía Coyoacán, C.P. 04150, Ciudad de México, a través del Instituto de Geofísica, Circuito de la Investigación Científica s/n, Ciudad Universitaria, Alcaldía Coyoacán, C.P. 04150, Ciudad de México, Tel. (55)56 22 41 15. URL: <http://revistagi.geofisica.unam.mx>, correo electrónico: revistagi@igeofisica.unam.mx. Editora responsable: Andrea Rostan Robledo. Certificado de Reserva de Derechos al uso Exclusivo del Título: 04-2022-081610251200-102, ISSN: en trámite, otorgados por el Instituto Nacional del Derecho de Autor (INDAUTOR). Responsable de la última actualización Saúl Armendáriz Sánchez, Editor Técnico. Fecha de la última modificación: 30 de septiembre 2012, Circuito de la Investigación Científica s/n, Ciudad Universitaria, Alcaldía Coyoacán, C.P. 04150, Ciudad de México.

El contenido de los artículos es responsabilidad de los autores y no refleja el punto de vista de los árbitros, del Editor o de la UNAM. Se autoriza la reproducción total o parcial de los textos siempre y cuando se cite la fuente completa y la dirección electrónica de la publicación.



Esta obra está bajo una Licencia Creative Commons Atribución-NoComercial-SinDerivadas 4.0 Internacional.

Contents

- Characterization of a leachate contaminated site integrating geophysical and hydrogeological information.
Salvador I. Belmonte-Jiménez, Martha E. Jiménez-Castañeda, Marco A. Pérez-Flores, José O. Campos-Enríquez, Jaime A. Reyes-López, Leobardo Salazar-Peña 309
-
- Looking for active faults at east Qattara depression, northwestern desert, Egypt.
Taha Rabeih 323
-
- Declining productivity in geothermal wells as a function of the damage effect.
Alfonso Aragón-Aguilar, Georgina Izquierdo-Montalvo, Víctor Arellano-Gómez, Mahendra P. Verma, Ma. Guadalupe Belín-Morales 339
-
- Applicability of attenuation relations for regional studies.
Anand Joshi, Ashvini Kumar, Cinna Lomnitz, Heriberta Castaños 349
-
- Hydrostratigraphy of Haftad Gholle Karst, Markazi province, Iran, optimized by Fuzzy Logic.
Mostafa Yousefi Rad 365
-
- Viscoelastic modeling and factor Q for reflection data.
Vladimir Sabinin 377
-

Gas Hydrates in the southern Jalisco subduction zone as evidenced by bottom simulating reflectors in Multichannel Seismic Reflection Data of the 2002 BART/FAMEX campaign.

William L. Bandy, Carlos A. Montera-Gutiérrez

Characterization of a leachate contaminated site integrating geophysical and hydrogeological information

Salvador I. Belmonte-Jiménez*, Martha E. Jiménez-Castañeda, Marco A. Pérez-Flores, José O. Campos-Enríquez, Jaime A. Reyes-López and Leobardo Salazar-Peña

Received: September 30, 2010; accepted: April 18, 2012; published on line: September 28, 2012

Resumen

Se reporta en este estudio la caracterización de una zona contaminada por lixiviados, siguiendo una metodología que integra datos geofísicos y geohidrológicos para proponer un modelo hidrogeológico del fenómeno. La caracterización del sitio (la estructura del subsuelo, y las características del suelo) incluyó seis perfiles sísmicos de refracción, tres líneas electromagnéticas (FDEM), dos perfiles eléctricos (ERT), cinco sondeos eléctricos verticales (SEV), y una serie de pruebas geohidrológicas para delimitar la pluma contaminante. El área de estudio corresponde a la laguna de lixiviados del relleno sanitario de la ciudad de Oaxaca, sur de México. El modelo hidrogeológico que se presenta constituye un ejemplo del potencial de la integración de varios métodos aplicados con el mismo objetivo; reduciendo así la ambigüedad de la respuesta geofísica. Los resultados indican que los valores de baja resistividad (1.5 a 2.5 Ohm-m) se relacionan con un suelo contaminado subyaciendo a la laguna de lixiviados y al medio fracturado. También se detectó un desplazamiento de la pluma contaminante hacia el SW de la laguna. La calidad del agua es buena, pero la actividad humana en el área de estudio confiere un riesgo para el acuífero superficial de Zaachila.

Palabras clave: lixiviados, prospección geofísica, caracterización hidrogeológica.

S.I. Belmonte-Jiménez*
Centro Interdisciplinario de Investigación
para el Desarrollo Integral Regional (CIIDIR-Oaxaca)
Instituto Politécnico Nacional
Hornos 1003, Colonia Noche Buena
Sta. Cruz Xoxocotlán C.P. 71230
Oaxaca, México
Corresponding author: sbelmont@prodigy.net.mx

M.E. Jiménez-Castañeda
Posgrado en Aprovechamiento
y Conservación de Recursos Naturales
Centro Interdisciplinario de Investigación
para el Desarrollo Integral Regional (CIIDIR-Oaxaca)
Instituto Politécnico Nacional
Oaxaca, México.

M.A. Pérez Flores-Flores
Centro de Investigación Científica
y de Educación Superior de Ensenada
Baja California, México.
E-mail: mperez@cicese.mx

Abstract

In this study we report the characterization of a leachate contaminated site, by following a methodology that integrates geophysical and hydrogeological data to better constrain a hydrogeological model. The characterization of the site (subsurface structure, soil characteristics) included six seismic refraction profiles, three electromagnetic lines using transient domain electromagnetic soundings (TDEM), two electric resistivity tomography (ERT) profiles, five vertical electrical sounding (VES) and hydrogeological testings and analysis to support the delimitation of the contaminant plume. The study area corresponds to the leachate lagoon of Oaxaca City landfill, southern Mexico. Its inferred hydrogeological model constitutes an example of the usefulness of the integration of several diverse methods applied with the same objective, thus reducing the ambiguity of applying a single characterization technique. The results indicate that low resistivity values from 1.5 to 2.5 Ohm-m are related to a leachate polluted soil underlying the leachate lagoon and also associated with an anomaly enclosed in the rockbed. A displacement of the polluted plume to the SW from the lagoon was also detected. Water quality is quite good but the human activity in the study area confers a risk to the Zaachila aquifer.

Key words: Leachate, geophysical surveys, hydrogeological characterization.

J.O. Campos-Enríquez
Departamento de Geomagnetismo y Exploración
Instituto de Geofísica
Universidad Nacional Autónoma de México
México D.F.
E-mail: ocampos@geofisica.unam.mx

J.A. Reyes-López
Instituto de Ingeniería.
Universidad Autónoma de Baja California, Mexicali.

L. Salazar-Peña
Escuela Superior de Ingeniería y Arquitectura
Unidad Ticomán
Instituto Politécnico Nacional

Introduction

Landfill leachates constitute a potential form of water pollution. Their effect on the environment has been documented in several studies (Williams *et al.*, 2000; Sun *et al.*, 2001; Porsania *et al.*, 2004; Feng *et al.*, 2007). However there exist many geologically inadequate landfills which increase the vulnerability of the surrounding sites (Bengtsson *et al.*, 1994).

The assessment of soil and water properties is important to characterise leachate impact (Nobes, 1996; Fatta *et al.*, 1999; Rosqvist *et al.*, 2003; Kumar and Alappat, 2005). Drilling is a direct method to obtain data but is punctual and expensive. On contrary, geophysical methods cover larger areas and are relatively inexpensive. Electrical and electromagnetic methods are frequently used in groundwater applications (Atekwana *et al.*, 2000; Buselli and Lu, 2001; Yoon and Park, 2001; Inman *et al.*, 2002; Rosqvist *et al.*, 2003; De la Vega *et al.*, 2003; Chandra *et al.*, 2004; Corwin and Lesch, 2005 a, b; Owen *et al.*, 2005; Bauer *et al.*, 2006; Asfahani, 2007). However, better results of geophysical methods are obtained by applying jointly methods which are supplementary with respect to their sensitivity to the physical properties of interest.

In this study we have integrated three geophysical methods (seismic refraction, electro-

magnetic induction and electric resistivity) with hydrological parameters to obtain a robust model of the leachate lagoon of Oaxaca City landfill.

Our objective is to characterise this site since recently has been populated and inhabitants have drilled wells with the risk represented by not knowing the water quality.

Materials and methods

Study site

The Oaxaca city Landfill, located at Zaachila receives 550 ton/day of waste (Figure 1). As result of waste weatering, a leachate stream have been flow down to a leachate lagoon for more than 25 years. The so called "leachate lagoon" is a structure constructed 1.8 km from the landfill as a oxidating pond, but with the opening of the landfill the flowing water have transported toxic substances that made of the pond a highly polluted site.

The area surrounding the leachate lagoon is composed by granular alluvial material and fractured sedimentary rocks such as sandstone and shale, that enable leachate infiltration to the subsoil (Belmonte *et al.*, 2005). Another important feature to consider is the presence of the Oaxaca Fault (N10W) in the Zaachila Valley (Nierto-Samaniego *et al.*, 1995; Campos-Enríquez *et al.*, 2010).

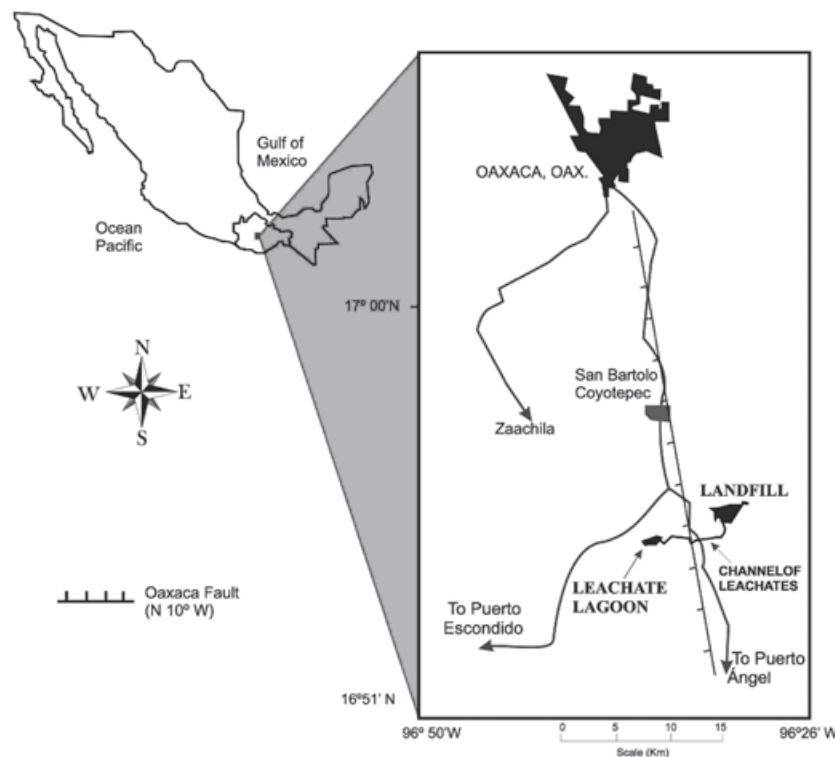


Figure 1. Location of Oaxaca City landfill and the leachate lagoon in the Oaxaca State, southern Mexico.

Seismic refraction survey

The seismic refraction survey at the leachate lagoon was designed to study the contrast between the unsaturated zone and the rockbed. Six seismic refraction lines with lengths of 108 m were obtained at several places around the site (Figure 2). A geophone spacing of 6 m and a hammer of 6 kg was used as the seismic source. Data was collected using a 24-channel seismograph (McSeis 170 OYO) and were interpreted using Geogiga software (2009).

Electromagnetic survey

Electromagnetic profiling along three 500 m long profiles with stations every 5 m were obtained using the Geonics EM34 conductivity meter operating at frequencies of 400, 1,600 and 6,400 Hz with a coil separation of 40, 20 and 10 m respectively. Further explanation of the theory used in EM34 can be reviewed in McNeill (1980). For each coil separation the data were acquired with the coils oriented both horizontally and vertically in relation to the surface. The data interpretation was

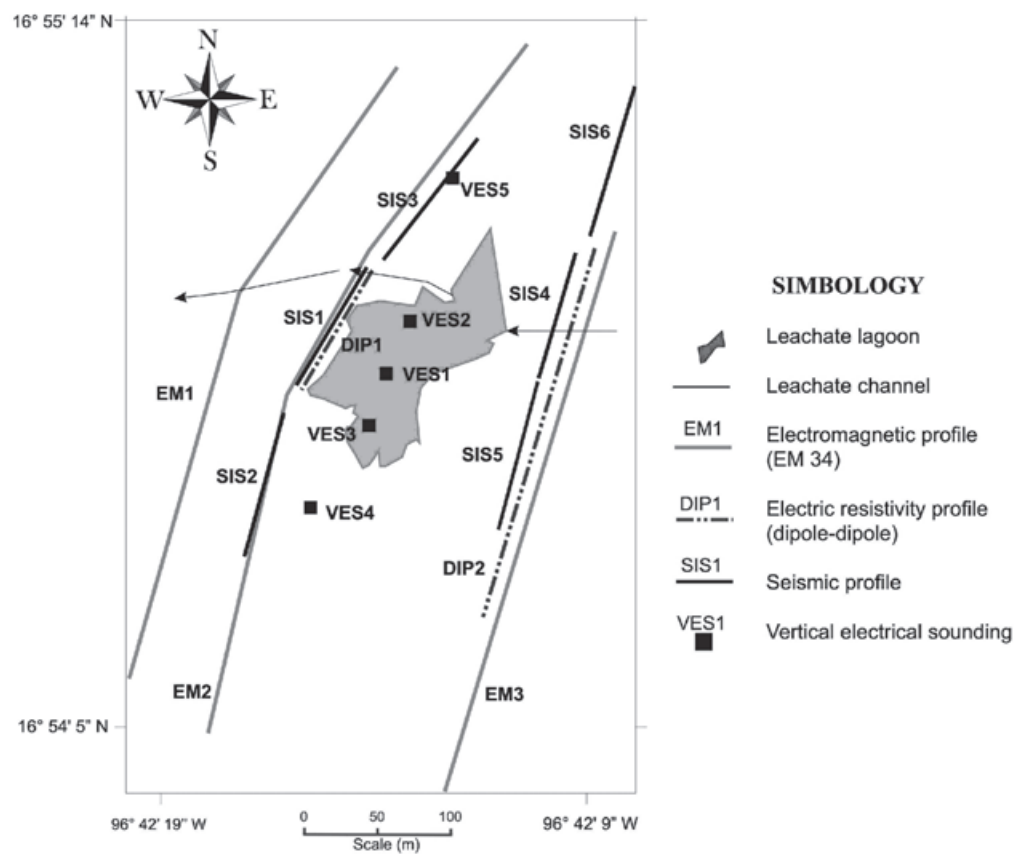


Figure 2. Location of seismic, electromagnetic, and dipole-dipole resistivity profiles, as well as of the vertical electrical soundings.

performed using the CICEM35 software developed at CICESE (Centro de Investigación Científica y de Educación Superior de Ensenada, Mexico), based in the modification of Gómez-Treviño's theory (1987) adapted by Pérez-Flores *et al.* (2001) for shallow EM.

D. C. Electric resistivity survey

a) Profiling

Two D.C. electric resistivity profiles using the dipole-dipole array were performed in the study area. DIP1 was conducted in the NW border of the

leachate lagoon with a 100 m length, 7 levels of investigation and an inter-electrode distance, a , of 2 m. DIP2 was located in the southwestern border with a 250 m length, an interelectrode distance of 5 m, and 7 levels of investigation. The data were interpreted using the CICES35 software from CICESE (Pérez-Flores *et al.*, 2001).

Misfit were 6.3 and 7.2% for DIP1 and DIP2 respectively. The 2D models were obtained in a single iteration under the approximation of low-resistivity contrast as explained in Pérez-Flores *et al.* (2001).

b) Sounding

In the dry season of 2008 (May) five vertical electrical soundings (VES) using the Schlumberger configuration were obtained in the study site (Figure 2). SEV1, SEV2 and SEV3 were made inside the lagoon, while SEV4 and SEV5 were located at the western and eastern borders respectively. A maximum current electrode spacing (AB/2) of 100 m was used for all the soundings. The processing and interpretation of the respective geoelectrical data was performed using the DCINV software (Pirttijärvi, 2005). During this survey particular attention was given to the electrode length since the soil texture did not allow the penetration of the electric current and it became necessary to use 60-cm long electrodes.

Hydrogeological control parameters

A piezometric map of the leachate lagoon was made by monitoring 8 wells drilled by the inhabitants as their source of potable water (Figure 3). Such monitoring wells were geo-referenced using an Astech ProMark2 GPS System and were also used to establish electric conductivity, total dissolved solids (TDS) and pH of water using a Hanna HI 98129 tester. The underground flow pattern was determined during the dry season

of 2007(November) and during the wet season (July, 2008). The hydraulic conductivity was established with two tests (D1 and D2) carried out in July of 2008 (Figure 3) using a variable charge infiltrometer. The dataset obtained was analyzed using the Darcy’s method (Sumner, 2000).

$$K_s = \frac{L}{t} \ln \frac{h_1 + L}{h_2 + L}$$

Where

h_1+L is the hydraulic head in the upper part of the infiltrometer.

h_2+L is the hydraulic head in the lower part of the infiltrometer.

Once the hydraulic conductivity was established, the transmissivity was estimated using stratum thicknesses obtained by means of the seismic study. Porosity was established through the Kozeny-Carman equation (Batu, 1998) modified for the conditions of the study area.

$$\frac{K}{0.4825} (1 - \eta)^2 = n^3$$

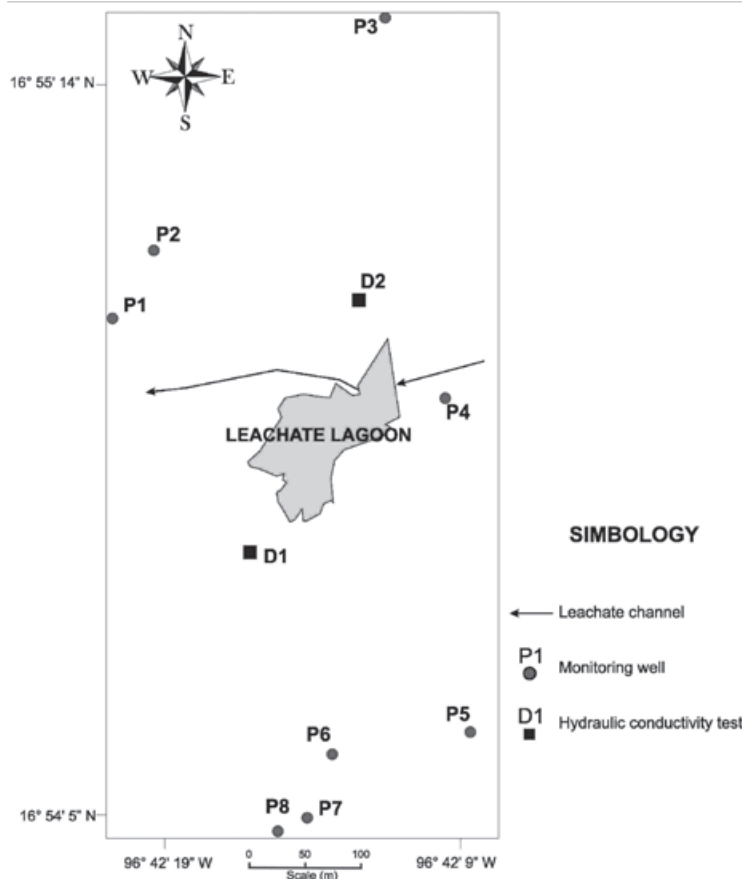


Figure 3. Localization of monitoring wells and sites of hydraulic testing.

Where

K is the hydraulic conductivity.
 n is the porosity.

Metal content and some chemical parameters (DOQ, carbonates, pH, electrical conductivity) were analyzed in samples of leachate and water from the closest well to the lagoon, P4 (Figure 3).

Results

Geophysical Surveys

a) Refraction seismic

Figure 4 shows the travel-time curves (hodochrones) corresponding to the SIS1 and SIS2 seismic profiles.

According to the seismic refraction data (Figure 5) to the west of the lagoon, along profiles SIS2, SIS1 and SIS3, there is a shallow layer with a velocity of 390 m/s associated to alluvium, overlying a shale bed with a velocity of 2,800 m/s. On the other side of the lagoon, along SIS5, SIS4 and SIS6 profiles (Figure 6), it was possible to delineate three layers. Below SIS5 and SIS6, the shallower bed presents a velocity of 390 m/s associated also to alluvium, while below SIS4 it presents a velocity of 280 m/s related to polluted alluvium close to the leachate lagoon. This first layer reaches its maximum depth of 7 m in SIS4 and SIS6. Along profiles SIS5 and SIS6, below the alluvium bed, there is a layer with a velocity of 1,300 m/s that has been interpreted as fractured shale. Contrastingly, in profile SIS6, the shale is not fractured and has a velocity of 2,800 m/s. Finally at the base of these three profiles a

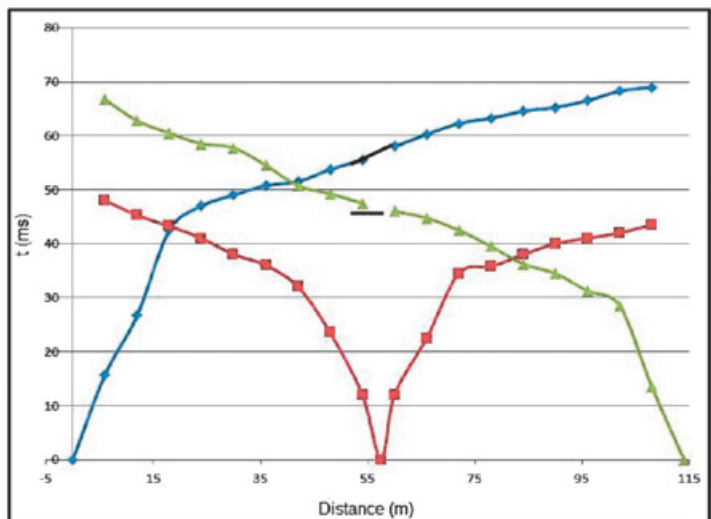
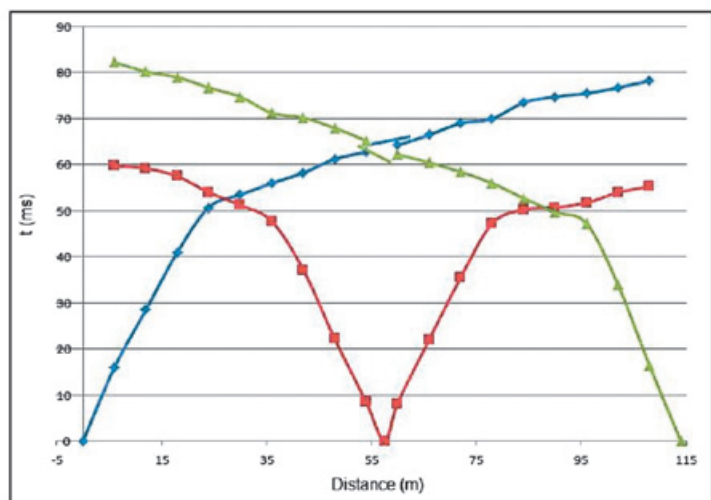


Figure 4. Dromochrones of seismic profiles obtained SIS2 and SIS1, leachate lagoon.

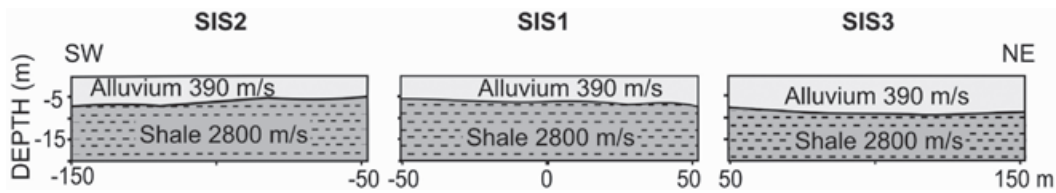


Figure 5. Seismic structure along the western border of the leachate lagoon.

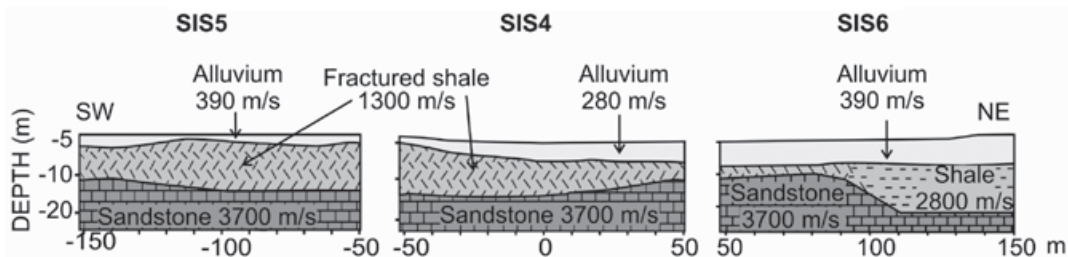


Figure 6. Dromocrones of the seismic profiles obtained in SiS2 and SiS1, of the leachate lagoon.

stratum with velocity of 3,700 m/s was mapped, which is been interpreted as the upper portion of an anticlinal structure of sandstone probably related to the Oaxaca Fault System.

b) Electromagnetics

Electromagnetic sections (Figure 7) indicate three resistivity domains. The shallowest one has a

resistivity ranging from 10 to 30 Ohm-m associated with alluvium and clay. The second domain is related to resistivities higher than 70 Ohm-m representing shale and fractured shale according to the seismic models (Figures 5 and 6). The last domain corresponds to a very conductive anomaly with values less than 10 Ohm-m associated with the leachate. In the EM1 profile, the conductive anomaly is seen at the surface from the positions

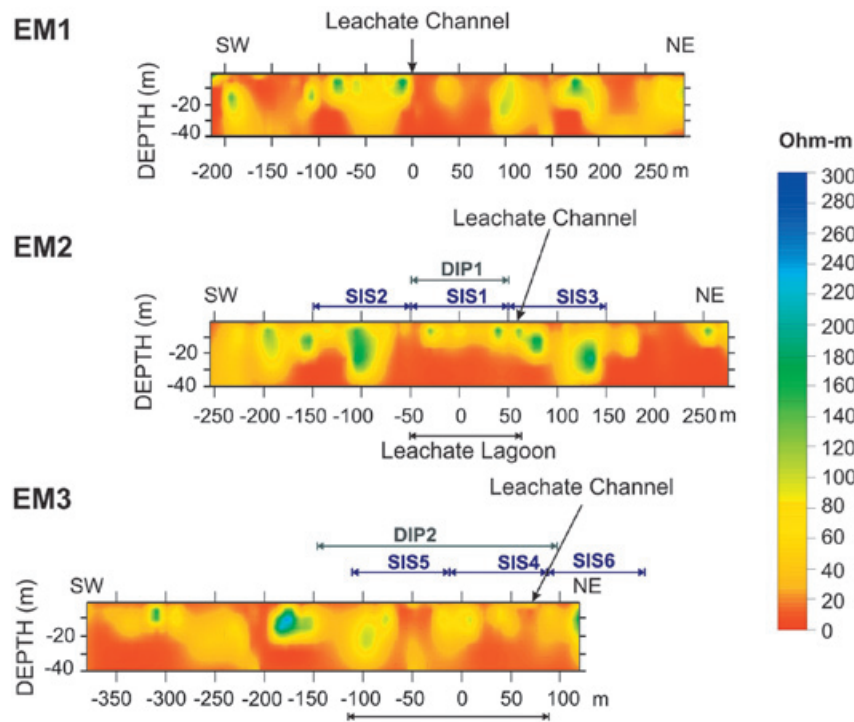


Figure 7. Electromagnetic models showing the correspondence with D.C resistivity and seismic profiles.

-200 to -100 m. Although the resistivity would suggest the presence of polluted soil, the true correspondence with the contaminants is found from 0 to 100 m due to the presence of the leachate channel. However, anomalies at depths of more than 20 m centred at positions -100, 0 and 150 m could suggest a toxic plume in the subsoil. The EM2 profile indicates the presence of a 2-D electric resistivity distribution mainly from -50 to 50 m coinciding with the lagoon. The DIP1 and SIS1 profiles also cover this area and indicate a conductive anomaly and a stratum of alluvium, respectively. Other important sections with low resistivity (less than 5 Ohm-m) are shown at positions -150 and 250 m, assumed as the signature of a contaminant plume percolating into the subsurface from the SW border of the lagoon and the area around the channel. From -100 to 100 m the EM3 model has a conductive anomaly (10 Ohm-m) associated with an area of leachate inundation during the rainy season, and the anomaly is represented in the DIP2 model (Figure 8). From -250 to -200 m, underlying a section with a resistivity higher than 100 Ohm-m, the model presents a value less than 5 Ohm-m interpreted as a leachate infiltration at a 30 m depth. According to the 2-D distribution of the EM models, changes going from the surface to the bottom of the sections, are interpreted as due to vertical fractures.

c) D.C. Electric resistivity

The dipolar profiles (Figure 8) DIP1 located at the western limit of the lagoon corresponds to the SIS1 seismic profile and to the central portion of the EM2 electromagnetic profile (Figure 7). DIP1 is featured by low resistivity values between 5 to 30 Ohm-m coinciding to the very conductive area (<10 Ohm-m) related to the subsoil around the

leachate channel as depicted by the EM2 electro-magnetic image between positions -50 and 50 m. The opposite profile, DIP2, covers SIS4 and SIS5 profiles and the right side of the EM3 profile from -150 to 100. DIP2 shows a very conductive section with values less than 20 Ohm-m in correspondence to a zone of leachate inundation that can also be observed in the EM3 electromagnetic image between distances -100 and 50 m (Figure 7). In both DIP1 and DIP2 models resistive anomalies of 100 Ohm-m are associated with fractured shale.

Figure 9 shows, for comparison purposes, VES curves obtained from soundings inside the leachate lagoon and outside it respectively.

Hydrogeological control parameters

The SW-D1 test (Figure 3) gave a hydraulic conductivity (K) of 64 m/day. The corresponding transmissivity (T) has a value of 282m²/day and a porosity of 35%. At the NW-D2 test, the hydraulic conductivity (K) was of 157 m/day, a transmissivity (T) of 1,413m²/day, and a porosity of 39%. Figure 10 shows the preferential underground flow pattern in the wet (November/2007) and dry seasons (July, 2008) when there was a depression due to water extraction. Electric conductivity of water (Figure 11a) ranged from 543 to 752μS/cm, except in the P1 well, with an electric conductivity of 2,148μS/cm. We infer that this last value shows the effects influence of polluted plume at P3 and P4 wells. The water table is located in the shale layer; it decreased 3 m during the dry season (July/2008) with respect to the wet season. In contrast, the water table in the P1 well was constant in both seasons; this constancy together with the low transmissivity (282m²/day) of the zone favours the existence of the polluted plume. In addition,

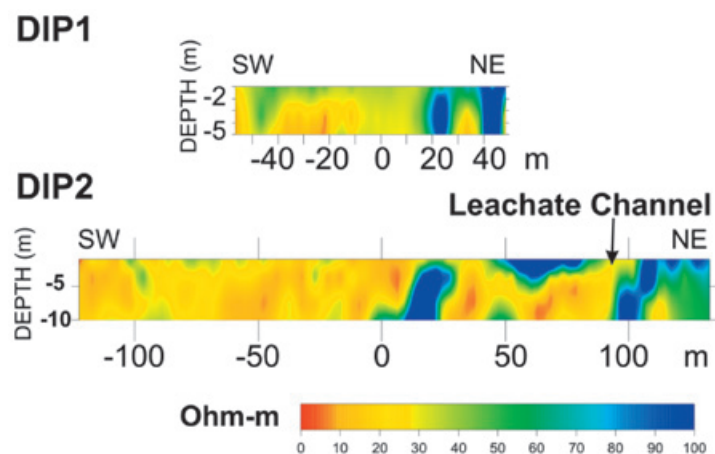


Figure 8. Geoelectric models using the dipole-dipole array.

the analysis of the water from P4 well indicates an important presence of chlorides (26.42 mg/l as Cl⁻) and nitrates (0.5 mg/L as N-NO₃). Figure 11b indicates the water pH in the study zone. The image shows that groundwater is almost neutral (7.12), but the monitoring of the wells close to the leachate lagoon shows that the water pH is slightly more basic (7.38). Physicochemical analysis of leachate sample indicated a pH of 8.4, which is related to an old fluid; the leachate COD (Chemical

Oxygen Demand) was established in 27,887.8 mg COD/l and its electric conductivity was 46,000µS/cm. Metal content in water, soil and leachates is summarized in Table 1. Here is observed that there are some elements in the leachate and soil that do not exist in water. Two explanations are possible. Either this circumstance indicates the infiltration to the rockbed through the fractures of the study area or the alluvium in the fractures allows the retention of some pollutants.

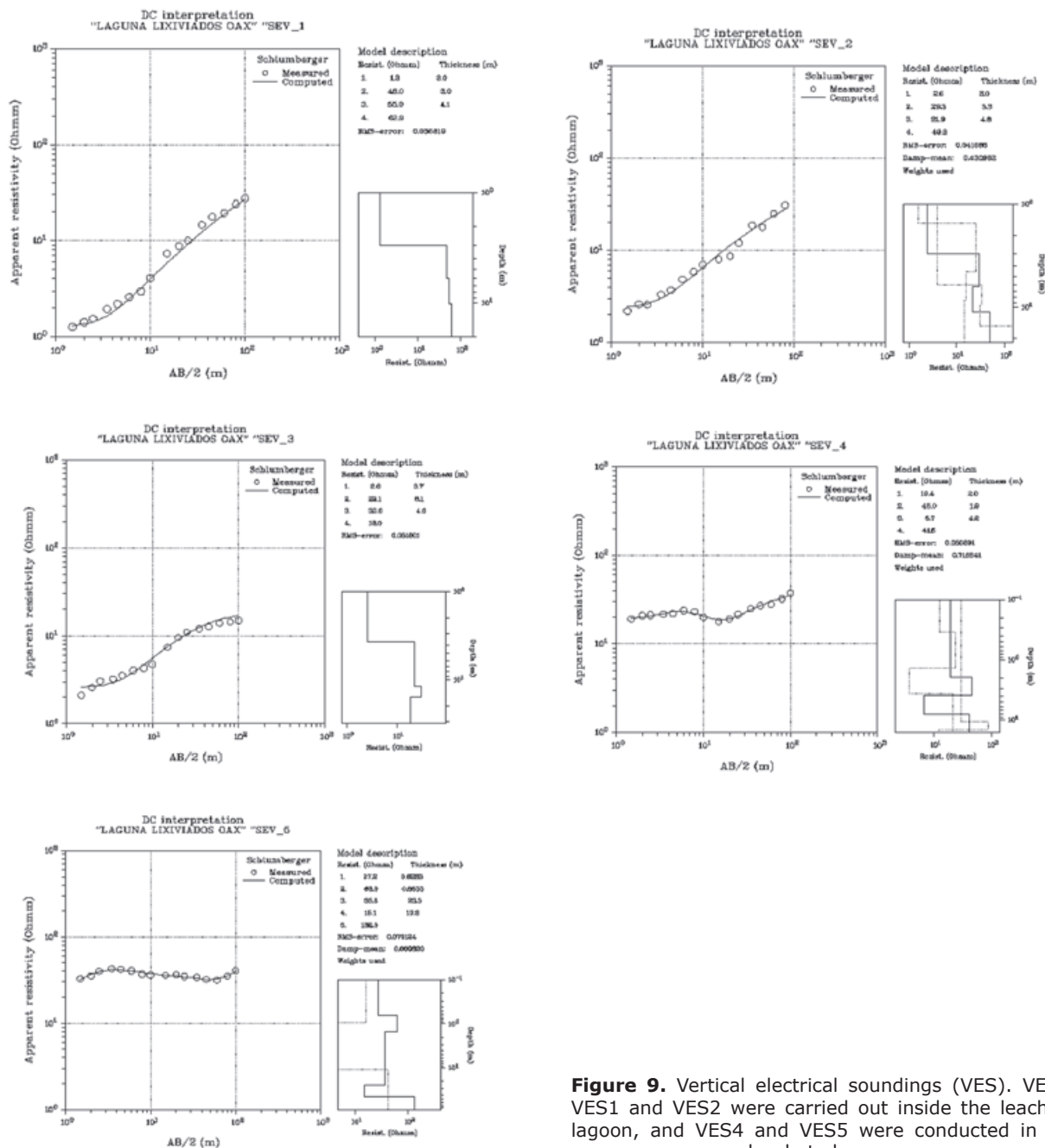


Figure 9. Vertical electrical soundings (VES). VES3, VES1 and VES2 were carried out inside the leachate lagoon, and VES4 and VES5 were conducted in the leachate lagoon.

Figure 10. Variation of underground water flow pattern. a) Wet season (November, 2007). b) Dry season (July, 2008).

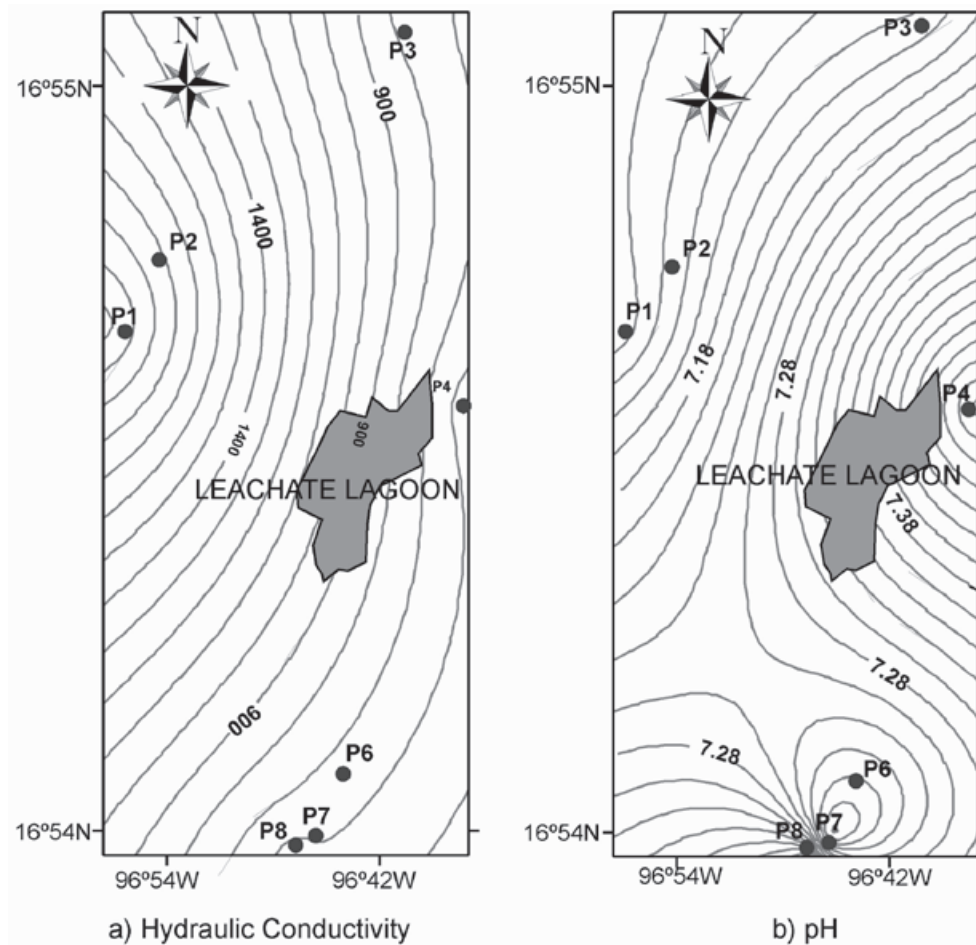
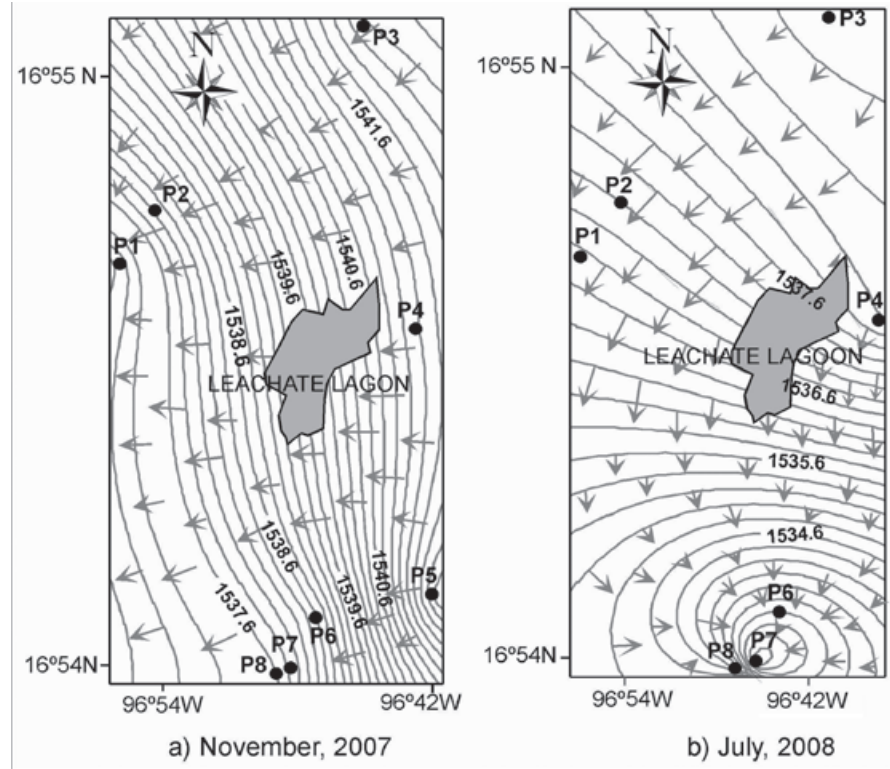


Figure 11. a) Map of hydraulic conductivity ($\mu\text{S}/\text{cm}$). b) pH of the water of the area of influence of the leachate lagoon.

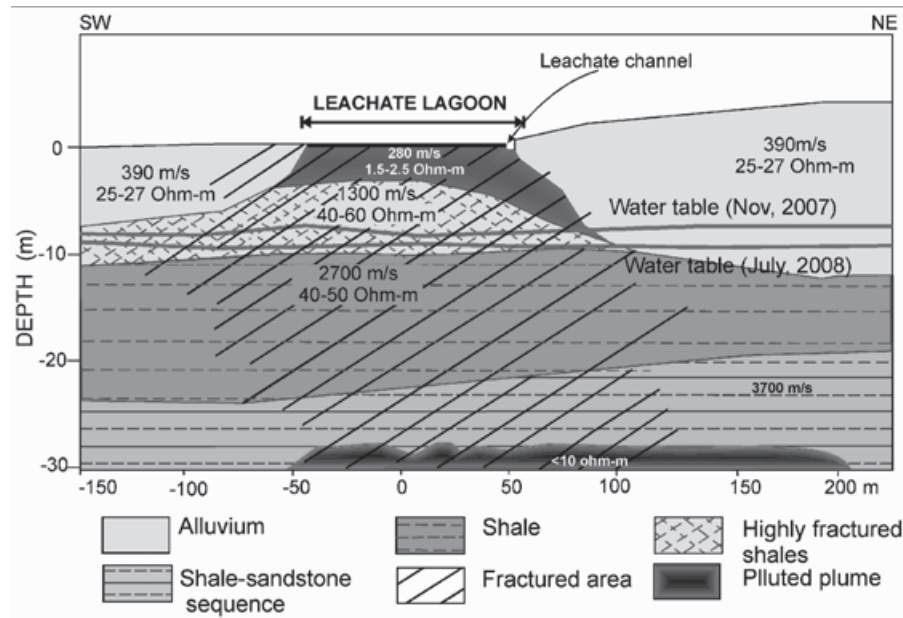


Figure 12. Hydrogeological model of leachate lagoon produced by Oaxaca City's landfill.

The hydrogeological model

The hydrogeological model of the leachate lagoon integrates the geophysical based information and the geohydrological control parameters (Figure 12). This model presents a very contaminated and conductive soil (1.5 to 2.5 Ohm-m) with a low velocity of 280 m/s immediately underlying the leachate lagoon and the leachate channel. This soil is associated to alluvium that is featured by resistivity values from 25 to 27 Ohm-m and a velocity of 390 m/s. The alluvium is relatively shallow with a maximum depth of 10 m at the NE border of the lagoon. The lower layer is highly fractured shale, probably related to the Oaxaca Fault, with a resistivity value of 40 to 60 Ohm-

m and a velocity of 1,300 m/s through which leachates could be infiltrating to the bedrock. In contrast, outcropping of shale presents the same resistivity range but a velocity of 2,700 m/s. Between alluvium and shale layers the water table fluctuates depending on the season (Figure 13). Small fractures could allow diffusion of pollutants in the aquifer but probably the characteristics of the soil have delayed them reaching the water (see Table 1). Finally the bedrock is represented by a shale-sandstone sequence with a velocity of 3,700 m/s. Here the polluted soil is related to a very conductive anomaly (<10 Ohm-m) at a depth of 30 m coinciding with the lagoon and leachate channel.

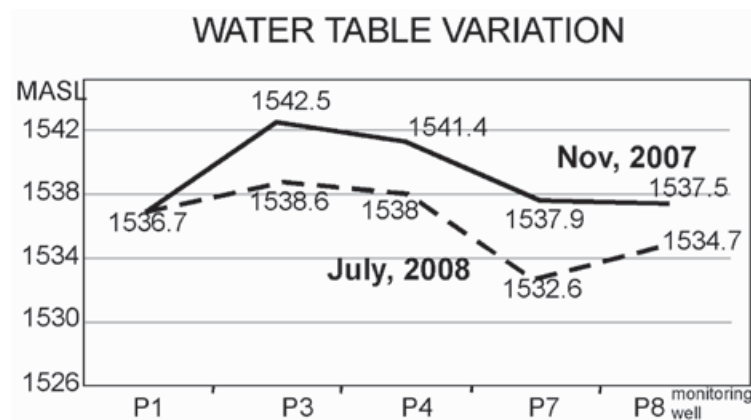


Figure 13. Water table variation in the study area.

Table 1. Chemical elements detected in samples of leachate, soil, and groundwater, for the period July, 2008, in parts per million (ppm).

METAL	SOIL	LEACHATE	WATER	METAL	SOIL	LEACHATE	WATER
Al	7.67	5	0	Fe	3.55	26	0
Sb	0	0.1	0	P	675	15	0
As	17	0	0	Mg	0.79	44.8	9.6
Ba	472	0.8	0.2	Mn	377	0	0
Ca	5.54	108	66	Mo	0	0.1	0
Co	17	0.1	0	Ni	26	0.3	0
Cu	60	0.3	0	Pb	0	0.2	0
Cr	66	1.4	0	K	2.32	1809.4	15.4
Sc	15	0.002	0	Na	1.07	1635	23
Sn	0	1.2	0.03	Zn	157	1	0.004
Sr	185	0.7	0.3	Ti	0.19	1.2	0

Conclusions

The geophysical information of the structure of the subsurface and geohydrological parameters allows more robust characterization of contaminated sites. This methodology is useful to establish a representative robust hydrogeological model of a study area and could be applied in detection and remediation of leachate contaminated sites. In the current case, the results indicate a very contaminated area underlying the lagoon and an important conductive area enclosed in the rock bed at a depth of 30 m. Both anomalies indicate leachates in the subsoil. Moreover a displacement of a polluted plume to the SW of the lagoon was detected. With respect to water quality, the results do not show the presence of toxic substances, although urbanization of the study site disturbs soil dynamics, and water extraction and house building are increasing the vulnerability of the Zaachila aquifer to the pollution.

Acknowledgments

This study was made with support of the projects SIP:20060280, and SIP:20070076 of CIIDIR-IPN.

References

- Asfahani J., 2007, Geoelectrical investigation for characterizing the hydrogeological conditions in semi-arid region in Khanasser valley, Syria. *J. of Arid Environments*, 68, 31–52.
- Atekwana B., Sauck W., Werkem D., 2000, Investigations of geoelectrical signatures at a hydrocarbon contaminated site. *Journal of Applied Geophysics*, 44, 167–180.

- Batu V., 1998, *Aquifer Hydraulics. A Comprehensive Guide to Hydrogeologic Data Analysis*. John Wiley and Sons, Inc. New York, NY. 752 pp.
- Bauer P., Supper R., Zimmermann S., Kinzelbach W., 2006, Geoelectrical imaging of groundwater salinization in the Okavango Delta, Botswana. *Journal of Applied Geophysics*, 60, 126–141.
- Belmonte-Jiménez S., Campos-Enríquez J., Alatorre-Zamora M., 2005, Vulnerability to contamination of the Zaachila aquifer, Oaxaca, México. *Geofísica Internacional*, 44, 283–300.
- Bengtsson L., Bendz D., Hogland W., Rosqvist H., Aksson M., 1994, Water balance for landfills of different age. *Journal of Hydrology* 158 pp. 203 – 217.
- Buselli G., Lu K., 2001, Groundwater contamination monitoring with multichannel electrical and electromagnetic methods. *Journal of Applied Geophysics*, 48, 11 – 23.
- Campos-Enríquez J.O., Belmonte-Jiménez S.I., Koppie J.D., Ortega-Guerrero F., Arzate J.A., Martínez -Silva J., Martínez-Serrano R.G., 2010, Gravity and magnetic survey of the Oaxaca city region: Cenozoic horst and graben structure superimposed on the Oaxaca-Juárez terrane boundary, southern Mexico, *Journal of South American Earth Sciences*, 29, 572–585.
- Chandra S., Anand Rao V., Singh V., 2004, A combined approach of Schlumberger and axial pole-dipole configurations for groundwater exploration in hard-rock areas. *Current Science*, 86, 1,437-1,442.

- CICEM35, Pérez-Flores M., Gómez-Treviño E., 2D Resistivity and EM Inversion. EM-34 2D inversion program. Internet free use: <http://arcada.cicese.mx/geofisica/dc2/index.html>
- CICRES35, Pérez-Flores M., Gómez-Treviño E., 2D Resistivity and EM Inversion. DC resistivity. 2D inversion program. Internet free use: <http://arcada.cicese.mx/geofisica/dc2/index.html>
- Corwin D., Lesch S., 2005a, Characterizing soil spatial variability with apparent soil electrical conductivity. Part I. Survey protocols. *Computers and Electronics in Agriculture*, 46, 103–133.
- Corwin D., Lesch S., 2005b, Characterizing soil spatial variability with apparent soil electrical conductivity. Part II. Case study. *Computers and Electronics in Agriculture*, 46, 135–152.
- De la Vega M., Osella A., Lascano E., 2003, Joint inversion of Wenner and dipole–dipole data to study a gasoline-contaminated soil. *Journal of Applied Geophysics*, 54, 97–109.
- Fatta D., Papadopoulos A., Loizidou M., 1999, A study on the landfill leachate and its impact on the groundwater quality of the greater area. *Environmental Geochemistry and Health*, 21, 2, 175–190.
- Feng S., Wang X., Wei G., Peng P., Yang Y., Cao Z., 2007, Leachates of municipal solid waste incineration bottom ash from Macao: Heavy metal concentrations and genotoxicity *Chemosphere* 67, 6, pp. 1133–1137 DOI:10.1016/j.chemosphere.2006.11.030.88
- Geogiga Software, 2009, Complete Package for Near Surface Geophysics. Geogiga Technology Corp. Canada.
- Gómez-Treviño E., 1987, Nonlinear integral equations for electromagnetic inverse problems. *Geophysics*, 52, 1, 297–1,302.
- Higuera-Díaz C., Carpenter P., Thompson M., 2007, Identification of buried sinkholes using refraction tomography at Ft. Campbell Army Airfield, Kentucky. *Environmental Geology*, 53, 805–812, DOI 10.1007/s00254-007-0693-y.
- Inman D., Freeland R., Ammons J., Yoder R., 2002, Soil Investigations using Electromagnetic Induction and ground-penetrating radar in southwest Tennessee. *Soil Science Society of America Journal*, 66, 206–211.
- Kumar D., Alappat B., 2005, Evaluating leachate contamination potential of landfill sites using leachate pollution index. *Clean Technologies and Environmental Policy*, 7, 90–197.
- McNeill J.D., 1980, Electromagnetic terrain conductivity measurement at low induction numbers. Geonics Limited, 15 p.
- Nieto-Samaniego A., Alaniz-Álvarez S., Ortega-Gutiérrez F., 1995, Estructura interna de la falla de Oaxaca (México) e influencia de las anisotropías litológicas durante su actividad cenozoica. *Revista Mexicana de Ciencias Geológicas*, 7, 1, 1–8.
- Nobes D., 1996, Troubled Waters: Environmental Applications of Electrical and Electromagnetic Methods. *Surveys in Geophysics*, 17, 393–454.
- Owen R., Gwavava O., Gwaze P., 2005, Multi-electrode resistivity survey for groundwater exploration in the Harare greenstone belt, Zimbabwe. *Hydrogeology Journal*, 14, 244–252.
- Pérez-Flores M.A., Méndez-Delgado S., Gómez-Treviño E., 2001, Imaging low-frequency and DC electromagnetic fields using a simple linear approximation. *Geophysics*, 66, 1, 067–1,081.
- Pirttijärvi M., 2005, DCINV 1-D Interpretation of electrical (DC) soundings ver 1.4 Finlandia.
- Porsania J., Filho W., Elisa V., Shimelesa F., Dou-radob J., Mourab H., 2004, The use of GPR and VES in delineating a contamination plume in a landfill site: a case study in SE Brazil. *Journal of Applied Geophysics*, 55, 199–209.
- Rogenhagen J., Jokat W., Hinz K., Kristoffersen Y., 2004, Improved seismic stratigraphy of the Mesozoic Weddell Sea. *Marine Geophysical Researches*, 25, 265–282 DOI 10.1007/s11001-005-1335-Y.
- Rosqvist H., Dahlin T., Fourie A., Röhrs L., Bengtson A., Larsson M., 2003, Mapping of leachate plumes at two landfills sites in South Africa using geoelectrical imaging techniques. Proceedings of 9th. International Waste Management and Landfill Symposium.
- Sundararajan N., Srinivas Y., Narasimha Chary M., Nandakumar G., Hanmantha C., 2004, Delineation of structures favorable to groundwater occurrence employing seismic refraction method: A case study from Tiruvuru, Krishna district, Andhra Pradesh A. The Proceedings of the Indian Academy of Sciences: Earth and Planetary Sciences, 113, 3, 259 267.
- Sumner M., 2000, Handbook of Soil Science CRC Press., USA, 2148 p.

- Telford W., Geldart L., Sheriff R., 1990, *Applied Geophysics*. Cambridge University Press, USA, 796 pp.
- Valenta J., Dohnal J., 2007, 3D seismic travel time surveying a comparison of the time-term method and tomography (an example from an archaeological site) *Journal of Applied Geophysics*, 63, 46–58.
- Williams C., Agassi M., Letey J., Farmer W., Nelson S., Ben-Hur M., 2000, Facilitated Transport of Napropamide by Dissolved Organic Matter Through Soil Columns. *Soil Science Society of America Journal*, 64, 590-594.
- Yan Z., Clayton R., Saleeby J., 2005, Seismic evidence for step faults cutting highly attenuated continental basement in the central Transverse ranges, California. *Geophysical Journal International*, 160, 651-666, DOI:10.1111/j.1365-246X.2005.02506.x.
- Yoon G., Park J., 2001, Sensitivity of leachate and fine contents on electrical resistivity variations of sandy soils. *Journal of Hazardous Materials*, B84, 147–161.

Looking for active faults at east Qattara depression, northwestern desert, Egypt

Taha Rabeh*

Received: April 01, 2011; accepted: February 07, 2012; published on line: September 28, 2012

Resumen

Los datos del campo potencial son considerados el principal factor que sustenta los procesos de exploración geofísica, utilizados para detectar y evaluar las estructuras del subsuelo. En este caso se realizó en el campo una recopilación detallada de datos magnéticos en el área escogida anteriormente para la investigación sísmica. El objetivo principal de este estudio, es detectar las estructuras más profundas del subsuelo y investigar las posibles relaciones de estas estructuras con la actividad sísmica.

El mapa de RTP aeromagnéticos fue usado para detectar la extensión regional de las estructuras de interpretación a partir del trabajo de prospección magnética. Las interpretaciones fueron realizadas en mapas RTP del terreno y aeromagnéticos utilizando, técnica de filtrado, separaciones del mínimos cuadrados, análisis de tendencias tectónicas, análisis espectral, el método de Werner, y Euler y dos técnicas de dimensiones. Los resultados muestran que las principales tendencias tectónicas dominantes son N35° - 45°W, N45°- 65° E, E -W y las tendencias de Aqaba.

Por otra parte WQ85 dos líneas sísmicas-31B y 127 fueron interpretados y la localización de estas líneas son coincidentes con el mapa tectónico deducido. Los resultados muestran que existe una gran coincidencia entre la ubicación de las fallas deducidas de los datos geomagnéticos y sísmicos. Los resultados obtenidos indican una buena relación con los datos de pozos.

Además, estas estructuras están relacionadas con las actividades del terremoto registrado por el National Egyptian Seismological Network (ENSN). La correlación permite deducir que la zona de estudio es más estable que otras áreas adyacentes en el norte de Egipto, cerca del mar Mediterráneo y el río Nilo Delta.

Palabras clave: prospección magnética, líneas sísmicas, estructuras del subsuelo.

Abstract

Potential field methods are considered the cheapest tools in geophysical exploration to detect and characterize subsurface structures. Here we present a detailed land magnetic survey in an East Qattara Depression that was subjected before to a reflection seismic investigation. The main target of this study is infer the deeper subsurface structures and to investigate possible relations of these structures with earthquake activity.

The reduced to north Pole (RTP) aeromagnetic map was used for detecting the regional extension of the interpreted structures on the land magnetic survey. The interpretations were performed on the RTP land and aeromagnetic maps using filtering techniques, least squares separations, tectonic trend analysis, spectral analysis, Werner and Euler deconvolutions, and 2.5-D modelling techniques. The results indicate that the main dominant tectonic trends are N35°- 45°W, N45°-65°E, E-W and Aqaba trends.

Moreover two seismic lines WQ85-31B and 127 were interpreted and compared with the deduced tectonic map. The results show that there is a great correlation between the location of the faults deduced from both the magnetic and seismic data. The results agree with the well logging data.

Furthermore these structures correlated with the recorded earthquake activity by the National Egyptian Seismological Network (ENSN). This correlation implies that the studied area is more stable than other adjacent areas in the northern parts of Egypt close to the Mediterranean Sea and the Nile Delta River.

Key words: magnetic survey, seismic lines, subsurface structures.

T. Rabeh*
National Research Institute of Astronomy
and Geophysics Helwan
Cairo, Egypt and IDL, Lisbon, Portugal
*Corresponding author: taharabeh@yahoo.com

Introduction

The study area lies between 29° 50' and 30° 25' of Latitude N and 28° 15' and 28° 50' of Longitude E, at the eastern part of Qattara Depression of the North Western Desert (Figure 1), covering an area of about 1,000 km². Seismic reflection studies have been done in this area by many petroleum companies including Khalda Petroleum Co. (2000), and Badr El Din Petroleum Co. (2004) which are considered the largest oil companies with concessions in the study area.

An comprehensive land magnetic survey in a mesh like form was conducted also. The distances between the stations range between 200 to 500 m depending on the topography obstacles and rate of the magnetic field variations. The magnetic data were corrected by diurnal and latitude variations and finally reduced to the north magnetic Pole. The RTP magnetic maps were subjected to qualitative analysis using trend analysis, and two dimensional wavelength filtering techniques (Zurflueh, 1967).

Also, quantitative interpretation was performed along profiles crossing the studied area from east to west and from north to south, using spectral analysis and 2.5 - D magnetic modelling techniques using commercial software (GM-SYS, 1995).

2.5-D magnetic profiles were selected along two seismic lines (line WQ85-51B and line 127). A good correlation is observed between the features of the seismic lines and the features on the structural maps obtained from the magnetic data, and the 2.5-D magnetic modelled profiles.

Geology and tectonic setting of the area

The study area, as part of North Western Desert region, its geology bears the common following regional features. The stratigraphic sequence overlying the basement complex in the North Western Desert generally comprises three major lithological divisions as proposed by Said (1990), Barakat (1982) and Abdel Hady *et al.* (1988). From base to top we have (i) Lower Clastic Division of Pre-Cenomanian age, (ii)

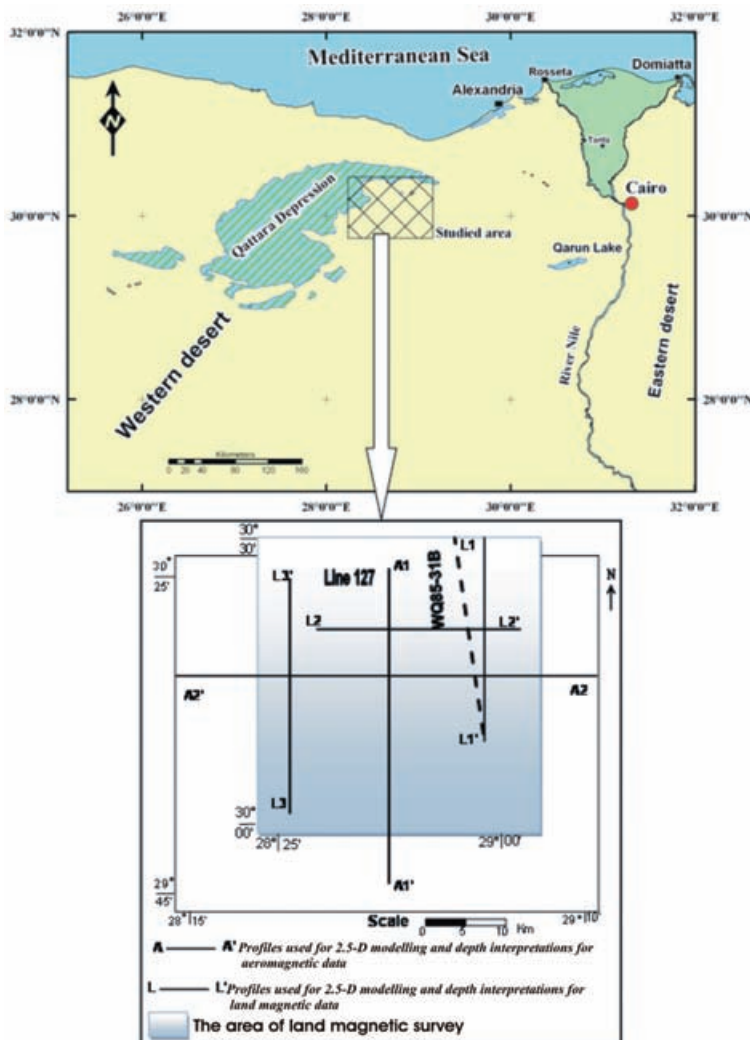


Figure 1. Location map of the study area showing the profiles used for seismic and magnetic interpretations.

Middle Calcareous Division of Cenomanian to late Eocene age (iii), and the Upper Clastic Division of Oligocene to recent age.

The surface geology (Figure 2) of the studied area shows that more than 80% of the zones covered by limestones of Miocene age is constituted by Sabkhas (evaporite-carbonate) deposits in the middle part. Sandstones and other Quaternary deposits with some minor Oligocene rocks are occupying the north-eastern part of the study area.

Recent seismicity mapped by Egyptian National Seismological Network (1997-2003) (Figure 3) indicates that the study area is featured a very low seismic activity, and earthquake activity is almost missing. This explains in part why surface faults (Figure 3) are absent or rare. This indicates also that the recent tectonics of the study area are more stable than others adjacent areas close to the Mediterranean sea or Nile-Delta.

Data acquisition and interpretation

A detailed land magnetic survey was made in the study area using two Proton magnetometers. One of them was fixed at the selected base

station, while the other was used to measure the total intensity along the stations that cover the study area in a mesh like form. The measured data were corrected for diurnal variations and for latitudes towards the north.

These data were digitized by computer digitizing programs and the total magnetic anomaly map was obtained. This map was reduced to the North Magnetic Pole using suitable FORTRAN program after Baranov (1975) (Figure 4). The RTP map illustrates the exact positions of the magnetic anomalies distributed all over the studied area. Furthermore, a RTP aeromagnetic anomaly map (Figure 5), was also used in the interpretation to illustrate the regional extensions of the subsurface structures.

The RTP magnetic maps indicate that most of these anomalies are aligned in NW-SE, NE-SW, and E-W directions. The deepest anomalies sources in the NE and SW portions as indicated by the presence of negative anomalies that imply thick sedimentary sequences, and from correlated drilled wells in these parts. The shallowest parts extend from NW to SE direction as indicated by the presence of positive anomalies and data from the drilled wells.

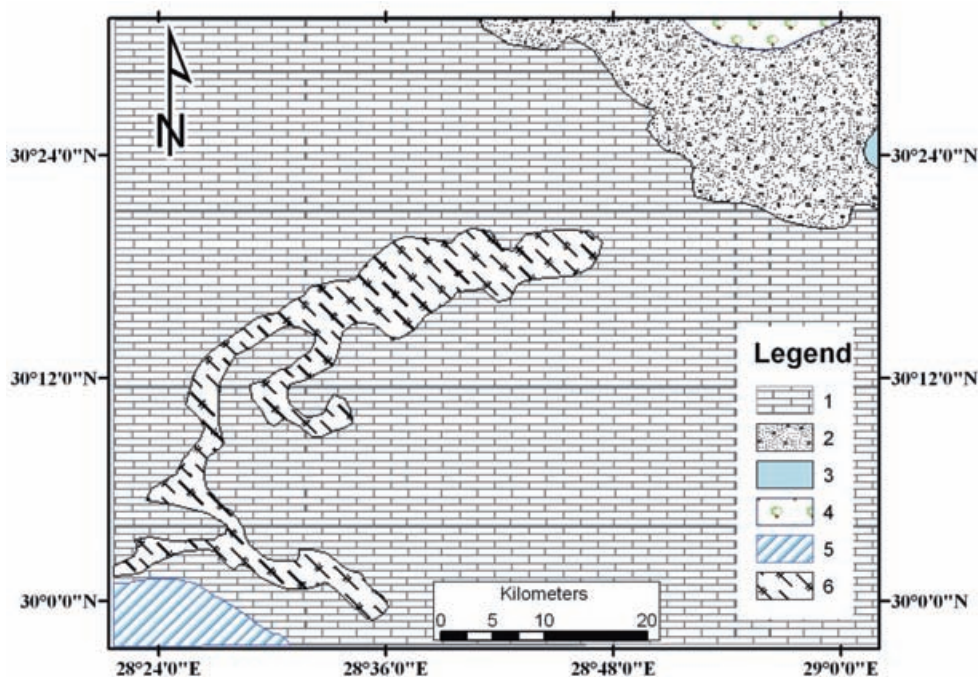


Figure 2. Surface geologic map of the study area after CONOCO (1987). 1- Miocene limestone, 2- Quaternary deposits, 3- Oligocene rocks, 4- Sand dunes, 5- Eocene limestone, 6- Sabkhas deposits.

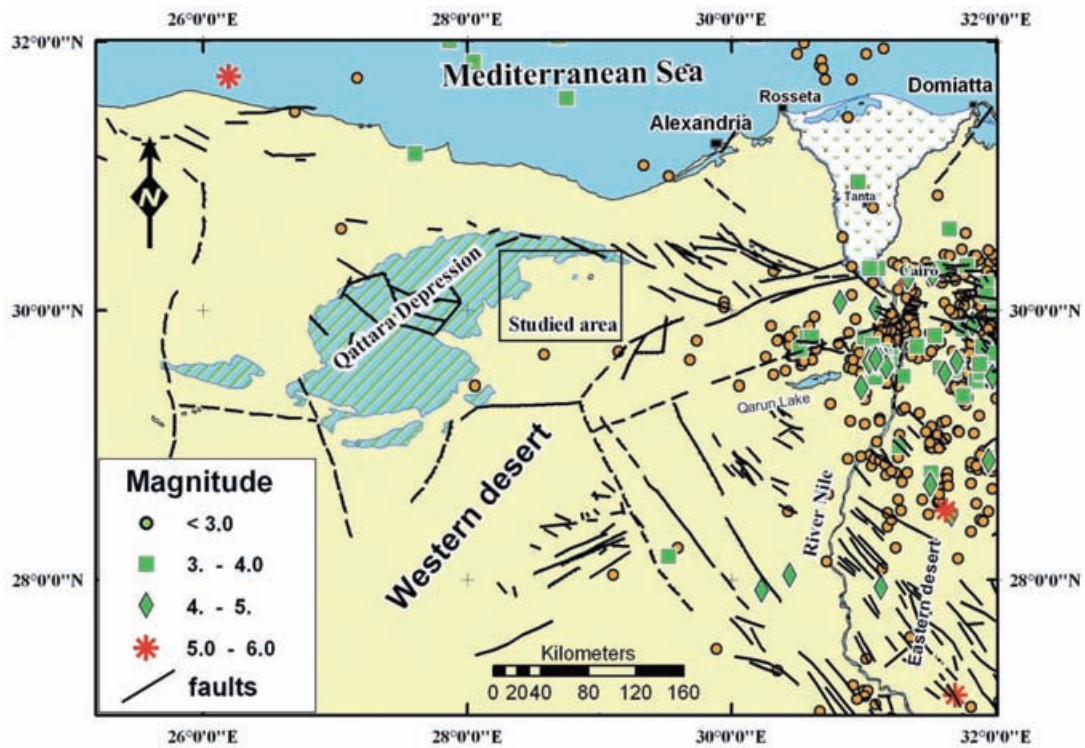


Figure 3. Recent earthquakes activity (1997- 2003) in the north western part of Egypt. Earthquake data were recorded by Egyptian National Seismological Network (ENSN).

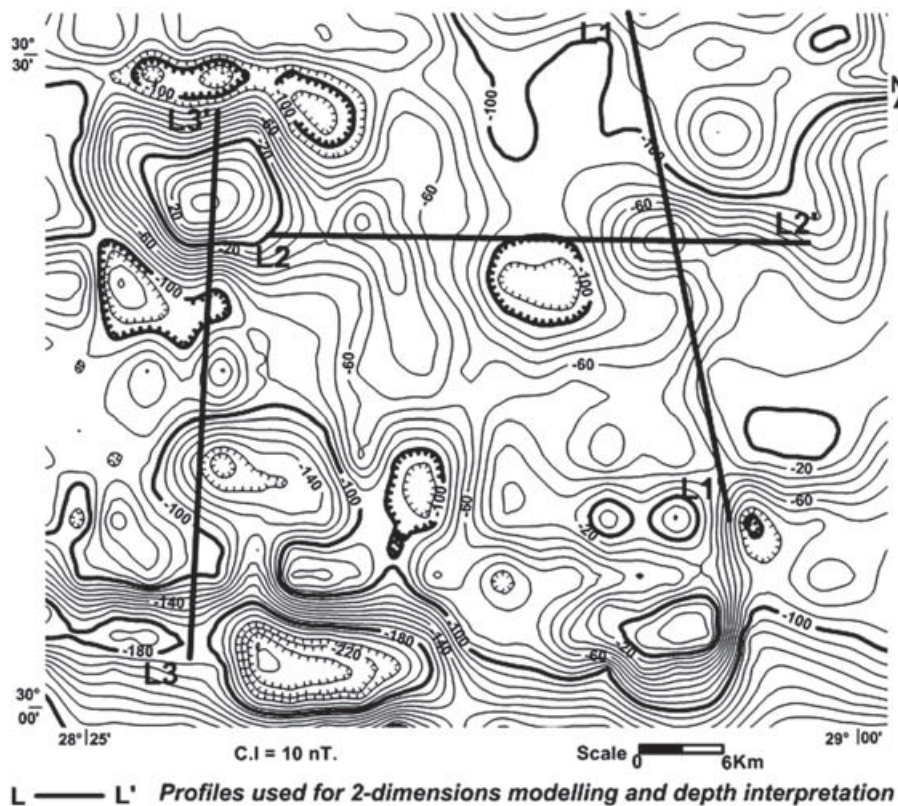
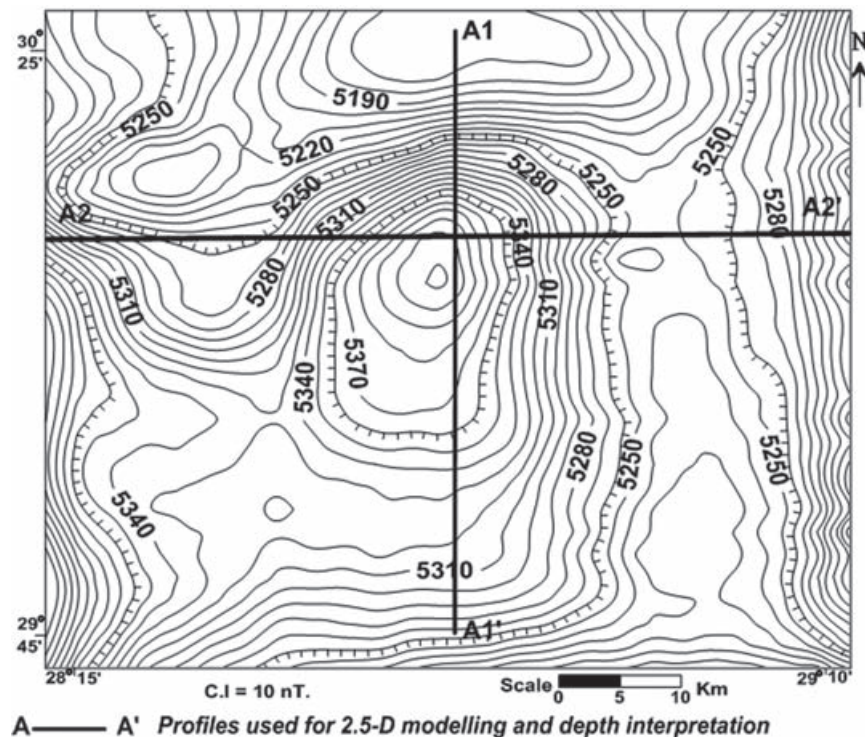


Figure 4. RTP land magnetic map of study area.

Figure 5. RTP aero-magnetic anomaly map of the study area after Egyptian General Petroleum Cooperation (1979).



Filtering technique

Wavelength linear filtering was applied to the RTP magnetic anomaly map. Fourier transform (Hildenbrand, 1983) processing was performed using three types of filters: (1) Low-cut of the residual anomalies with short wavelengths, high frequencies and shallow depths, (2) High-cut of the regional anomalies with long wavelengths, low frequencies and deep depths and (3) Band-pass of the transitional anomalies with intermediate wavelengths, frequencies and depth ranges.

The obtained maps show that most of the anomalies trend in the NW-SE, NE-SW and NNE-SSW directions. Figures 6 and 7 show regional of the landmagnetic map, and the residual corresponding to the aeromagnetic map.

respectively. It is clear that the negative anomalies at the northeastern and southwestern parts of the studied area are present at different levels. This could be originated from the presence associated to a thick sedimentary sequence. Meanwhile the positive anomalies extend from the northwest to southeast and could be due to the presence of a thin sedimentary sequence and/or intrusion.

Least squares method

The least square method of Henderson (1960), was applied using Surfer software to the RTP land magnetic and to the RTP aeromagnetic anomaly

maps to the area. First, second, and third order surfaces were fitted to the input magnetic and gravity data. This method consists of fitting a mathematical surface that approximates the regional component of the potential data. In all cases the condition of the least squares solution is $\sum R^2 = \text{minimum}$, where R denotes the residuals (Nettleton, 1976). The residual anomaly is given as:

$$RA = \Delta g - Z \quad (1)$$

where Δg is the observed potential data and Z is the regional surface.

The correlation coefficients between successive residual maps were computed in order to determine the optimum order of the regional surface to be used. Results were $r_{21} = 0.854$, $r_{21} = 0.965$, and $r_{34} = 0.546$.

The results indicate that the residual magnetic anomaly maps (Figures 8 and 9) of the second order represent the best fitted maps. Also these fitted maps are more or less analogous to the residual map resulted from the filtered technique.

Trend analysis technique

The RTP maps, together with the filtered maps (residual, band-pass and regional filtered maps) were used to delineate the common structural trends in the studied area. The lengths and trends for each detected lineament on the different maps were measured clockwise from the north.

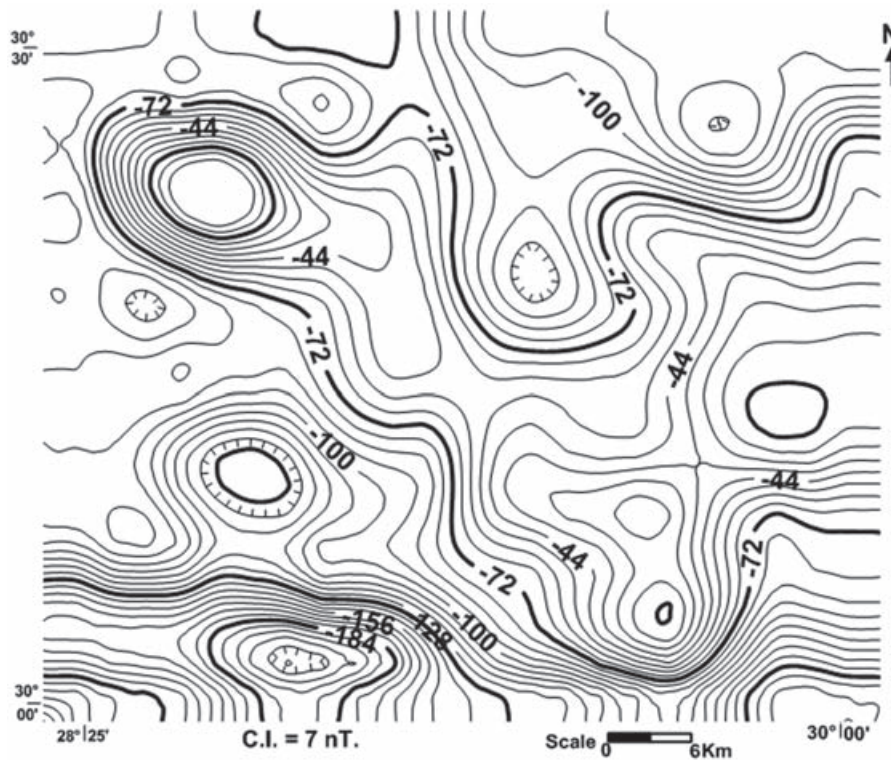


Figure 6. Low-pass regional filtered land magnetic anomaly map.

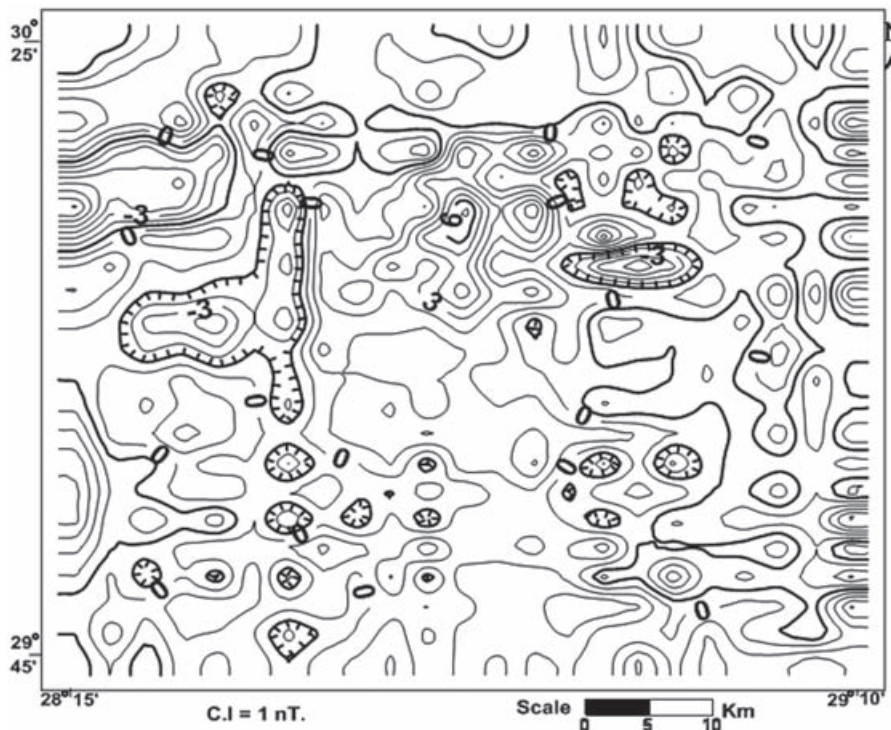


Figure 7. High-pass residual filtered aeromagnetic anomaly map.

Lengths were taken partially in consideration when calculating the statics. The deduced structures map from the land RTP magnetic anomaly map is assumed to represent the fault system affecting the area. On the other hand, the structure maps deduced from the filtered maps

represent faults taking place at different levels (shallow structures deduced from the residual map, intermediate structures deduced from the band-pass filtered map, and deep structures deduced from the regional anomaly map).

Depth estimation methods were applied to the filtered land magnetic maps to determine the mean depth of these structures. In case of Werner deconvolution method the mean values along the basement interface were calculated. Table 1 summarizes the results of Werner deconvolution and spectral analysis methods that would be explained later.

These results confirm that the filtered land magnetic maps represent the distribution of the magnetic anomaly at shallow (mean depth 1 km), intermediate (mean depth 2.3 km) and deep (mean depth 3.6 km) levels respectively.

The deduced fault planes of different directions are grouped every 10° around the north for their length percentage (L %). Statistical procedures have been used to illustrate the predominant

fault trends affecting the studied area. The results of azimuth distribution of both surface and subsurface elements are presented in the form of rose diagrams (Figures 10, 11 and 12).

The results show that the most predominant directions are N35° - 45° W, N45° - 65°E, E - W and Aqaba trends (Figure 11). These trends prevail at the shallow and deep depths lineaments.

Spectral analyses technique

The spectral analysis technique is used for determination of the depth to the basement under the sedimentary cover. This technique depends on the transformation of the space domain into frequency domain by using the Fourier transform.

Table 1. Depth estimation along profiles L1 and L2 of the filtered land magnetic maps.

Regional land magnetic map		Band-pass filtered		Residual land magnetic map		Method / map land magnetic map
Depth in Km		Depth in Km		Depth in Km		
L2	L1	L2	L1	L2	L1	Werner deconvolution method
3.7	3.5	2.25	2.1	1.2	1	
3.5	3.6	2.1	2.31	1.1	1.2	Spectral analysis method

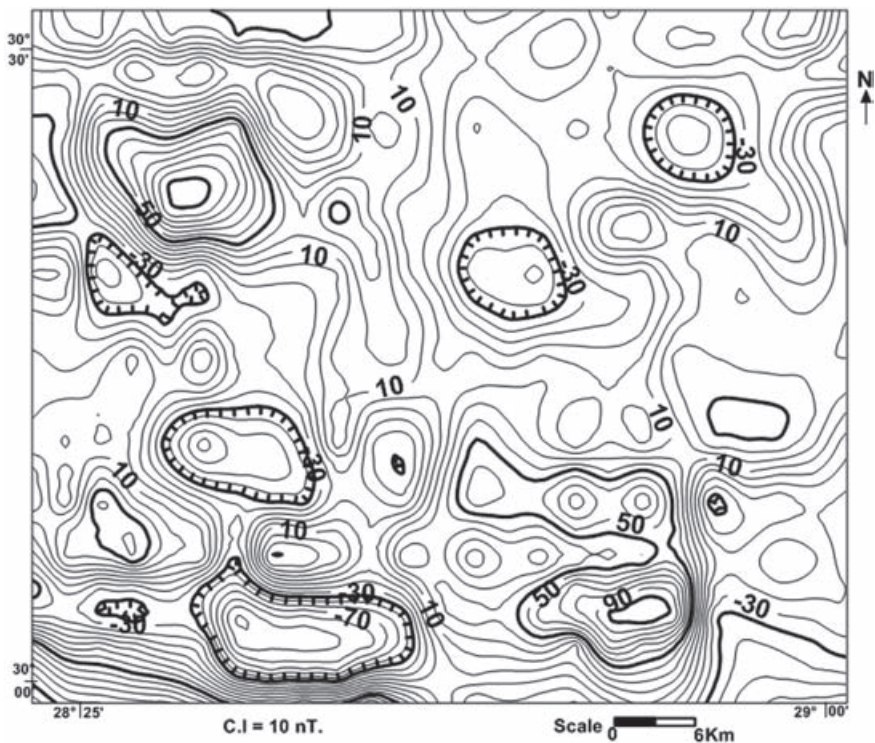


Figure 8. Least square land magnetic map (2nd order) of the study area.

Figure 11. Structure map as deduced from the RTP aeromagnetic map with location of interpreted seismic lines.

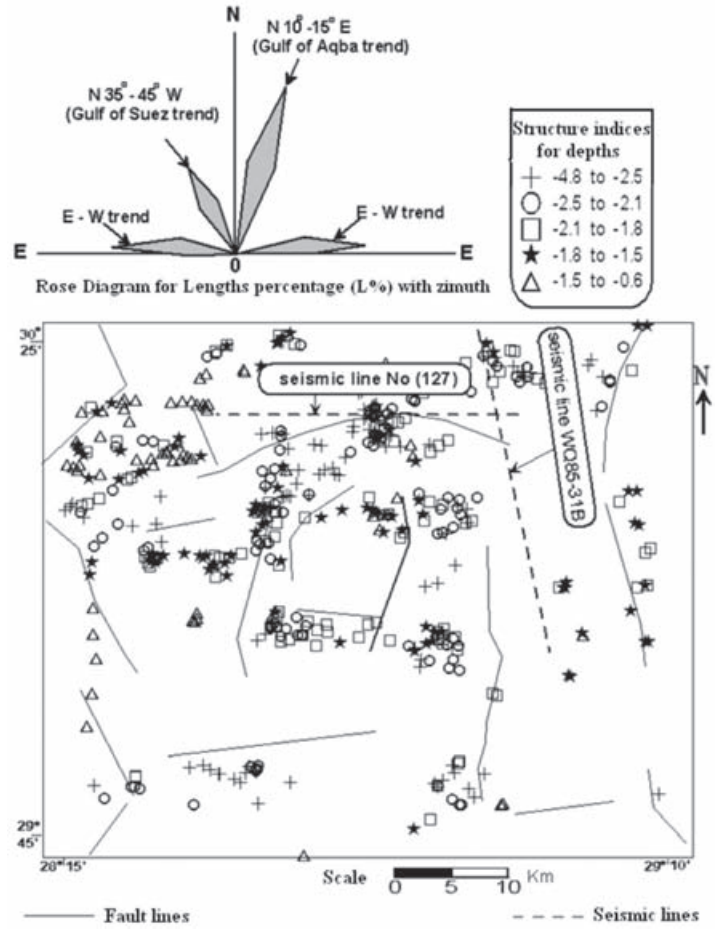
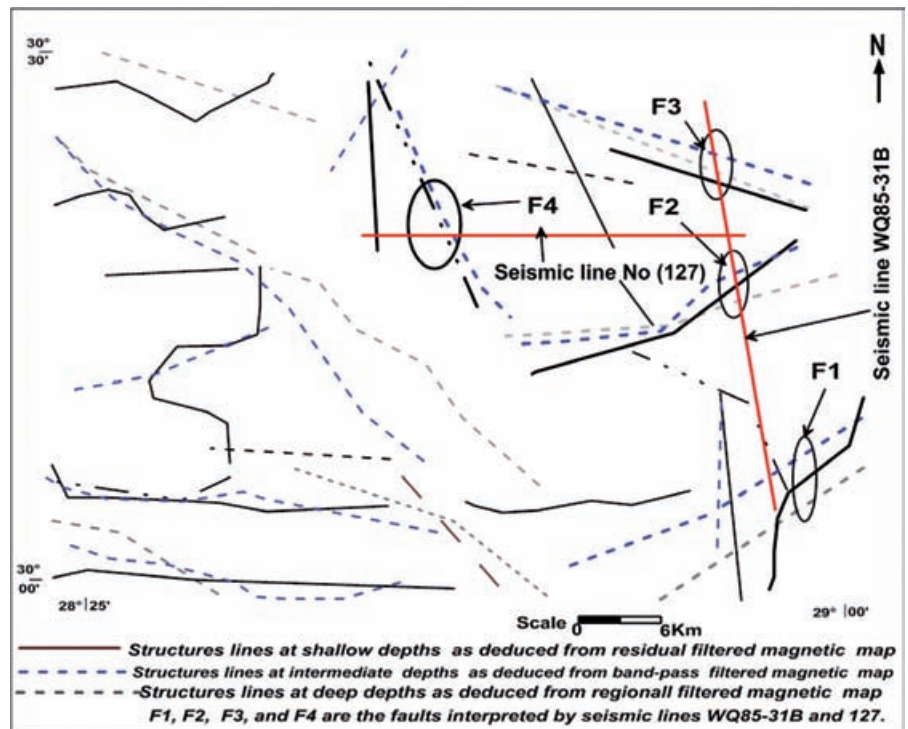


Figure 12. Fault structure lines as deduced from filtered magnetic anomaly maps.



It is expressed mathematically (Båth, 1974) as follows:

$$F(\omega) = \int_{-\infty}^{\infty} f(x)e^{i\omega x} dx \quad (2)$$

where: $F(\omega)$ is the Fourier transform of $f(x)$, $f(x)$ is the value of the function or anomalous potential data at a point x and, ω is the spatial frequency in cycle / unit distance in x . The depth z can be estimated from the graphical diagram of the \ln diagram of the long amplitude spectrum using the relation

$$-z = \tan(\Phi) \quad (3)$$

where: Φ is the dip angle of the straight line approximated in the diagram of the \ln -amplitude spectrum versus the spatial frequency.

The results (Figure 13) show that the main depth increases towards the north and western parts where they reaches volves of about 4.3 km or more and decrease towards the eastern and southern parts where they reaches volves of about 3.5 km. The depth to the intruded rocks ranges between 0.7 to 0.4 km.

Werner deconvolution method

The deconvolution technique (Werner,1953) is based on the selection of a group of four or more measurements in order to calculate the location of the magnetic body separately. When locations

are plotted in cross sections, the depth estimates tend to cluster around the true location of the causative body. Groups of consecutive points were treated as a "window" sliding along the profile.

The program applied to the RTP geomagnetic data is based on the method developed by Pasteka (2001) aimed to increase and confirm the resulting depths along the selected profiles for horizontal and vertical directions. The results confirm the tectonics deduced from the trend analysis of the RTP geomagnetic maps. Also it illustrates that the mean depth to the basement rocks is ranging between 3.9 and 4.1 km (Figure 14).

Euler deconvolution method

This method has a wide application to determine the subsurface positions (Reid *et al.*, 1990) and the depths to the geomagnetic inhomogeneities. (Thompson, 1982). It is applied to grided data. The method obtains the gradients, locate the square windows within the grids of gradient values and field, and obtain the structural data.

The method was applied to the RTP land magnetic and RTP aeromagnetic grided data using the 0.5 magnetic index, with a window size of 11 km, in order to obtain the depths to the basement rocks and their structures. The results were plotted in X and Y planes (Figures 10 and 11). These results indicate that the depth to the sources reaches about 4 km.

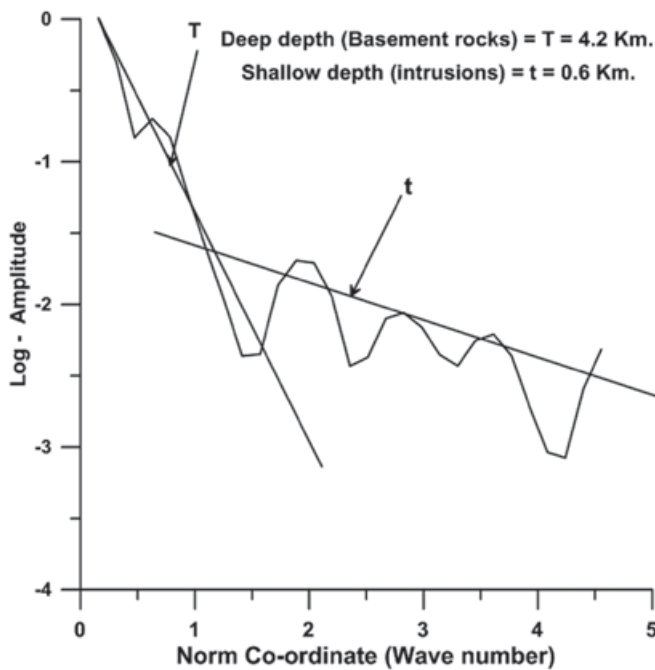


Figure 13. Spectral analysis from land magnetic map parallel to the location of seismic line (127).

The results deduced from the land magnetic data (Figure 10) are correlated with the results of the trend analysis technique due to the detailed survey contains more detailed information. Meanwhile the results of RTP aeromagnetic data (Figure 11) show less similarities with trend analysis owing to the regional survey may be poor in minor details.

Two and half dimensions model technique

The computation of the magnetic field due to 2.5-D model polygonal homogeneous magnetized bodies of arbitrary shape at a point (x, y, z) expressed by Ku (1977) is as Follows:

$$A_{DIP}(x,z) = \frac{2(J.R)}{R^2} \tag{5}$$

where: J is the magnetization vector, R is the radial vector between the point x, y, z and a point in the volume x', y', z' and equal to:

$$R = \sqrt{(x'-x)^2 + (y'-y)^2 + (z'-z)^2} \tag{6}$$

Computations of the magnetic effects for models with complex geometry have been carried out using GM-SYS computer program, by Northwest Geophysical Associates, Inc. (1995),

for an arbitrary two-dimensional polygon (c. e., Talwani, and Ewing).

The results show that the profile A1- A1' is affected by four faults from south to north (Figure 15). Whereas profile A2-A2' shows that it is affected by one fault F4 (Figure 16). In general the configuration of the basement surface obtained from 2.5-D modelling technique illustrates that the main depth of the area increases towards the north and west directions. The main depths to the basement surface range between 3.5 and 4.5 km.

Seismic lines interpretations

Two seismic lines WQ85-31B and 127 were prepared by Egyptian General Petroleum Cooperation (EGPC) trending N-S and E-W, respectively (Figures 17 and 18). They were correlated with the vertical velocity logs to locate the exact depths to the horizons (marker beds). These lines were interpreted to establish the shallower structures in the sedimentary rocks. These lines were correlated with the profiles interpreted from 2.5-D modeling technique.

This correlation reveals that the structures interpreted from these seismic lines correlate well with features deduced from the geomagnetic interpretations along the same profiles. This correlation also indicates that these structures are extending from the subsurface basement rocks upward to the sedimentary sequences.

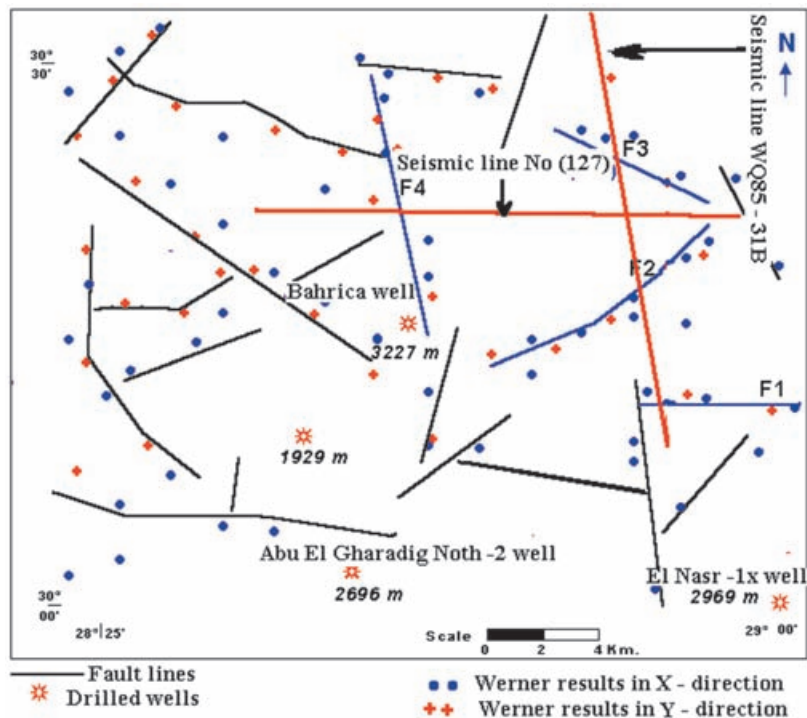


Figure 14. Result of application Werner and Euler deconvolution methods to RTP land magnetic map.

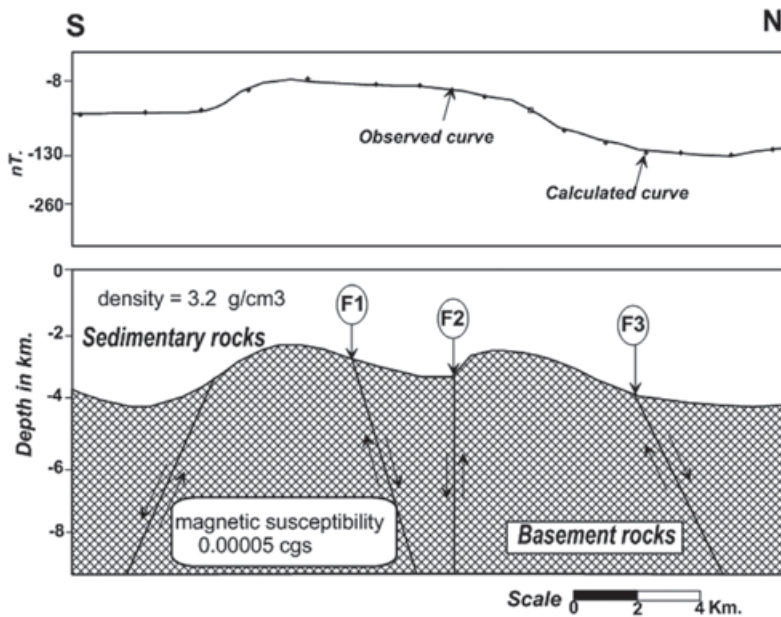


Figure 15. Two and half dimensions geomagnetic model along profile A1-A1' of the land magnetic map.

a- Interpretation along line WQ85-31B:

- The length of this line (Figure 17), is more than 18 km and covers from nearly the southern to the northern parts of the study area. The interpretation along this line indicates that there are three normal faults affecting the sedimentary section. These faults are affecting Bahariya, Abu Roash, Khoman, and Apollonia formations. The mean depth to the upper surface of these faults is about 600 meter. The deduced faults can be correlated approximately with the faults F1, F2 and F3 deduced from the interpretations of geomagnetic data.

b- Interpretation along line 127:

- This seismic line (Figure 18), extends in E-W direction and covers more than 24 km. This line is parallel to the profile L2 - L2' along the RTP land magnetic map. This line is affected by two faults. The first fault cuts Bahariya, Abu Roash, Khoman, and Apollonia formations and the other branch of this fault cuts only the Bahariya formation. The second fault passes Bahariya Fm and it is the oldest. Also, we note that the first fault correlated with the F4 deduced by geomagnetic interpretations. The depth to the upper surface of this fault reaches about 600 m.

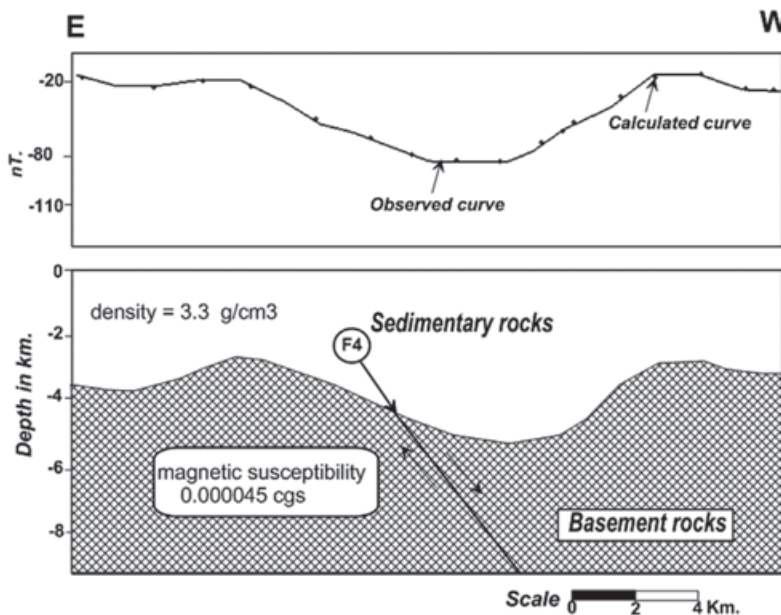


Figure 16. Two dimensions geomagnetic model along profile A2' - A2 of the land magnetic map.

Figure 17. Interpreted geoseismic structural cross-section along seismic line WQ85-51B.

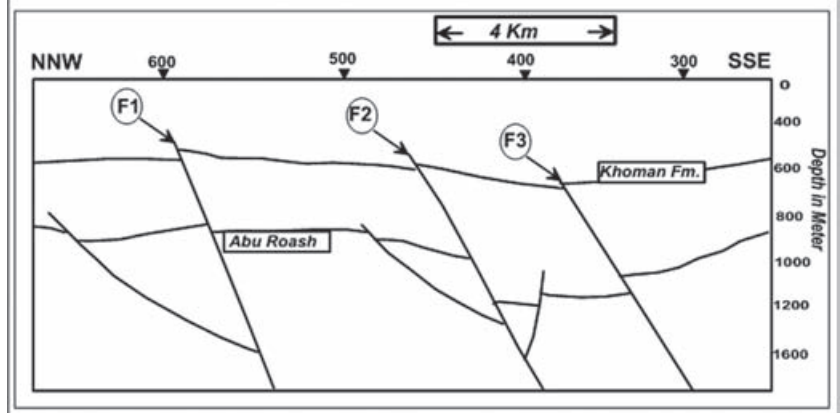
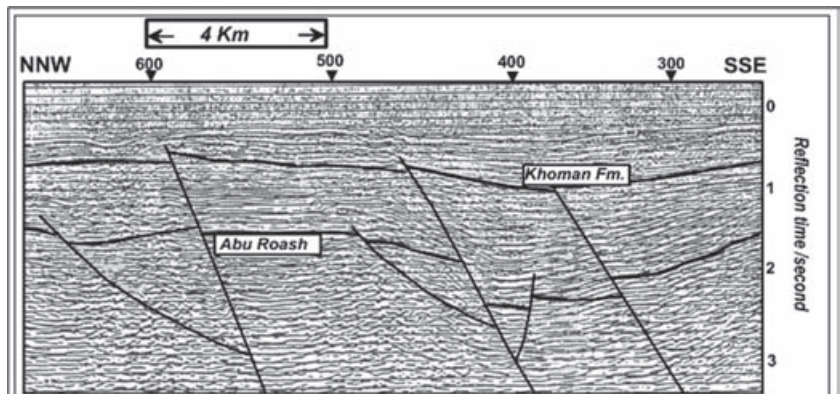
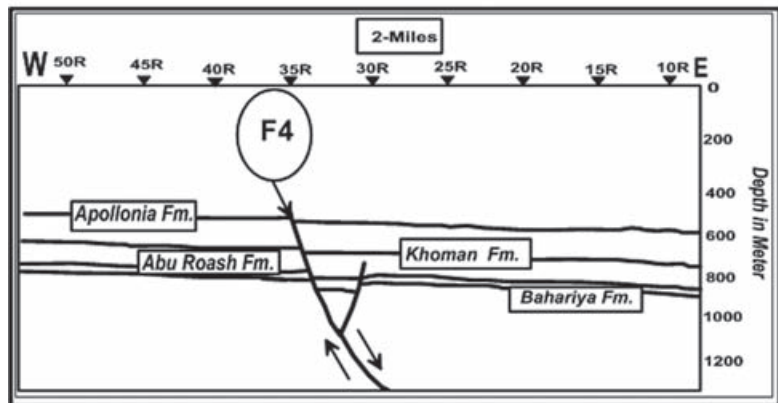
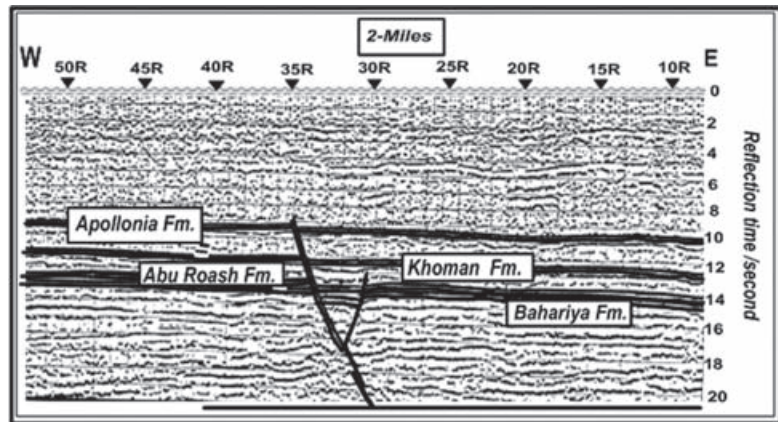


Figure 18. Interpreted geoseismic structural cross-section along seismic line No. (127).

Discussion and conclusions

In this study, a correlation carried out between the structures deduced from the geomagnetic data and the structures deduced from the seismic data. Accordingly an agreement and indicates that these structures are extending from the subsurface basement rocks upward to the sedimentary sequence. It proves the capability of the geomagnetic method to detect the structures of the basement rocks which extends to the overlying sedimentary rocks. This leads to the conclusion that the geomagnetic tool is an effective geophysical method in the fields of exploration and prospecting if we applied the suitable interpretation methods and techniques. The tectonic trends affecting the area are N35° - 45° W parallel to the Gulf of Suez, N45° - 65°E, related to the Syrian Arc tectonics, E - W belong to the Mediterranean and Aqaba trends.

Also, these structures trends are correlated fairly well with the results deduced from Euler method and the interpreted seismic sections. The depths to the basement rocks range between 3.1 and 4.3 km, which matched with the drilled wells in the study area.

The deduced fault structures, imply that all of them do not affect Quaternary or near surface rocks. This is also indicated from seismicity map of north-western Egypt compiled by ENSN. The possible interpretation for this outcome is that the study area is recently more stable than other adjacent areas in the northern parts of Egypt.

This work provides a guide line for any exploration process, and for establish any new towns or strategic projects in the area.

Bibliography

- Abdel Hady A.M., Kolkila A.A., Abdou M.F., 1988, Subsurface Aptian rocks in some parts of the North Western desert; their geologic setting and hydrocarbon potetiality, Egypt, *J. Geol.*, 32, 219-241.
- Badr El Din Petroleum Co., 2004, Seismic Survey at the northeastern part of Qattara Depression, internal report, Cairo, Egypt.
- Barakat M.G., 1982, General review of Petroliferous Provinces of Egypt with special emphasis on their geologic setting and oil potentialities. Petro. and Gas. Proj., Cairo Univ., M. I. T., p. 86.
- Baranov V., 1975, Potential field and their transformation in applied geophysics. Geoexploration Monograph, Series L, No. 6: Gerbruder Borntraeger, Berlin, Stuttgart, Germany.
- Båth M., 1974, Spectral analysis in Geophysics. Elsevier Scientific Publ. Company, Amsterdam, New York.
- Conoco and General Petroleum Corporation, 1987, Geological map of Egypt, Scale 1 : 500,000: Bernice, Cairo-Egypt.
- Egyptian General Petroleum Co-operation, 1979, Aeromagnetic map Scale 1 : 100000, General Petroleum company.
- GM-SYS. 1995, Gravity and magnetic modelling, version 3.6; Northwest Geophysical Association, Inc. (NGA), Corvallis, Oregon, U.S.A. 97339.
- Henderson R.G., 1960, A comprehensive system of automatic computation in magnetic and gravity interpretation, *Geophys.*, 30, 569-585.
- Hildenbrand T.G., 1983, Filtering program based on two dimensional Fourier analysis, A. U.S. Geological survey open-file report, 83-237, p. 31.
- Khalda Petroleum Co., 2000, Seismic Survey at Abu Senna basin southern part of Qattara Depression, internal report, Cairo, Egypt.
- Ku C.C., 1977, A direct computation of gravity and magnetic anomalies caused by 2- and 3-D bodies of arbitrary magnetic polarization by equivalent-point method. *Geophysics, Soc. of Expl. Geophys.*, 42, 610-622.
- Ku C.C., Sharp J.A., 1983, Werner deconvolution for automated interpretation and its refinement using Marquardt's Inverse Modeling. *Geophysics*, 28, 754-774.
- Nettleton L.L., 1976, Gravity and magnetic in oil prospecting. Mc-Graw- Hill Book Co, New York.
- Pasteka R., 2001, Comment on the structural index used in Euler deconvolution for the step structure in gravimetry. Extended abstracts from EAGE 63rd Conference and technical exhibition, Amesterdam, p. 211.
- Reid J.M., Allsop H. Granser, 1990, Magnetic interpretation in three dimentions using Euler deconvolution. *Geophysics*, 55, 80-91.
- Said R., 1990, The geology of Egypt. Balkemor Publishers, Rotterdam, Netherlands, 364-380.

Talwani M., Ewing M., 1960, Rapid computation of gravitational attraction of three-dimensional bodies of arbitrary shape. *Geophysics*, 25, 203-225.

Thompson D.T., 1982, EULDPH – A new technique for making computer-assisted depth estimates from magnetic data. *Geophysics*, 47, 31 – 37.

Zurflueh E.G., 1967, Application of two dimensional linear wavelength filtering. *Geophys.* 32, 1,015 - 1,035.

Werner S., 1953, Interpretation of magnetic anomalies at sheet-like bodies, *sveriges Geol. Undersok, Ser., C., Arsbok*, 6, 413 – 449.

Declining productivity in geothermal wells as a function of the damage effect

Alfonso Aragón Aguilar*, Georgina Izquierdo Montalvo, Víctor Arellano Gómez, Mahendra P. Verma and Ma. Guadalupe Belín Morales

Received: May 18, 2011; accepted: May 03, 2012; published on line: September 28, 2012

Resumen

La curva-tipo geotérmica afectada por daño sirve para determinar el efecto de daño en un pozo y para caracterizarlo. Esta metodología puede ser aplicada para determinar el efecto del daño en los pozos que no pueden ser retirados de la explotación continua. Comúnmente se emplean los análisis de las pruebas transitorias de presión, cuya ejecución es tardada. En los pozos analizados, el efecto de daño aumenta con su tiempo de explotación y está relacionado con el deterioro en la producción. El conocimiento del daño ayuda a la toma de decisiones acerca de las operaciones a aplicar en el pozo con el objeto de mejorar su productividad.

Palabras clave: factor de daño, productividad, declinación de la producción, diseño de la explotación, campo geotérmico, Los Azufres, Cerro Prieto.

Abstract

The inflow curve may be used to determinate the damage effect and wellbore characterization in geothermal fields. The methodology can be applied for determining damage effect in wells that cannot be retired from continuous exploitation. The skin or damage effect is usually estimated from transient pressure tests which require time. It was found that the damage effect in the wells increases with exploitation time and is related with deterioration of production. Knowledge of damage is needed for taking decisions about operations on the well for enhancement of productivity.

Key words: skin factor, damage effect, productivity, production decline, design exploitation, geothermal field, Los Azufres, Cerro Prieto.

A. Aragón Aguilar*
G. Izquierdo Montalvo
V. Arellano Gómez
M. P. Verma
Instituto de investigaciones Eléctricas
Calle Reforma 113
Col. Palmira, 62490
Cuernavaca Morelos
México
*Corresponding author: aaragon@iie.org.mx

Ma. Guadalupe Belín Morales²
Academia Mexicana de Ciencias
Km. 23.5 Carretera Federal México-Cuernavaca
Tlalpan, 14400
México D.F., México
Tel.: (52) 777 3623811 (ext. 7329)

Introduction

Production evaluations of geothermal wells are carried out periodically to characterize the well, and to establishing criteria for operation during continuous exploitation. Drawdown pressures from the reservoir to delivery points are calculated using nodal analysis (Flopetrol Johnston-Schlumberger, 2008). Figure 1 shows a schematic diagram of the pressure at different points p_e is the static pressure, r_e is the drainage radius, p_{wf} is the pressure at bottom-hole, r_{wf} is the radius of the well, p_{wh} is the pressure at well head and p_s is the pressure at the inlet of the separator.

Abnormal decreases in well pressure are caused by the increase of flow during output tests (Evinger and Muskat, 1942; Horner, 1951; Matthews *et al.*, 1954). Evinger and Muskat (1942) showed that the abnormal behavior in the drawdown pressure is related to deterioration of production.

Knowledge of the skin effect (Evinger and Muskat, 1942; Horner, 1951; and Ramey, 1970) during production is useful for taking decisions about operations such as cleaning, repairs, stimulations, etc.

The skin effect is synonymous to damage in a well and reduction of its production. A positive value of the skin effect indicates deterioration of the well. A zero value means that the well is in undisturbed state, and a negative one indicates improved conditions in the well. A decrease in production is a consequence of damage.

Vogel (1968) proposed an inflow performance relationship as follows:

$$Q_D = 1.0 - 0.2(p_D) - 0.8(p_D)^2 \tag{1}$$

where $Q_D = q/(q_o)_{max}$ is the dimensionless mass flow and $p_D = p/p_e$ is the dimensionless pressure.

Other authors, (Standing, 1970; Klins and Majcher, 1992; Iglesias and Moya, 1998; Moya *et al.*, 1998) proposed inflow performance relationships.

Damage effect related with production decline

Figure 2 shows the descriptive behavior of the pressure in the reservoir without skin (p_{wf}^*) and with skin (p_{wf}). It can be observed an additional drawdown of the pressure under presence of damage.

For incorporating damage effect into the inflow relationship, Aragón (2006); Aragón *et al.* (2008a) and Aragón *et al.*, (2008b) proposed following expression considering the main characteristics of geothermal systems:

$$M = \left(\frac{\ln \frac{r_e}{r_w} - 0.6603}{\ln \frac{r_e}{r_w} - 0.6603 + s} \right) \tag{2}$$

where r_e is the reservoir radius, r_w is the wellbore radius and s is the damage effect. The main considerations were the variation of the radii of the wells (r_w) between 2 and 3.5 inches (0.0508 and 0.0889 m). Due to the uncertainty of the drainage radius value (r_e), a sensitivity analysis of the behavior of the M factor against damage

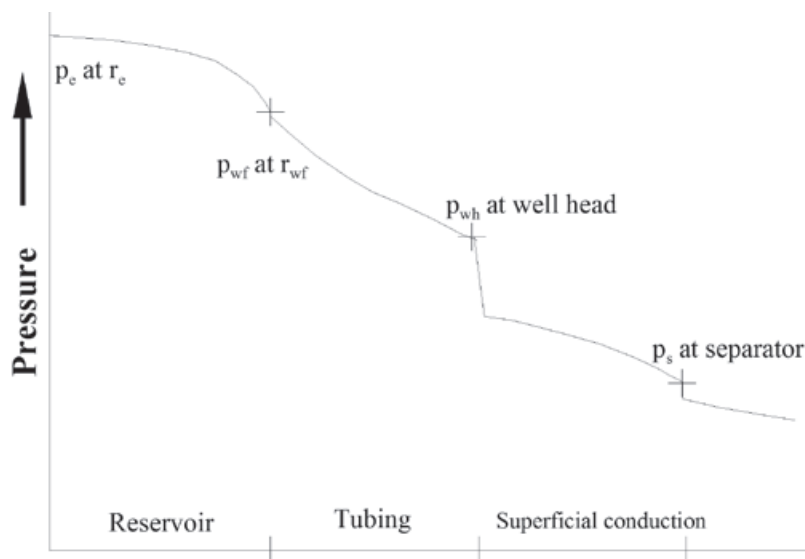


Figure 1. Behavior of the pressure at different points along the travel of the fluid between the reservoir and the final delivery.

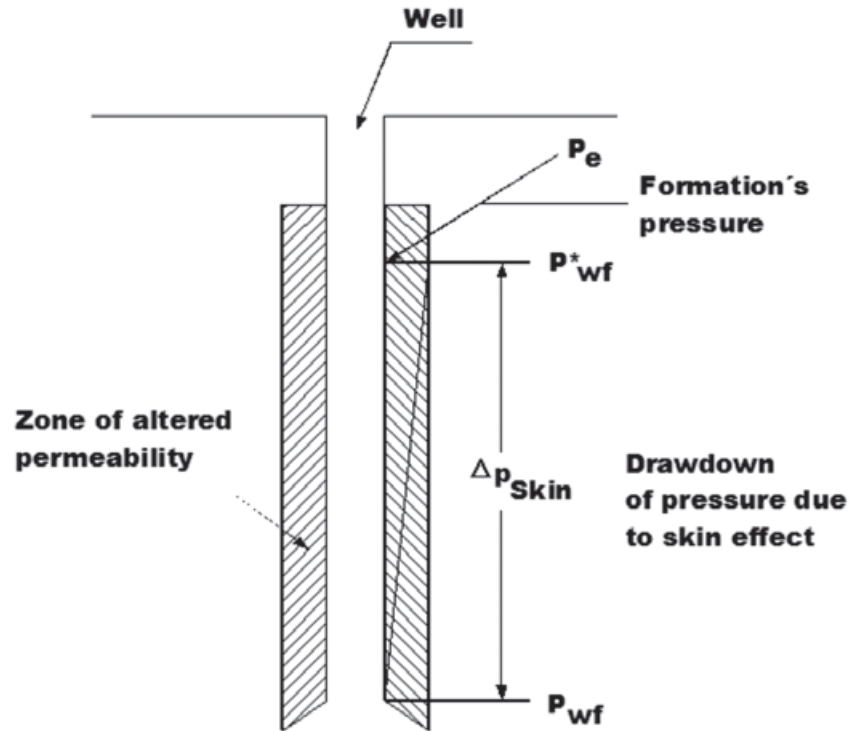


Figure 2. Pressure distribution in the reservoir for cases with and without damage effect.

effect for different values of r_c was done and the results are shown in Figure 3. The value of well radius (r_w) used in this equation is the common of the tubing in geothermal systems of 3.5 inches (0.0889 m).

Geothermal inflow performance relationships affected by damage

The general expression of geothermal inflow relationship affected by damage and considering the fluid as ternary mixture (Montoya, 2003; Meza, 2005) H_2O-CO_2-NaCl is:

$$p_D = M \left\{ 0.993 - 0.16(W_D) - 2.08(W_D)^2 + 3.95(W_D)^3 - 2.70(W_D)^4 \right\} \tag{3}$$

The graphic expression of the equation (3) is a family of curves, each one of these, representing different damage values and is called as the geothermal inflow type-curve affected with damage. The type curve is shown in Figure 4 and is being applied for determining the damage effect in wells using their production data measured at different flow rates.

For using the measured data of the well with this type-curve it is necessary to adequate them to bottom-hole conditions. It is achieved through the use of a flow simulator.

The geothermal inflow type-curve used with practical cases

For showing that the methodology can be applied in any geothermal field, two representative Mexican fields were selected; Los Azufres geothermal field which is located inside the Mexican Neovolcanic Belt, (volcanic formation) and the Cerro Prieto geothermal field as an example of sandy formation. The location of both fields is shown in Figure 5. Examples of how to use the geothermal inflow type curve are shown using data of production wells of these two fields. Representative wells of both geothermal fields were chosen.

Case 1

The described methodology for determining the value of the damage effect in geothermal wells, was applied using production data (Iglesias *et al.* 1985; Hiriart and Gutiérrez-Negrin, 1998) of well A-13 at Los Azufres, geothermal field. The analyzed well of this field was chosen due to its representative characteristics of the field. The

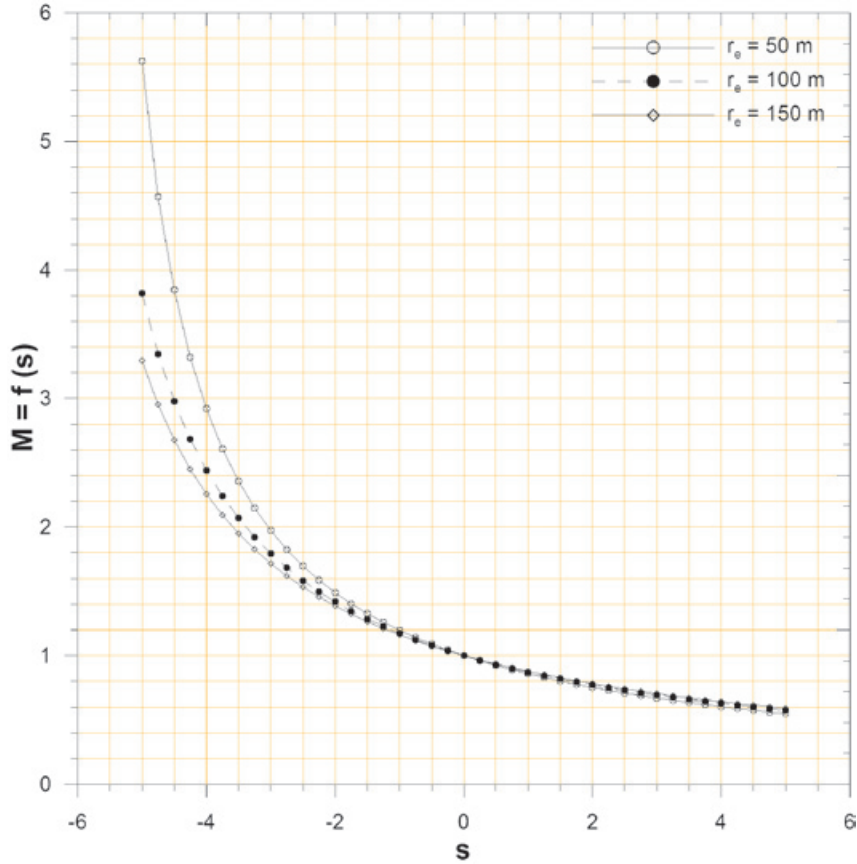


Figure 3. Performance of the M factor as function of the damage value (s), for different values of the reservoir drainage radius (r_e).

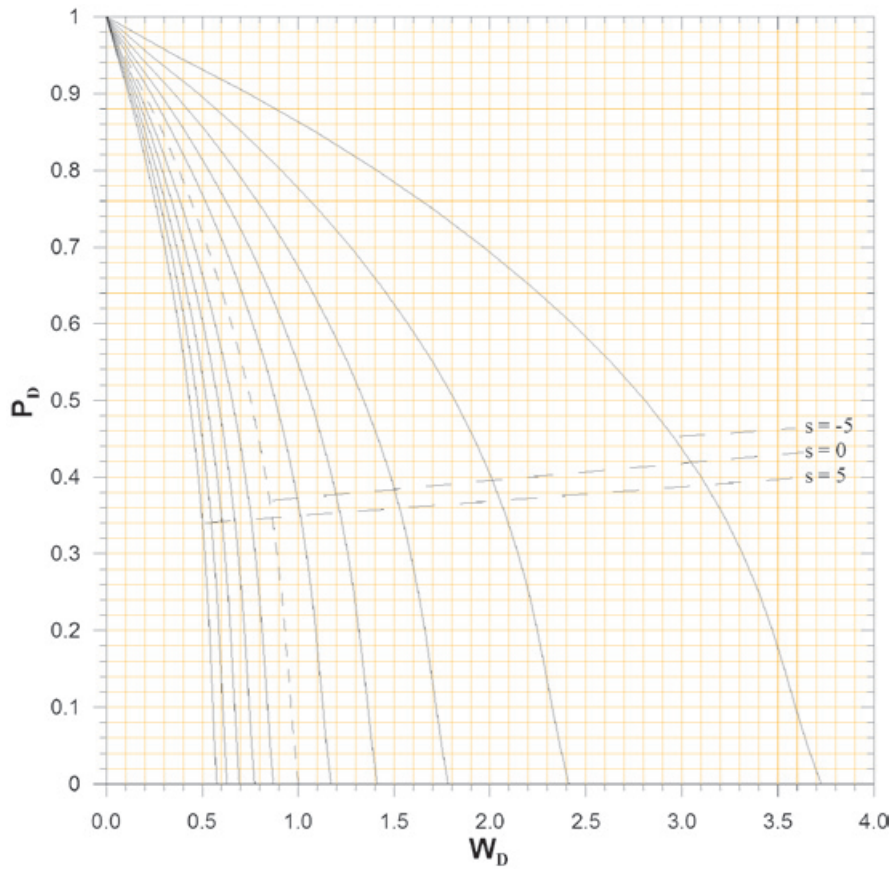


Figure 4. Geothermal inflow type curves for determining the damage effect in wells, using data of production measurements.

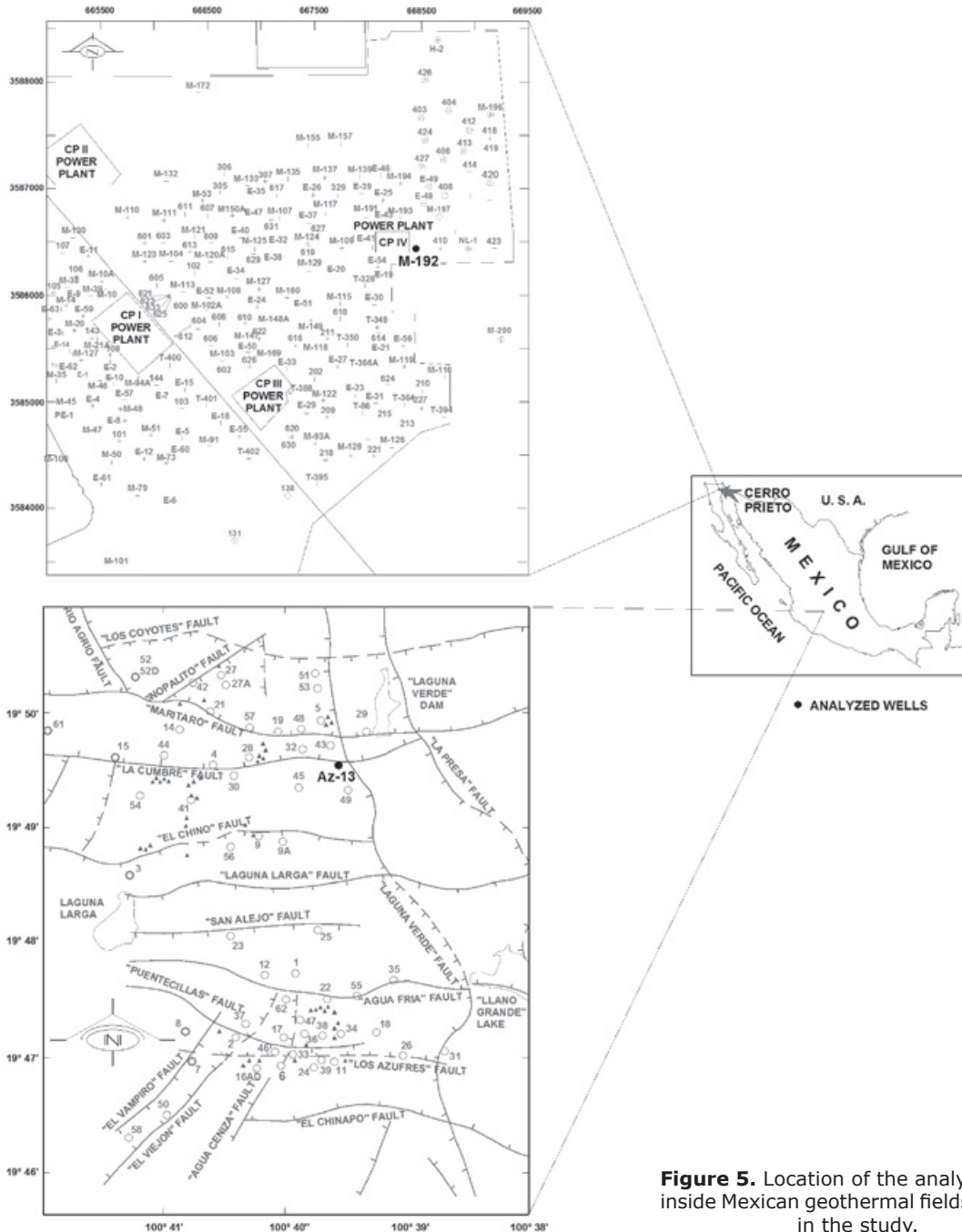


Figure 5. Location of the analyzed wells inside Mexican geothermal fields involved in the study.

production of this well is mainly a two phase flow. The selected data correspond to initial conditions and after different times of continuous exploitation. Through the knowledge of the initial conditions in the well, and its subsequent behavior it was feasible to identify its decline due to the continuous exploitation.

Figure 6 shows the characteristic production curves of the well at initial conditions and after different times of its continuous exploitation. The measured data were taken at wellhead conditions, so that the well flow simulation pro-

gram (PBPower, 2005) was used to determine the variable values at bottom-hole conditions.

Dimensionless values of pressure and flow rate were calculated for each one of the measurements done during the output tests. Therefore by applying the methodology, the value of the damage, is determined by identifying that curve where the dimensionless values (W_{Dr} , p_D) are located. Figure 7 shows the graphs using the geothermal inflow type-curve and the dimensionless data sets of three output tests carried out in this well.

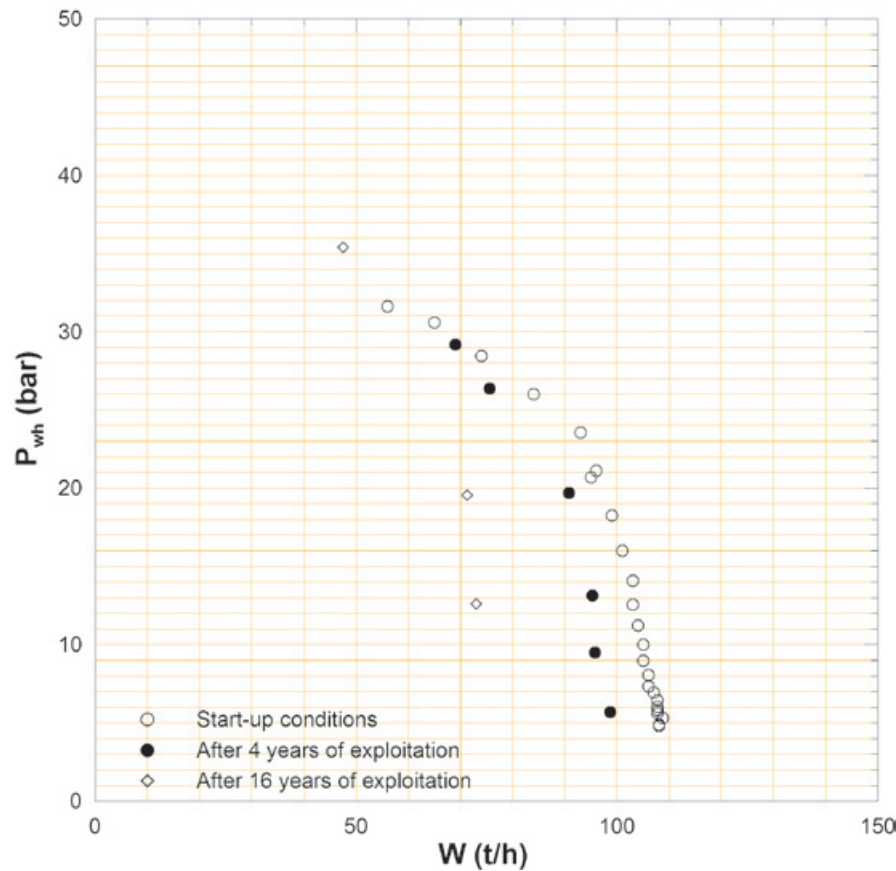


Figure 6. Production characteristic curves of well A-13 of the Los Azufres geothermal field, at its initial conditions, and after 4 and 16 years of continuous exploitation.

From last figure, it can be noticed that the determined values of the damage effect, is -2.1 for initial conditions, of -1.9 after 4 years and of 0.5 after 16 years of continuous exploitation. The decrease both in pressure (p) as in mass flow (W) were determined by year, taking into account the interval times between measurements. The found negative values of Δp and ΔW , are related to the decline productivity of the well.

Case 2

Production measurements of well M-192 (Ribó, 1989) taken as representative for the Cerro Prieto geothermal field were analyzed following this methodology. This well is located in the area of CP IV zone (Figure 4). The analysis was carried out at initial conditions and after six years of continuous exploitation. The output characteristic curves of this well are shown in Figure 8. The determination of the damage effect in this well is shown in Figure 9. As can be seen in this figure, the determined damage effect in this well was of -3.6 for initial conditions and of 1.5 after six years of continuous exploitation.

Table 1 summarizes a correlative analysis of the behavior of the pressure, mass flow rate and

damage effect, respect to exploitation time of the analyzed wells.

Discussion results

From a sensibility analysis of Equation (2), it is possible to deduce that the values of the reservoir's drainage radius (r_c) do not produce great variations of the M factor.

For initial conditions in the wells, the damage value is negative, mainly due to the washing operations applied at their completion stage. The negative value of the damage effect is equivalent to obtain beneficial conditions in the well. Accordingly, it was found there is relation between the obtained damage values and the time of operative life of the well at date of the production measurements. It seems that in the analyzed wells, the values of the damage effect increase due to their decline. Through comparison of the characteristic production curves obtained at different stages of the productive life of the well, it can be noticed the decline in its productive properties (see Figures 6 and 8). In summary it can be seen the decrease in the productive characteristics of analyzed wells, as a function of their exploitation time.

The obtained results (Table 1), indicate that damage effect is related with the well decline. It is important to emphasize that both analyzed wells show that while the damage effect increases, their productive characteristics diminish. The last two columns of Table 1 show the yearly decrease of pressure and mass flow rate and as mentioned before, these variables decrease with exploitation time.

Table 1. Behavior of the production parameters analyzed through the production tests carried out at different stages in well A-13 of Los Azufres geothermal field and in M-192 of Cerro Prieto geothermal field.

Well	Production time (years)	p_{wf} (Bar)	W_{max} (t/h)	S Damage	$-\Delta p/year$ (Bar/yr)	$-\Delta W/year$ (t/h)/yr
A-13	0	58.7	110	-2.1		
	4	55.1	103	-1.9	.9	1.8
	16	52.2	86	0.5	.73	4.3
M-192	0	315	475	-3.6		
	6	207	350	1.5	18	20.8

It is important to take into account, the magnitude of the change of the production variables in Los Azufres and in Cerro Prieto geothermal field. So, the mean mass flow rate (W) in Cerro Prieto wells is twice higher than that of wells in Los Azufres. Similarly the mean value of bottom-hole flowing pressure (p_{wf}) is more than three times higher in Cerro Prieto wells, than at Los Azufres wells.

The values of the damage effect, of the analyzed wells, increase with the exploitation time (Figures 7 and 9). In general, the results of the values of the calculated damage effect show an increase, which is related with its exploitation period (Table 1). Taking the total of analyzed period time of each well, it can be found that yearly variation of the damage effect for the well of Los Azufres is of 0.1625, however for the well of Cerro Prieto is of 0.85.

Conclusions

From the study carried out the main conclusions are:

The obtained results support the feasibility for apply this methodology in geothermal fields with any rock formation type.

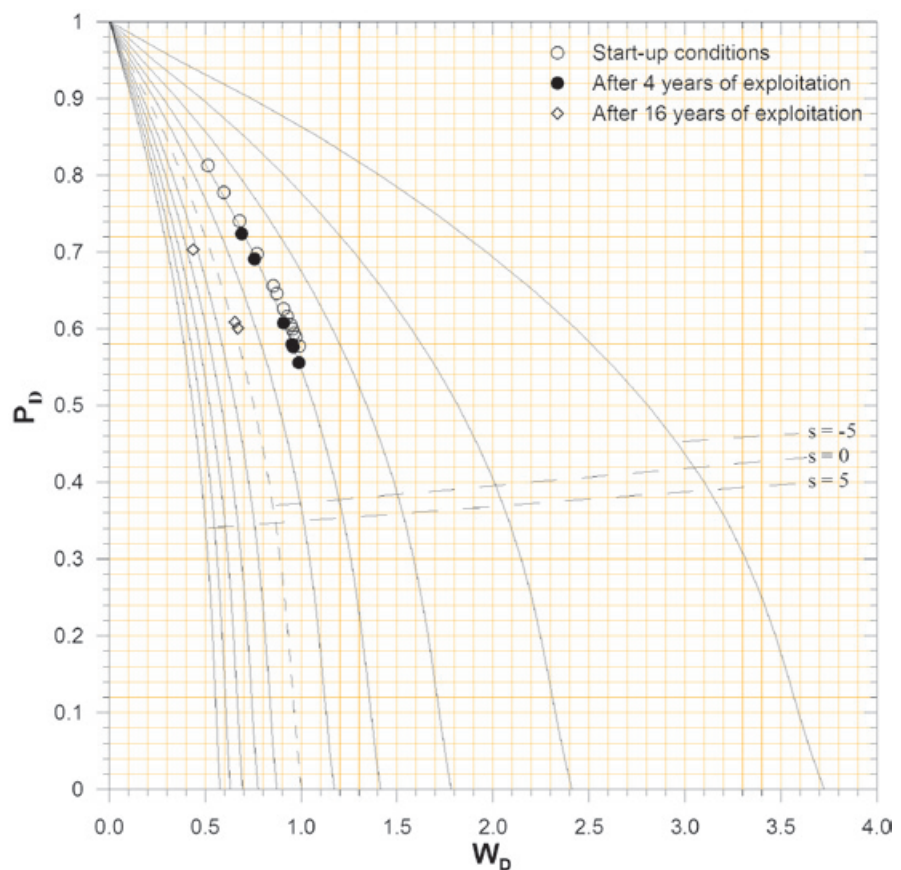


Figure 7. Application of the geothermal inflow type-curve, for determining the damage effect using data set of output tests, taken at different exploitation times, in the well A-13 of the Los Azufres México geothermal field.

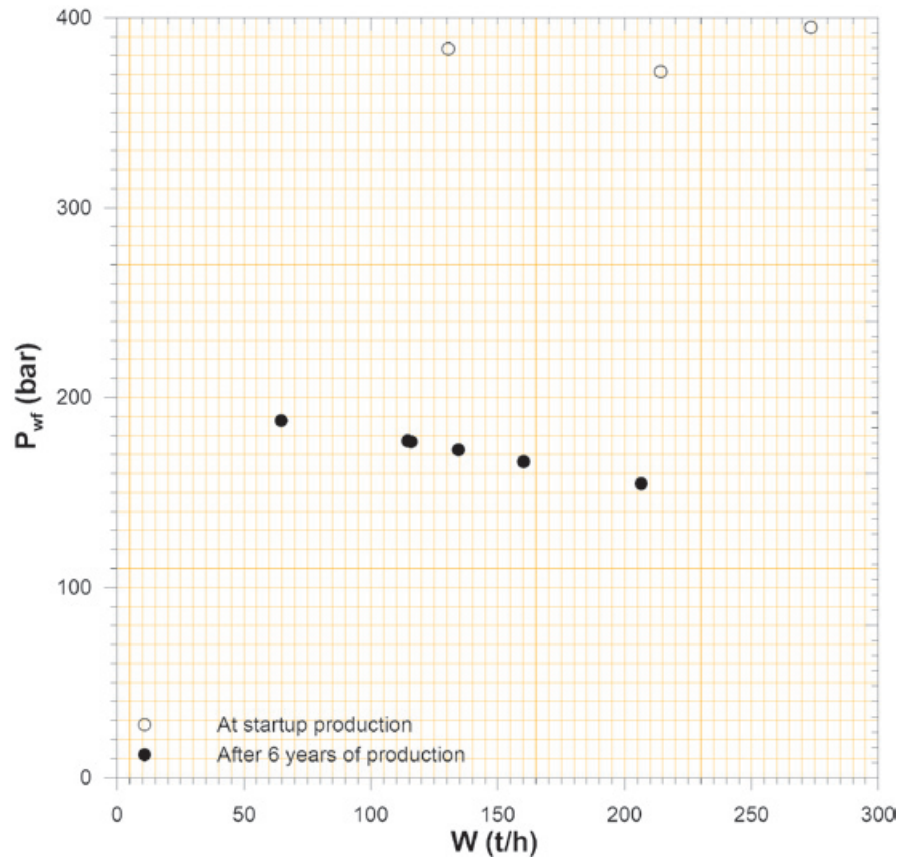


Figure 8. Production characteristic curves of well M-192, taken at its initial conditions and after six years of continuous exploitation time.

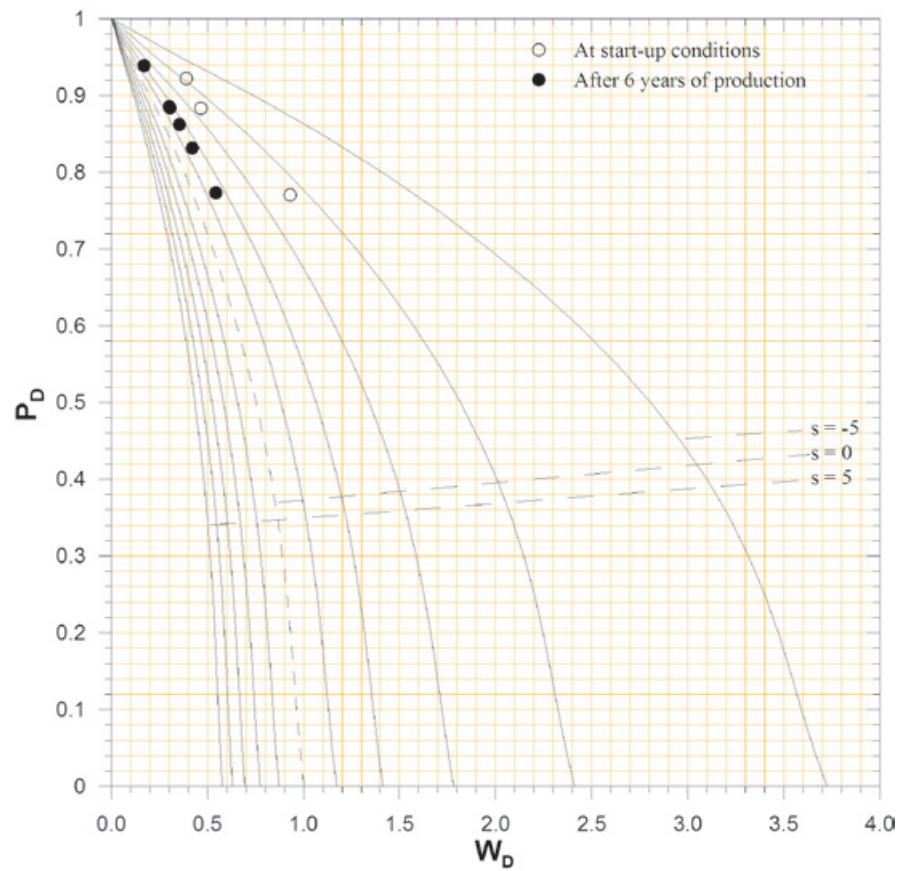


Figure 9. Determination of the damage effect, from the use of the geothermal inflow type curve with the measurements carried out in well M-192 at its initial conditions and after six years of continuous of continuous exploitation.

The results indicated that inflow performance relationships can be used as a technical tool for characterizing the wells productivity at initial conditions and at different stages of their operative life.

According with the obtained results, the geothermal inflow type curve can be taken as an alternative tool for determining the damage in wells that do can not be retired from the continuous system exploitation.

The numerical value of the damage effect determined in the analyzed wells increases as function of the exploitation time, being it an indicative parameter of the diminution of the productive characteristics of the well.

The knowledge of the damage effect allows support to decisions in order to apply the appropriate remediation operations in wells, such as cleanings, repairs, stimulations, etc., for enhancement of their productivity.

The applied methodology allows the characterization of the decline of production parameters (W , p_e) of wells. This knowledge is useful for taking the best decisions in the establishment of the wells exploitation designs.

An important topic for future research in this area is the study of yearly behavior of damage effect found in the well of Cerro Prieto that differs greatly from that determined at the well of Los Azufres. Emphasizing that the first corresponds to sandy formation system and the other one is in volcanic formation.

Nomenclature

Capital letters

M Factor incorporated in the inflow relationships

Q Volumetric flow rate

W Mass flow rate

Lower case letters

p Pressure

q Flow rate

r Radius

s Damage effect

Subindex

D Dimensionless value

e Referred to reservoir conditions

max Maximum conditions

o Referred to oil

s Referred to separator conditions

w Referred to well

wf Referred to flowing conditions

wh Referred to wellhead conditions

Greek symbols

Δ Gradient

Acknowledgements

The authors thank to authorities of IIE and CFE for the support in the development of this research. Also express their gratitude to Dr. Cinna Lomnitz, and anonymous reviewer whose contributions helped to improve this paper.

Bibliography

- Aragón A.A., 2006, La influencia del factor de daño en curvas-tipo de flujo geotérmico y su impacto en el diagnóstico de permeabilidades. Tesis Doctoral, CENIDET, (Centro Nacional de Investigación y Desarrollo Tecnológico) SEP, Cuernavaca, Morelos, México, 103 p.
- Aragón A., Moya A.S., García-Gutiérrez A., 2008a, Inflow performance relationships in geothermal and petroleum reservoir engineering: A review of the state of the art. *Geothermics*, 37, 635-650.
- Aragón A., Moya S.L., Suárez C., 2008b, Determination of the Damage Effect in Geothermal Wells using Inflow Type Curves, Chapter 7 of "Geothermal Energy Research Frontiers", Nova Science Publishers, Inc. ISBN: 1-60021-683-8, 163 – 201.
- Evinger H.H., Muskat M., 1942, Calculation of theoretical productivity factor. *Trans., AIME*, 146, 126-139.
- Flopetrol Johnston-Schlumberger, 2008, Oilfield Review Winter 2008, 20, 3.
- Hiriart L.G., Gutiérrez-Negrín L.C., 1998, Resultados de la explotación geotérmica en México, en 1997. *Geotermia, Revista Mexicana de Geoenergía*, 14, 2, 71-77.

- Horner D.R., 1951, Pressure build-up in wells, Proc. Third World Petroleum Congress, Section II, E. J. Brill Leiden, p. 503.
- Iglesias E.R., Arellano G.V., Garfias A., Miranda C., Aragón A., 1985, The natural thermodynamic state of the fluids in the Los Azufres geothermal reservoir, Proceeding 10th Workshop on Geothermal Reservoir Engineering, Stanford University, Stanford Cal. U.S.A., January 22-24, p. 241-246.
- Iglesias E.R., Moya S.L., 1998, Applicability of Geothermal Inflow Performance Reference Curves to CO₂-Bearing Reservoirs, *Geothermics*, 27, 3, 305-315.
- Klins M.A., Majcher M.W., 1992, Inflow performance relationships for damaged or improved wells producing under solution-gas drive. *Journal Pet. Tech.*, SPE-AIME, 1357-1363.
- Matthews C.S., Brons, F., Hazebrook, P., 1954, A method for determination of average pressure in a bounded reservoir. *Trans.*, AIME, 201. p. 182-191.
- Meza C.O., 2005, Efecto de la precipitación de sales en el diagnóstico de permeabilidades rocosas. Tesis de maestría, CENIDET, (Centro Nacional de Investigación y Desarrollo Tecnológico) SEP, Cuernavaca, Morelos, México, 107 pp.
- Montoya D., 2003, Estimación de permeabilidades de yacimientos geotérmicos mediante la aplicación de curvas tipo de influjo geotérmico. Tesis de maestría, CENIDET, (Centro Nacional de Investigación y Desarrollo Tecnológico) SEP, Cuernavaca, Morelos, México, 112 pp.
- Moya S.L., Aragón A., Iglesias E., Santoyo E., 1998, Prediction of Mass Deliverability From a Single Wellhead Measurement and Geothermal Inflow Performance Reference Curves, *Geothermics*, 27, 3, 317-329.
- PBPower Geothermal Resources, 2005, WELLSIM, Software package, New Zealand, <http://software.pbpower.net/>
- Ramey H.J., Jr., 1970, Short-time well test data interpretation in the presence of skin effect and wellbore storage. *Journal Petroleum Tech.*, 97-104.
- Ribó M.O., 1989, Análisis de pruebas de presión en pozos de Cerro Prieto, in Proceedings Symposium in the field of geothermal energy, Agreement between Comisión Federal de Electricidad (México) and Department of Energy (DOE) of USA, San Diego Cal., U.S.A., p. 123-129.
- Standing M.B., 1970, Inflow performance relationships for damaged wells producing by solution-gas drive. *Journal Pet. Tech.*, 1399-1400.
- Vogel J.V., 1968, Inflow performance relationships for solution gas drive Wells. *Journal Pet. Tech.* SPE 1476 Annual Fall Meeting of Society of Petroleum Engineers, Dallas Texas, USA, 66-79.

Applicability of attenuation relations for regional studies

Anand Joshi*, Ashvini Kumar, Cinna Lomnitz, Heriberta Castaños and Shahid Akhtar

Received: August 31, 2011; accepted: May 23, 2012; published on line: September 28, 2012

Resumen

El siguiente trabajo analiza las aplicabilidades de diferentes ecuaciones predictivas del movimiento del suelo en estadios regionales. Para ello se han utilizado las gráficas cumulativas de probabilidad y de residuales. Tanto la normalidad como la adecuación del modelo están conformes siempre que los conjuntos de datos sean similares; sin embargo, cuando el modelo se utiliza para la predicción de datos en diferentes regiones existe desviación de la normalidad. Por ejemplo, un conjunto de datos provenientes de sismos en los Himalayas registrados en una red sísmica fue predicha mediante las ecuaciones de Abrahamson y Litehiser (1989), de Boore y Atkinson (2008), de Boore *et al.* (1997) y de Joyner y Boore (1981) y resulta que estos modelos presentan el efecto "fat tail" y amplias desviaciones de adecuación. Por otra parte, si se utiliza el modelo que hemos derivado a base de datos de los Himalayas la predicción es normal y adecuada. Finalmente, se examina la dependencia de las ecuaciones predictivas de los mapas de zonificación sísmica regionales. Se obtuvo un mapa de 10% de probabilidad de excedencia para una aceleración pico de 0.1g con el método de Joshi y Patel (1997) y se encontró que el mapa resultante era similar cuando se empleaban dos ecuaciones predictivas basadas en datos de los Himalayas; en cambio, usando la ecuación de Abrahamson y Litehiser (1989) los resultados eran discordantes.

Palabras clave: normalidad, residual, predicción sísmica, Himalaya.

Abstract

This paper discusses the applicability of different ground motion prediction equations (GMPE) for regional studies. Cumulative probability plots and residual plots are used to check the normality and model inadequacies in various GMPE. It is seen that as long as the data set is similar to that used for generating GMPE the normality and model adequacies are broadly satisfied. However, clear deviation from normality is observed when using GMPE for predicting different data sets. In order to check utility of various worldwide GMPE for dataset other than that used for preparing GMPE, the dataset of Himalayan earthquakes recorded on strong motion network has been predicted using the GMPE given by Abrahamson and Litehiser (1989), Boore and Atkinson (2008), Boore *et al.* (1997) and Joyner and Boore (1981). It is seen that these GMPE shows presence of fat tails together with large model inadequacies when they are used for predicting Himalayan data. The data for Himalayan earthquake are also predicted by using the GMPE developed using Himalayan data. It is seen that this GMPE obeys normality and does not reflect any model inadequacies. The dependency of GMPE on the seismic zonation map of the region is also checked in this work. The seismic map for 10% probability of exceedence of peak ground acceleration of 0.1g is prepared using modified method given by Joshi and Patel (1997). It is seen that two different regional GMPE developed using Himalayan dataset gives similar seismic zonation map however large deviation in the seismic zonation map is observed when GMPE given by Abrahamson and Litehiser (1989) has been used.

Key words: normality, residual, seismic, Himalaya.

A. Joshi*
A. Kumar
Department of Earth Sciences
Indian Institute of Technology Roorkee
Roorkee, India
*Corresponding author: anushijos@yahoo.co.in

C. Lomnitz
Instituto de Geofísica
Universidad Nacional Autónoma de México
Ciudad Universitaria
Delegación Coyoacán, 04510
México, D.F., México

H. Castaños
Instituto de Investigaciones Económicas
Universidad Nacional Autónoma de México
Ciudad Universitaria
Delegación Coyoacán, 04510
México, D.F., México

Introduction

An evaluation of seismic hazards, whether deterministic (scenario based) or probabilistic, requires an estimate of the expected ground motion at the site of interest. The most common mean of estimating expected ground motion in the probabilistic seismic hazard analysis (PSHA), depends on use of ground motion prediction equation (Campbell, 1981). A ground motion prediction equation (GMPE) or ground motion model as seismologists prefer to call it is a mathematical based expression that relates a specific strong motion parameter of ground shaking to one or more seismological parameters of an earthquake. The ground motion prediction equation includes a random residual, which can be specified in term of its statistical parameters like mean value and standard deviation. Early works related to the development of GMPE does not include ground motion variability (Bommer and Abrahamson, 2006). McGuire (1976) has published many GMPE which do not report associated standard deviation. The inclusion of ground motion variability became standard at the beginning of the 1980's (e.g., Campbell, 1981; Joyner and Boore, 1981).

New attenuation models for shallow crustal earthquake in the Western United States and similar active tectonic regions have been developed under Next Generation of Ground Motion Attenuation Models (NGA) project by Power *et al.* (2008). Five set of ground motion models have been developed under this project. The five NGA models developed by Power *et al.* (2008) are compared with respect to data set utilized, model parameterizations and ground motion predictions by Abrahamson *et al.* (2008). Selection of appropriate GMPE for any seismological and engineering use plays an important role for any new region. It is seen that almost all parts of the world do not have sufficient strong motion data from which GMPE solely based on instrumental data from a small geographical area can be derived (Douglas, 2011). Validity of GMPE derived from data of similar tectonic setup is confirmed by Douglas (2011) for regional studies. Douglas (2011) conclude that although some regions seem to show considerable differences in shaking it is currently more defensible to use well-constrained models, possibly based on data from other regions, rather than use local, often poorly constrained, models.

This paper discusses the deviation of normality and model inadequacies in the worldwide GMPE when they are used to predict regional Himalayan data. The GMPE's based on worldwide data prepared by Abrahamson and Litehiser (1989), Boore *et al.* (1997), Boore and Atkinson

(2008), Joyner and Boore (1981) has been used to check its deviation from normality and model adequacies for predicting values other than that used for its preparation. The GMPE's prepared from the Himalayan data has been used further to check its deviation from normality and model adequacies.

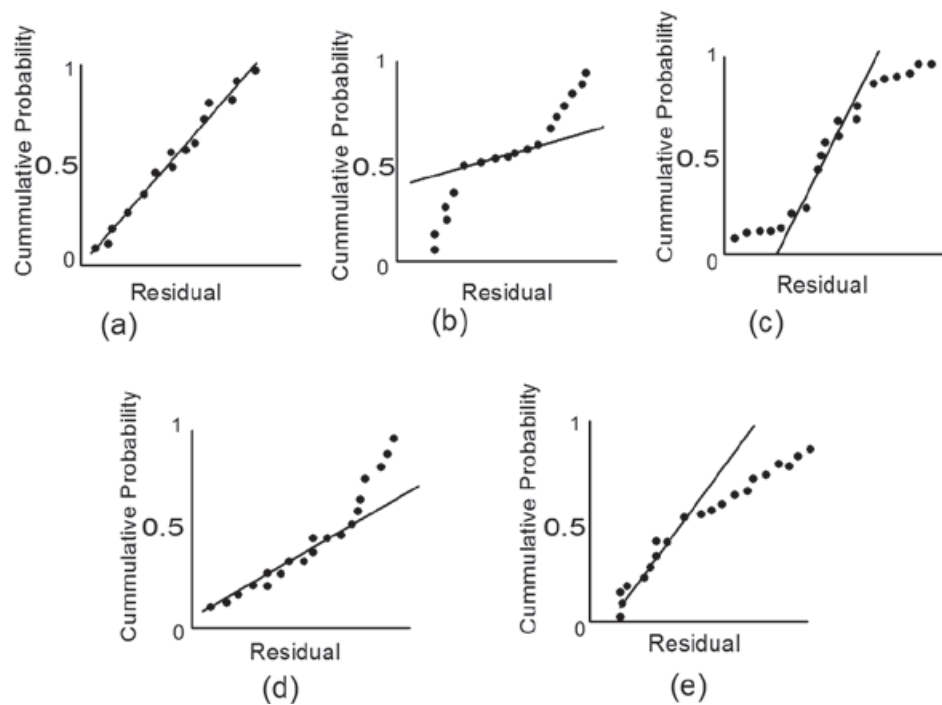
Residual in GMPE: Concept

Ground-motion prediction equation (GMPE) can be expressed in the following form (Campbell, 1981) as:

$$Y = b_1 f_1(M) f_2(R) f_3(M, R) f_4(P_i) \epsilon \quad (1)$$

Where, Y is the strong motion parameter to be predicted, $f_1(M)$ is a function of the magnitude scale M ; $f_2(R)$ is a function of distance parameter R ; $f_3(M, R)$ is a joint function of M and R ; $f_4(P_i)$ is a function representing parameter of earthquake, path, site, or structure and ϵ (epsilon) is the random residual representing the uncertainty in Y (Campbell, 1981). The random residual is usually assumed to be log normally distributed (Campbell, 1981). A posteriori empirical justification in support of a lognormal distribution for random residual comes from statistical tests on the observed scatter about the predicted value of Y (Esteva, 1970; Donovan, 1973; McGuire, 1977, 1978; Campbell, 1981). It is assumed that random residuals behave normally for all computations related to the ground motion variability. Deviation of this random residual with respect to normality is one of the main causes of presence of fat tail in the distribution function. A simple method of checking nonlinearity assumption is to construct a plot of cumulative probability with respect to residuals plotted in an increasing order. This graph is a straight line for normal distribution as shown in Figure 1(a). A sharp upward and downward curve at both ends in Figure 1(b) indicates that the tail of this distribution is too heavy to be considered as normal distribution. Flattening at the extreme end shown in Figure 1(c), which is a typical pattern from a distribution with thinner tail. The patterns associated with positive and negative skew are shown in Figure 1(d) and 1(e), respectively. Small departures from normality assumption do not affect the model greatly, but gross nonlinearity is potentially more serious. If the errors come from a distribution with thicker or heavier tails than the normal, the least square fit may be sensitive to a small subset of data. Heavy tail distribution often generates outliers that pull the least square fit too much in their direction. The random residual also plays an important role in deciding several types of model inadequacies. The model inadequacies in the GMPE are checked by plotting random variable

Figure 1. Normal probability plots (a) ideal; (b) heavy-tailed distribution; (c) light-tailed distribution; (d) positive skew; (e) negative skew. (Modified after Montgomery *et al.* 2003).



versus predicted parameter. If the plot of random residuals versus predicted parameter shows the data points within a horizontal band then there are no obvious model defect. The model inadequacies in this plot are shown by deviation in this plot.

Data Set:

A network of eight stations has been installed in the Pithoragarh region of Kumaon Himalaya under a major seismicity project sponsored by the Department of Science and Technology, India. Accelerographs have been installed in an area of 11,812 sq. km in the Pithoragarh and adjoining region. This network had recorded several events in this region since March, 2006. The hypocentral parameters of events recorded at three or more than three stations have been determined using HYPO71 software originally developed by Lee and Lahr (1972). Those events which are recorded at one and two stations are also used in the present work after calculating hypocentral distance from S-P time in the record. Location of these eight stations along with the geology of the region is shown in Figure 2. Three-component force balance accelerometer has been installed at each station. The threshold level of instrument was set at a very low threshold of 0.005% of full scale in order to have nearly continuous digital recording mode. The sensitivity of instrument is 1.25V/g and full scale measurement is 2.5V. This means the instrument has very low threshold of 0.1 gal. The purpose of such a low threshold level is to record almost every possible local events in small

span of time i.e., March 2006 to March 2008. Sampling interval of digital data is kept at 0.01 sec. The minimum inter station distance between these stations is approximately 11 km. The records collected from the accelerograph have been processed using the procedure suggested by Boore and Bommer (2005). The processing steps involve baseline correction, instrumental scaling and frequency filtering.

Magnitude is one of the most important dependent parameters required for any regression analysis. Keeping in view of the saturation of m_b , M_s and M_L scales, M_w scale has been used in the present work. In order to calculate M_w , seismic moment is calculated from the source spectrum at each station calculated after correcting the entire record for geometrical and anelastic attenuation. The S phase has been used from each record and is corrected for geometrical and anelastic attenuation term. The quality factor $Q_\beta(f) = 112f^{0.97}$ obtained for the nearby region of the Garhwal Himalaya by Joshi (2006) has been used for calculating source displacement spectra for all records. The calculated seismic moment is converted into moment magnitude using the following relation of Kanamori (1977):

$$M_w = \frac{2}{3} \log_{10}(M_o) - 10.7 \quad (2)$$

Distribution of PGA with hypocentral distance is shown in Figure 3(a) and it shows that

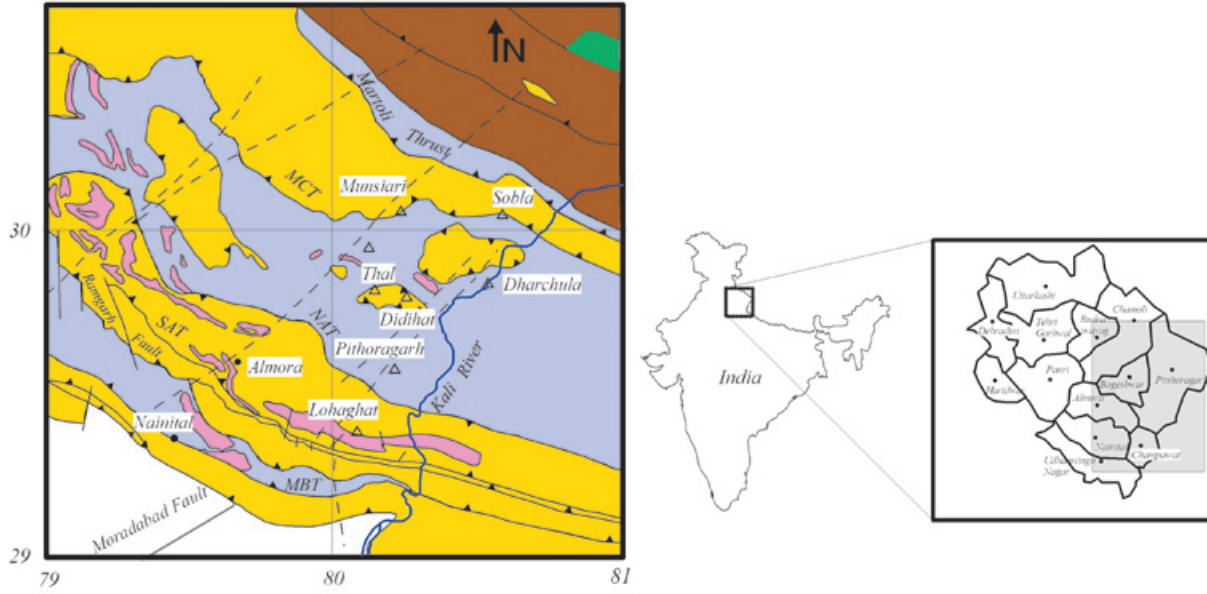


Figure 2. The Geological map of the Uttarakhand Himalaya (Modified after GSI, 2000). Location of strong motion recorders in the Uttarakhand Himalaya. Empty triangle denotes the stations maintained by the National Geophysical Research Institute and Department of Earth Sciences, Indian Institute of Technology, Roorkee.

hypocentral distance of the data set lies in a range between $4 \leq R \leq 151$ km and most of data lies in range 10-100 km. Distribution of magnitude with hypocentral distance is shown in Figure 3(b) and it shows that magnitude range of data is $3.5 \leq M_w \leq 5.3$.

Data set used in the present paper includes 130 accelerograms recorded by eighty two earthquakes. These records have been obtained from this network of eight stations operating in the Uttarakhand Himalaya between 2006 to 2008. This dataset has been used to obtain GMPE

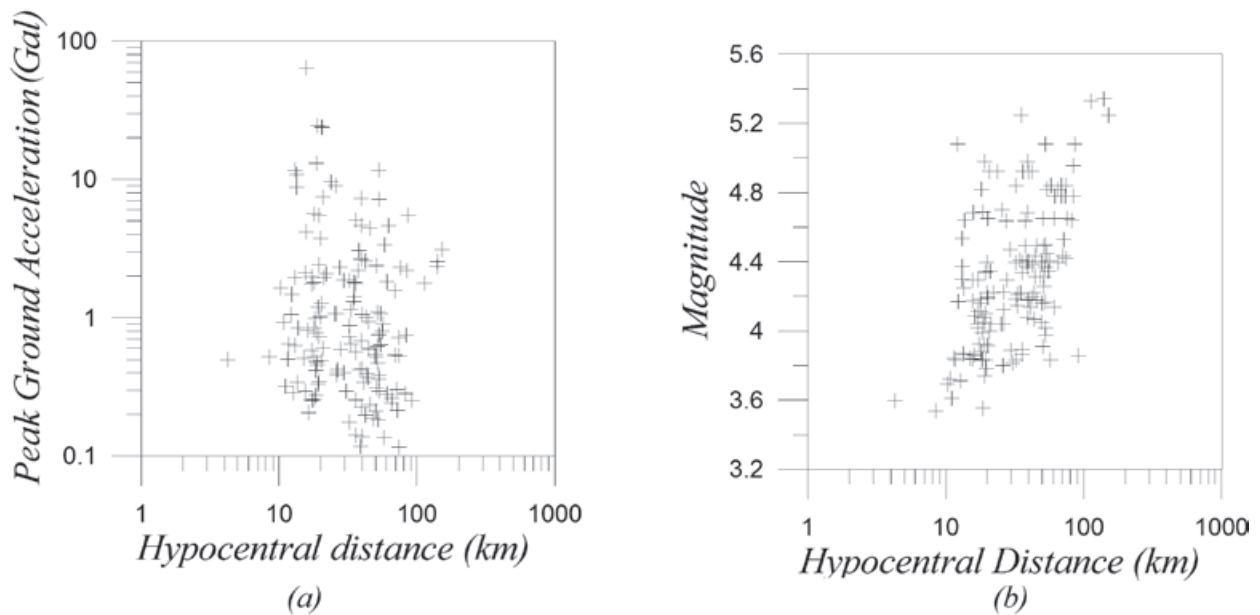


Figure 3. Distribution of (a) PGA with hypocentral distance and (b) Moment magnitude with hypocentral distance of the recorded data of Kumaon array.

using damped least square inversion method. The obtain relation is based on regression model given by Joshi *et al.* (2011). This relation is given as:

$$\ln(PGA) = -0.336 + 2.58 M_w + .018r - 2.96 \ln(r + 15) \quad (3)$$

Where, PGA is maximum peak ground acceleration in Gal, M_w is moment magnitude and 'r' is the hypocentral distance in km. Root mean square error between logarithm observed and estimated PGA obtained from this relation is 0.98 and standard deviation in the PGA is 0.82.

In an attempt to check the dependency of distance parameter on obtained GMPE we have introduced term epicentral distance '(E+15)' in place of '(r+15)' in the GMPE given in eq (3). This gives following form of GMPE from same data:

$$\ln(PGA) = -5.8 + 2.62 M_w - 0.16 \ln r - 1.33 \ln(E + 15) \quad (4)$$

Where in this relation, PGA is maximum peak ground acceleration in Gals observed in the horizontal component, M_w is the moment magnitude, 'r' is the hypocentral distance and E is the epicentral distance in km. Root mean square error between logarithm observed and estimated PGA obtained from this relation is 0.87 and

standard deviation in the PGA is 0.42, which is less than that observed in GMPE given in eq. (3).

Various studies done by Joshi and Patel (1997), Joshi *et al.* (2001), Joshi (1997, 1998, 2001), Kumar *et al.* (1998) regarding modeling of strong motion data for the Himalayan earthquakes shows that the GMPE of Abrahamson and Litehiser (1989) is suitable to predict PGA parameters in this region. This relation which is hereby referred in the text as AL89, is given as:

$$\text{Log}_{10}(a(g)) = -0.62 + 0.177M - 0.982 \log_{10}(R + e0.284M) + 0.132F - 0.0008ER \quad (5)$$

In this expression, M is the magnitude of the earthquake represented by an element, R is the distance in km to the closest approach of the zone of energy release and a(g) is the horizontal PGA. The variable E is a dummy variable and is 1 for interplate events and 0 for intra plate events. The dummy variable F is 1 for reverse or reverses oblique events and 0 otherwise. For the Himalayan region, the local condition favour using values E = 1 and F = 1 and hence these are used for calculating the value of PGA by this expression for Himalayan earthquakes. Data set used to develop this GMPE is shown in Figure 4. Figure 4 is a plot of the earthquake magnitude with distance of the 585 recordings. The database includes accelerations from distance ranging between 0.08 km to 400 km and surface wave magnitudes between 5.0 to 8.1.

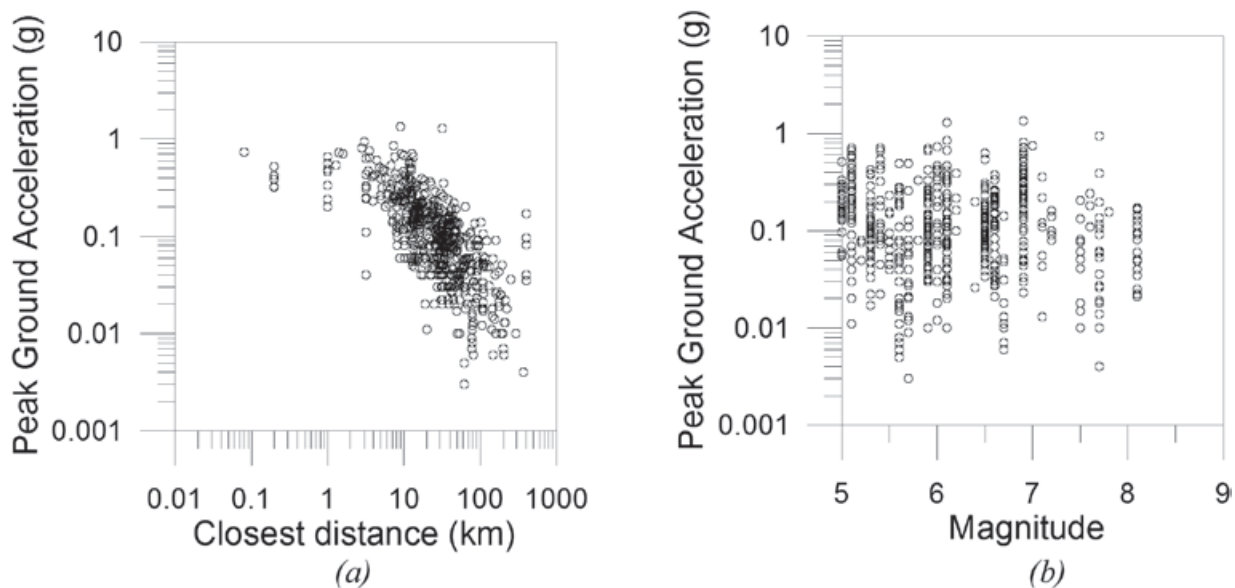


Figure 4. Distribution of PGA with respect to (a) closest distance and (b) magnitude for the data used in the GMPE given by AL89.

The GMPE developed by Joyner and Boore (1981) has been used for preparing the seismic hazard map of India and adjoining region by Bhatia *et al.* (1999) under Global Seismic Hazard Assessment Program (GSHAP). The GMPE given by Joyner and Boore (1981) is hereby referred as JB81 in the text and is given as:

$$\text{Loga}(g) = -1.02 + 0.249M - \log r - 0.00255r \tag{6}$$

Where $r = (d_2 + h_2)^{1/2}$, $h = 7.3$

In this expression, 'r' is the hypocentral distance, 'M' is the magnitude of earthquake and a(g) is PGA in g. This relation is restricted to the data of Western North American shallow earthquakes with depth less than 20 km and magnitude more than 5.0 and includes 183 records. The distribution of hypocentral distance and magnitude with respect to PGA is shown in Figure 5.

Testing normality and model adequacies on GMPE:

A very simple method for checking the normality assumption in GMPE is to construct a cumulative probability plot of the residuals. First step in this process is calculation of random residuals. The random residual is defined as difference of logarithm of actual and predicted values. The

random residuals are arranged in an increasing order and are plotted against cumulative probability in order to make cumulative probability plot. The ideal normal probability plot of random residual follows a straight line. Substantial departures from a straight line indicate that the distribution is not normal. A departure from normality is potentially serious as the *t* or *F* statistics and confidence and prediction interval depends on normality assumption (Montgomery *et al.*, 2001). The model inadequacies in the GMPE are checked by the plot of random residual versus actual value. In the present work model adequacies present in various GMPE are checked by plotting random residuals versus observed PGA values with random residual on vertical axis. It is seen that as long as the plot of random residuals versus observed values follows horizontal band there are no model inadequacies. Strong deviations of random residuals from this band and strange patterns often resulted due to the model inadequacies (Montgomery *et al.*, 2003). The GMPE given by AL89 has been tested for normality and model inadequacies in the present work. The observed and predicted value of PGA is shown in Figure 6(a). The check of normality and model inadequacies is shown in Figure 6(b) and 6(c), respectively. The relation between predicted value of the PGA used in the dataset and the actual value obtained from this relation is shown in Figure 6(a). The linear trends of plot in Figure 6(a) denote that GMPE is capable of predicting the data which has been used for its generation.

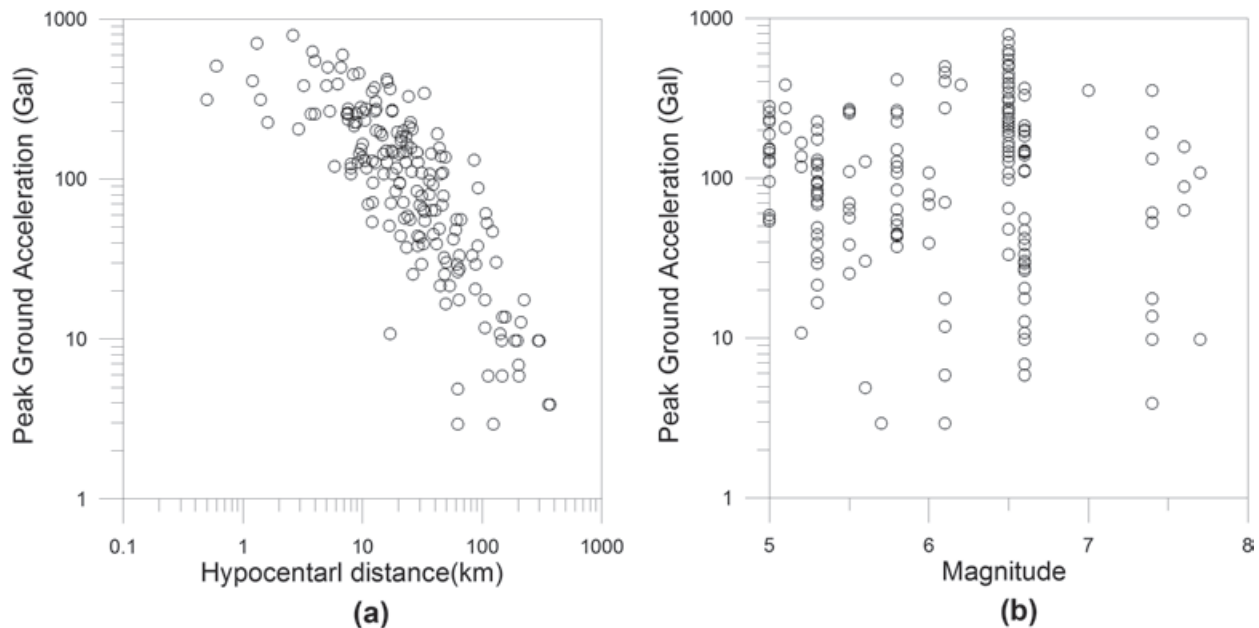


Figure 5. Distribution of PGA with respect to (a) closest distance and (b) Magnitude for the data used in the GMPE given by JB81.

The plot of random residual versus cumulative probability in Figure 6(b) shows presence of weak tail in the cumulative probability plot. The horizontal band of residual in all range of actual data defend that the model is adequate to predict PGA values. The GMPE given by JB81 is tested in the present work. First look between estimated and observed parameters in Figure 7(a) shows a linear trend which gives an impression that the relation can predict PGA parameter; however a closer look on the plot of cumulative probability function versus random residual in Figure 7(b) shows presence of tail in one end of this relation. Funnel pattern in the plot of random residual versus predicted parameter in Figure 7(c) shows that variance increases as Y decreases and this can be attributed from less number of data point in high magnitude range.

The GMPE from database of network installed in the Himalayan region is given by eqs. (3) and (4). In the present work the data set of 130 accelerograms used in preparing this GMPE is used to check the assumption of normality and model inadequacies. Figure 8 and Figure 9 show that GMPE given in eq. (3) and eq. (4) respectively, predict values which are comparable with the observed data. The cumulative probability plot of random variable

also falls in a straight line indicating it to be following normality assumption. However some weak tails are also evident at the extreme ends.

The test on normality and model inadequacies on various GMPE shows that GMPE behave almost similar to its dataset which was initially used for its prediction. In order to check the effect of normality for predicting data set other than that used for developing the respective GMPE a test is performed to predict data set of AL89 using GMPE given by JB81 and that of JB81 using GMPE given by AL89. Clear deviation from normality is observed in this test which is shown in Figure 10. These cumulative probability plots show that the mean is a negative value which means there is a problem of underestimation. The problem of underestimation can also be due to the difference in the variables used in two GMPE models. It is seen that the deviation from cumulative probability plot on predicting the data of AL89 by JB81 is less because of the large amount of data used by AL89 as compared to JB81.

The effect on the assumption of normality and model inadequacies in the GMPE used for predicting regional Himalayan data is checked in this paper. In this test GMPE of AL89, JB81 are

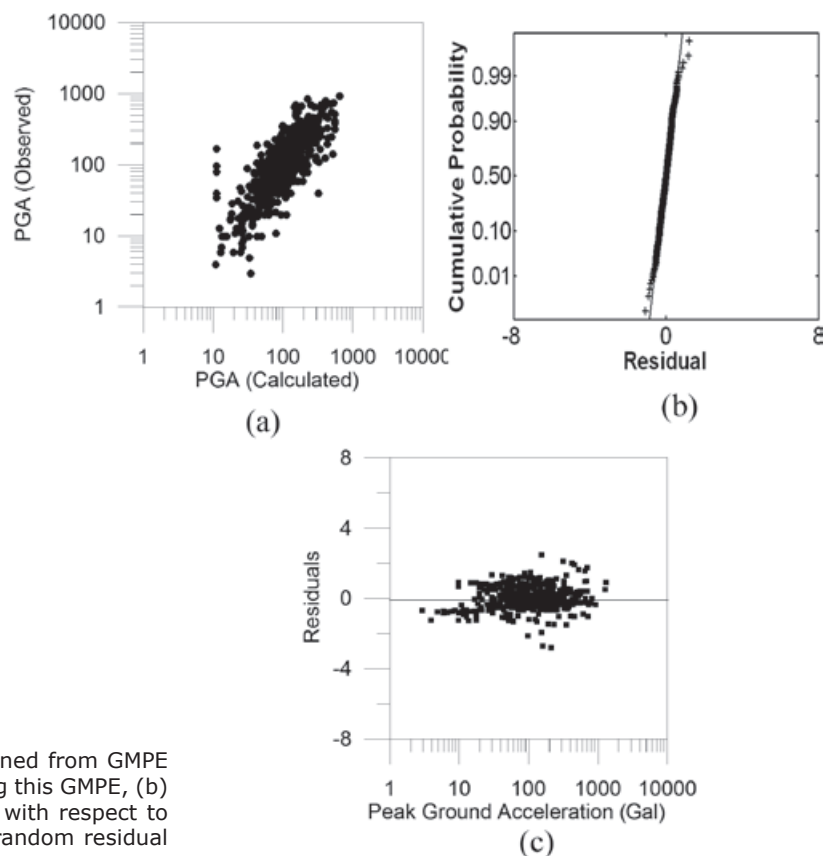


Figure 6. (a) comparison of PGA obtained from GMPE of AL89 with the data used in developing this GMPE, (b) its cumulative probability function plot with respect to random residual of estimation, (c) its random residual plot with respect to PGA parameter.

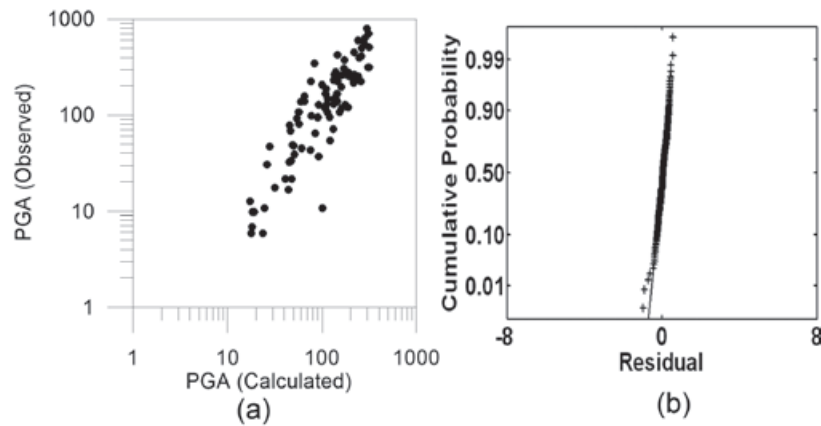


Figure 7. (a) comparison of PGA obtained from regression relation of JB81 with the data used in developing this GMPE, (b) its cumulative probability function plot with respect to random residual of estimation, (c) its random residual plot with respect to PGA parameter.

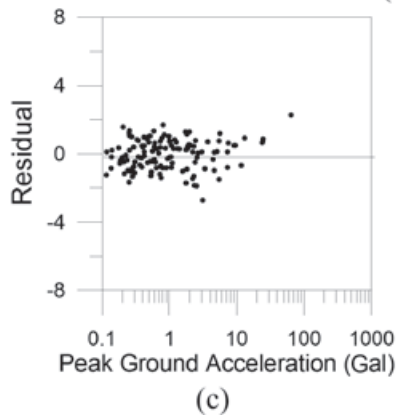
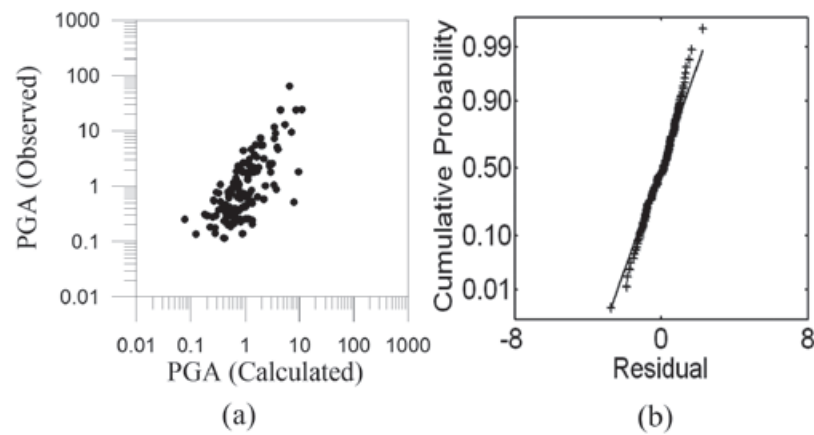
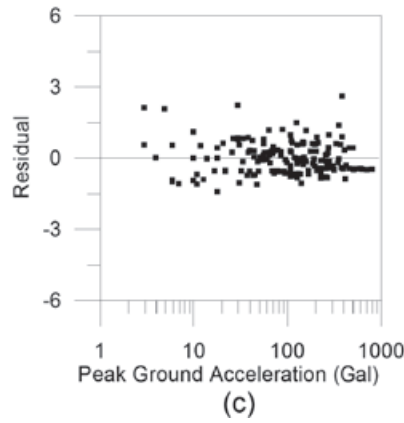
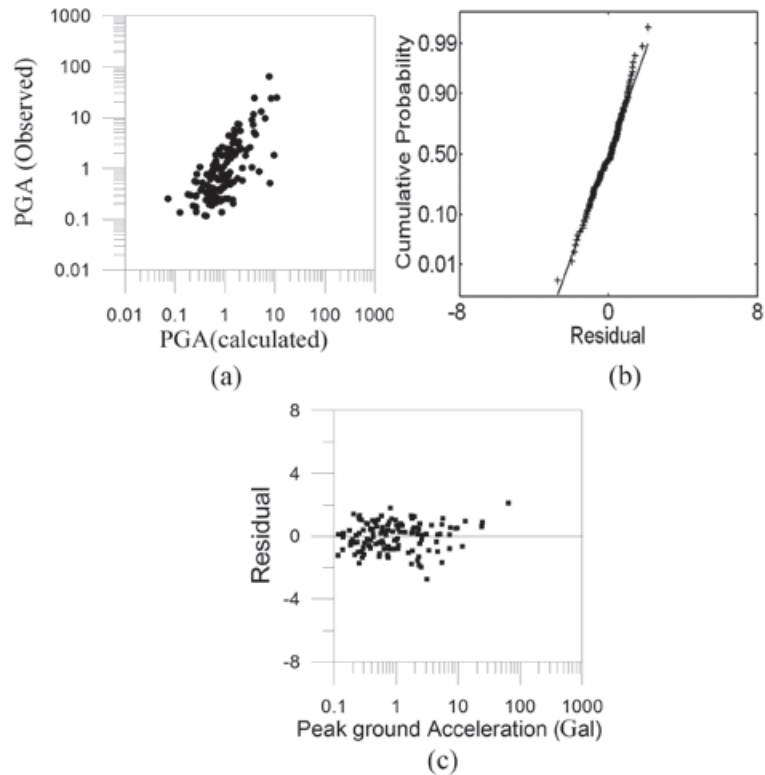


Figure 8. (a) Comparison of PGA obtained from regression model of Joshi *et al.* (2011) with the data used in developing this GMPE, (b) its cumulative probability function plot with respect to random residual of estimation, (c) its random residual plot with respect to PGA parameter.

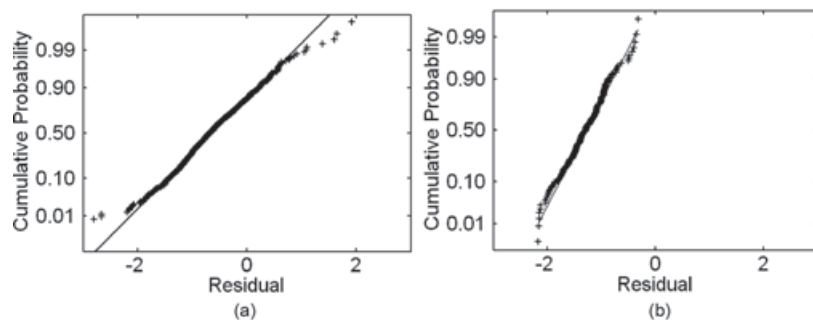
Figure 9. (a) Comparison of PGA obtained from regression model of Joshi *et al.* (2011) with the data used in developing this GMPE using epicentral distance as one of the distance dependent parameter, (b) its cumulative probability function plot with respect to residual of estimation, (c) its residual plot with respect to PGA parameter.



included because of its frequent use in strong motion modeling of Himalayan earthquakes (Joshi, 2006; Kumar *et al.*, 1998) and in seismic hazard estimation of the region (Bhatia *et al.*, 1999). This test also includes other recent GMPE given by Boore *et al.* (1997) and Boore and Atkinson (2008). The GMPE given by Boore and Atkinson (2008) and Boore *et al.* (1997) is now hereby referred to in the text as BA08 and BO97, respectively. The test checks the distribution of random residual with respect to PGA and deviation of its random residuals from normality and is shown in Figure 11. It is seen that the ground motion relations by AL89, BA08 and JB81 overestimate the value of PGA when

applied for predicting Himalaya data, thus clearly emphasizing the need to develop a new GMPE for the region. Although BO97 gives comparable match in terms of predicted parameter, strict deviation from normality is clearly seen in the GMPE when used for predicting Himalayan data. It is seen from this test that when these relations are used for predicting values of PGA for Kumaon Himalaya, a fat tail or heavy tail is clearly seen in the normality of random residual which clearly indicates deviation of GMPE from normality. This type of deviation from normality is expected to affect PSHA technique where we use 10% of probability of exceedence of PGA in 50 years as a major parameter for seismic hazard zonation.

Figure 10. Cumulative probability plots of random residual produced by using (a) GMPE defined by JB81 for predicting data used in AL89 (b) GMPE defined by AL89 for predicting data used in JB81.



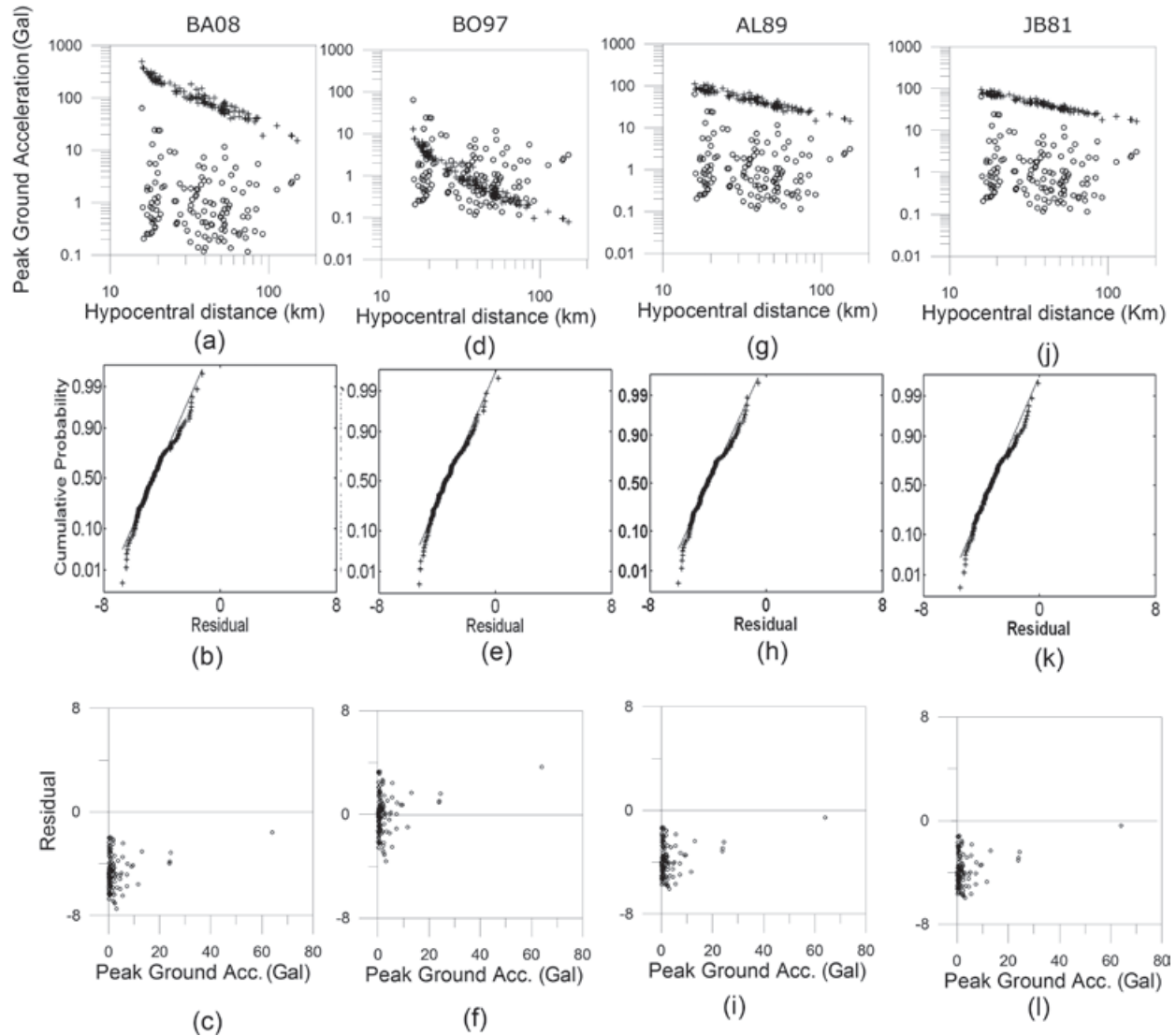


Figure 11. (a) Comparison of PGA obtained from GMPE defined by BA08 with the data of Kumaon Himalaya (2011), (b) its cumulative probability function plot with respect to random residual of estimation, (c) its random residual plot with respect to PGA parameter, (d) Comparison of PGA obtained from GMPE of BO97 with the data of Kumaon Himalaya (2011), (e) its cumulative probability function plot with respect to random residual of estimation, (f) its random residual plot with respect to PGA parameter. (g) Comparison of PGA obtained from GMPE of AL89 with the data of Kumaon Himalaya (2011), (h) its cumulative probability function plot with respect to random residual of estimation, (i) its random residual plot with respect to PGA parameter. (j) Comparison of PGA obtained from GMPE of JB81 with the data of Kumaon Himalaya (2011), (k) its cumulative probability function plot with respect to random residual of estimation, (l) its random residual plot with respect to PGA parameter.

Estimation of seismic hazard map using different GMPE:

It is seen that appropriate choice of GMPE influence the value of predicted parameter. In an attempt to check how GMPE can influence seismic hazard map of the region, the seismic hazard map of Uttarakhand Himalaya is prepared using different GMPE. Joshi and Patel (1997) have formulated a method of seismic zonation which is based on the deterministic modeling of finite ruptures along identified probable fault in an area

using a semi empirical approach. This method of zonation has been applied for the Doon valley (Joshi and Patel, 1997); Assam valley (Joshi *et al.*, 2007) and the Uttarakhand Himalaya (Joshi and Mohan, 2010). The technique of zonation is dependent on the semi empirical simulation technique which in turn is dependent on the GMPE applicable for the region under study. In the preparation of seismic zonation maps for the Uttarakhand Himalaya by Joshi and Mohan (2010), Joshi and Patel (1997) the GMPE relation given as AL89 has been used. Although

AL89 is based on worldwide data it is seen in the present work that this relation suffers from problem of overestimation and deviation from normality when used for predicting Himalayan earthquakes. In the present work seismic hazard for PGA of 100 Gals for 10% probability of exceedence is prepared using modified seismic zonation technique given by Joshi and Patel (1997). Various steps in this technique are as follows:

(i) The first step is the identification of active lineaments in the region. The length of a possible rupture along these lineaments is measured from the same map. The length and width of possible ruptures along these lineaments are calculated using the empirical relationship of Wells and Coppersmith (1994) and Kanamori and Anderson (1975), respectively.

(ii) The entire region is divided into a grid consisting of several observation points at which PGA is computed from the simulated acceleration record using semi empirical technique.

(iii) At the each observation point PGA's are computed by modeling one by one, the rupture along each selected lineament using semi the empirical modeling technique given by Midorikawa (1993). This technique is based on GMPE. For 'm' number of lineaments, 'm' values of peak ground accelerations (i.e., $P_{a1}, P_{a2}, \dots, P_{am}$) are obtained at that observation point. In this process the PGA's are also obtained for various possibilities of nucleation points. For a rupture divided into subfaults of size $n \times n$ there are $n \times n$ possibilities of nucleation points. Therefore the process of simulation generates a dataset of PGA's which consists of all possibilities of ruptures. The database includes contributions from ruptures within 100 km radius from the observation point. The probability of exceedence of PGA of 100 Gal is computed using the obtained database of PGA's values from several model at the observation site.

(v) Since we are dealing with a small area therefore a similar frequency-magnitude relation is expected in the region. The frequency magnitude relation for this region is calculated on the basis of available data from USGS and is given as:

$$\text{Log } N = 5.7 - .71 M$$

Where, M is the magnitude of earthquake and N is number of earthquake equal or more than M.

(v) The process is repeated for all observation points and the probability of exceedence of PGA at each point is computed. Contours of the expected acceleration have been used for defining various

zones. These zones are used to get the value of PGA in a region due to an expected earthquake. This parameter is finally used in the preparation of a seismic hazard zonation map.

The tectonic map of the Uttarakhand Himalaya showing various ruptures along lineaments that are modeled for seismic zonation is shown in Figure 12. These lineaments are identified from the tectonic and geological map of the region given by GSI (2000). The region of Uttarakhand Himalaya consists of Garhwal and Kumaon Himalaya. Although these two regions have similar tectonics and geology, different attenuation models have been obtained for these regions by Joshi *et al.* (2011). The Garhwal Himalaya has been selected as an area between latitude 29° to 33° and longitude 78° to 80°, which covers 60% area of the Uttarakhand Himalaya. The Kumaon region has been selected as an area between latitude 29° to 33° and longitude 80° to 81° which covers 40% of total area of Uttarakhand Himalaya. In this work we have used the GMPE given by eqs. (3) and (4) for modeling lineaments in the Kumaon region while for Garhwal region we have followed the GMPE given by Joshi *et al.* (2011). The software used for preparing seismic hazard in this paper is a modification of MICRZ given by Joshi and Patel (1997). The GMPE given by eqs. (3) and (4) are both based on regional data and differ only in term of distance parameter. The seismic hazard map prepared using eqs. (3) and (4) is shown in Figure 13(a) and (b) respectively and it shows that as long as a GMPE prepared from regional database is used in seismic hazard zonation there is no drastic difference in the obtained seismic hazards of the region using similar technique. However strong difference in terms of shape of zones is observed when the AL89 is used as GMPE for seismic hazard zonation. Since AL89 clearly shows overestimation of PGA values the zones of 10% probability of exceedence of PGA of value 100 Gal shown in the seismic zoning map in Figure 14 has also increased drastically. This test demonstrates importance of proper choice of GMPE for seismic hazard zonation in any region.

Conclusions

The main conclusion drawn from the study is that when using a GMPE in any region we must test it against the data that are present in that region which can help us decide the applicability of GMPE. The paper discusses the applicability of GMPE for predicting values for which it is made. Cumulative probability plots and random residual plots are used to check the presence of fat tail and model adequacies in the GMPE given by BO97, BA08, AL89 and JB81. It is seen that as long as the data set is similar as the one used for generating

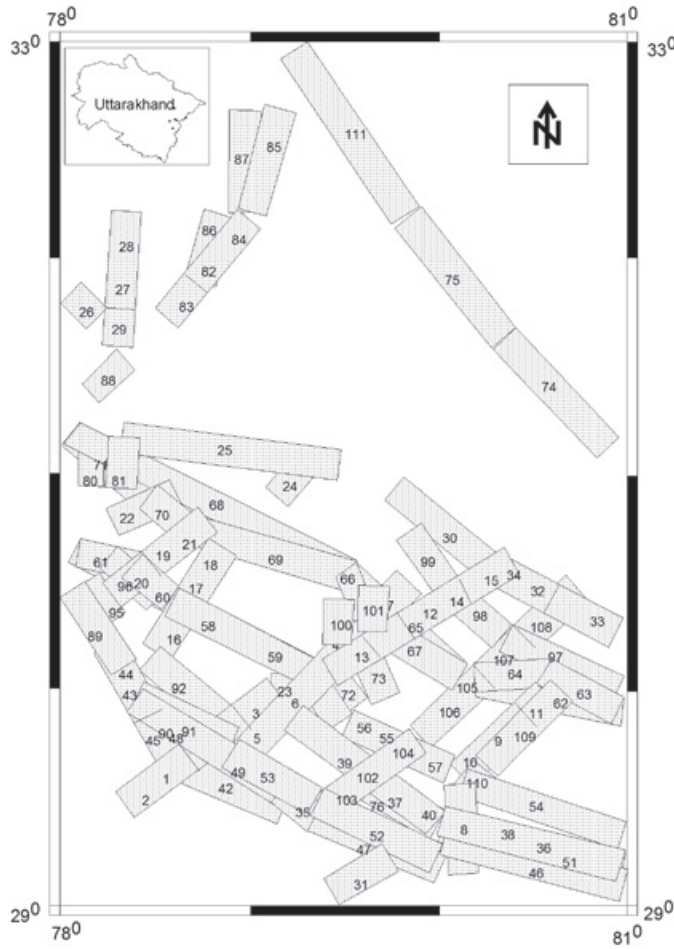


Figure 12. Location of rupture modeled for Uttarakhand Himalaya for preparation of seismic zonation map. The ruptures were taken from the seismotectonic map of Uttarakhand given by GSI (2000).

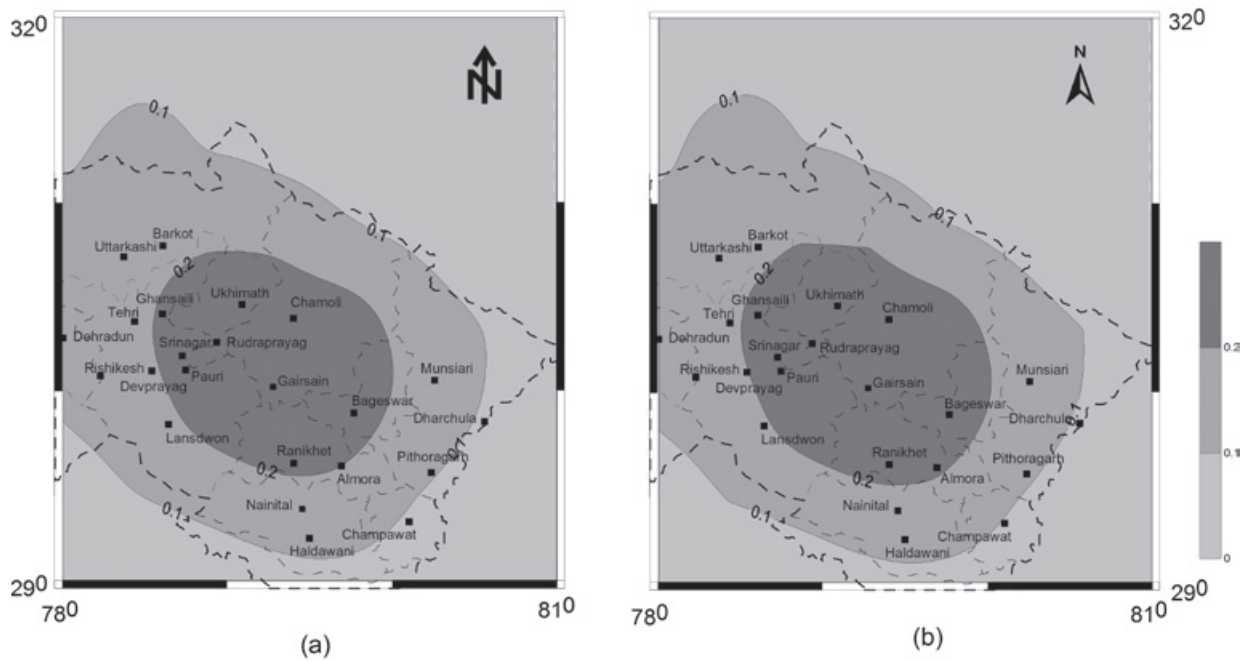


Figure 13. Seismic hazard map of Uttarakhand Himalaya showing 10% probability of exceedence of PGA of 100 Gals using GMPE dependent on (a) Hypocentral and (b) Epicentral distance, respectively. The region covering contour of 0.1 value shows the region having probability of exceedence of PGA of 100 Gals.

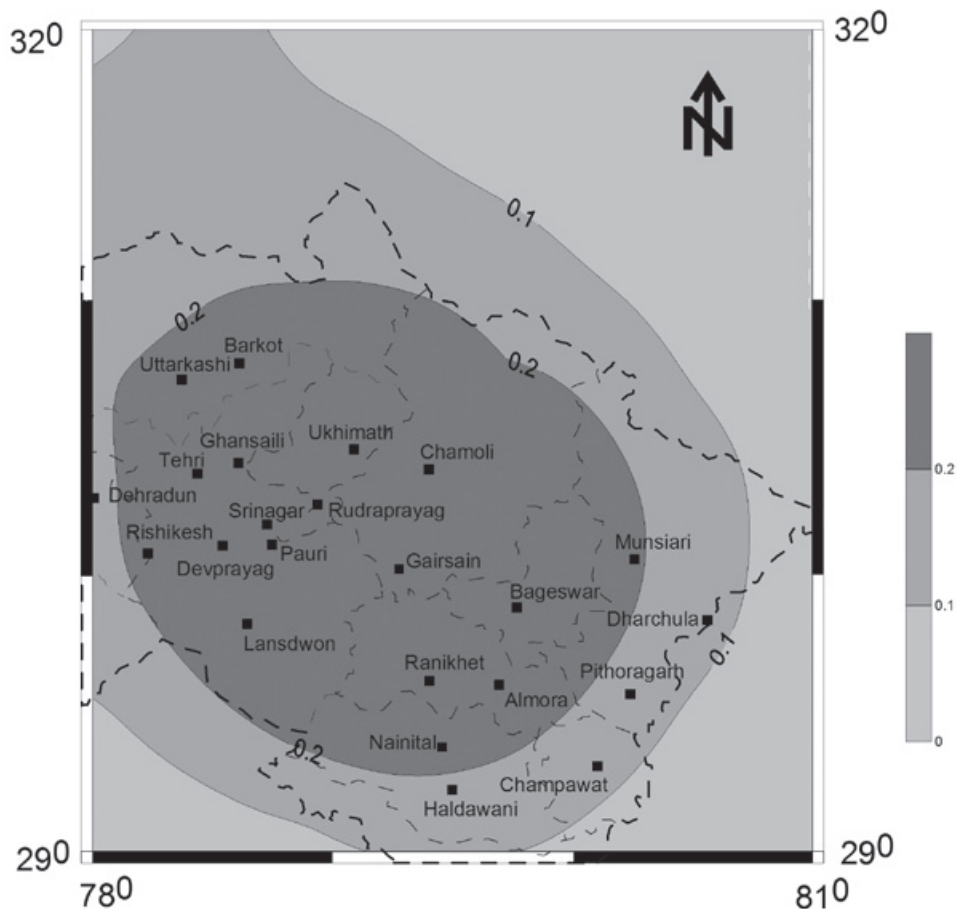


Figure 14. Seismic hazard map of Uttarakhand Himalaya showing 10% probability of exceedence of PGA of 100 Gals using GMPE given by AL89. The region covering contour of 0.1 values shows the region having probability of exceedence of PGA of 100 Gals.

GMPE the normality and model adequacies are satisfied. When the data is different than that used for generation of the GMPE, deviation is observed in the cumulative probability plot. In order to check utility of the worldwide GMPE for predicting dataset other than that used for preparing the GMPE, the dataset of Himalayan earthquakes recorded on strong motion network has been predicting using various GMPE's. It is seen that these GMPE's show the presence of fat tails together with large model adequacies when are used for predicting Himalayan data. On the other side the regression model developed using Himalayan data obeys normality and does not reflect any model inadequacies. In order to check the dependency of selected GMPE on obtained seismic zonation map, the region of Uttarakhand Himalaya is selected in the present work. The seismic Zonation map is prepared for this region using the technique given by Joshi

and Patel (1997). Different zonation map are prepared for different GMPE's and it is seen that similar seismic zonation maps are obtained when different GMPE based on similar regional data are used and strong difference is obtained when GMPE based on other data is used in seismic zonation. The main conclusion that can be drawn from the study is that when using a GMPE in any region we must test it against the deviation from normality and model adequacies before using it for seismic zonation and other uses.

Acknowledgements

Authors sincerely acknowledge the grant received from Indo-Mexican project grant no. DST/INT/MEX/PRO-05/2007 for this work. The data used in this project is outcome of project grant No. MoES /P.O.(Seismo)/ 1(42)/2009.

Bibliography

- Abrahamson N.A., Litehiser J.J., 1989, Attenuation of vertical peak acceleration, *Bull. Seism. Soc. Am.*, 79, p.549-580.
- Abrahamson N., Atkinson G., Boore D., Bozognia Y., Campbell K., Chiou B., Idriss I. M., Silva W., Youngs R., 2008, Comparisons of the NGA ground-motion relations, *Earthquake Spectra* 24, p. 45-66.
- Bhatia S.C., Ravi Kumar M., Gupta H.K, 1999, A probabilistic hazard map of India and adjoining regions. *Annali di geofisica*, 42:1153-1164.
- Bommer J.J., Abrahamson N.A., 2006, Why Do Modern Probabilistic Seismic-Hazard Analyses Often Lead to Increased Hazard Estimates? *Bull. Seism. Soc. Am.*, 96, p.1967-1977.
- Boore D.M., Atkinson G.M., 2008, Ground motion prediction equations for the average horizontail component of PGA, PGV and 5% damped PSA at spectral periods between 0.01s and 10.0s, *Earthquake Spectra*, 24, 1, pp. 99-138.
- Boore D.M., Bommer J.J., 2005, Processing of strong motion accelerograms: needs, options and consequences, *Soil Dynamics and Earthquake Engineering*, 25, pp. 93-115.
- Boore D.M., William B., Joyner, Fumal T.E., 1997, Equations for Estimating Horizontal Response Spectra and Peak Acceleration from Western North American Earthquakes: A Summary of recent Work, *Seismological Research Letters*, 68, 1, p. 128-153.
- Campbell K.W., 1981, Near source attenuation of peak horizontal acceleration, *Bull. Seism. Soc. Am.*, 71, 6, 2,039-2,070.
- Donovan N.C., 1973, A statistical evolution of strong motion data including the February 9, 1971 san Fernando earthquake 5th world conf. earthquake Eng.
- Douglas J., 2011, Investigating possible regional dependence in strong motions, in *Earthquake data in Engineering Seismology*, S. Skkar, P. Gulkan and T. Van Eck (eds.). Springer Ltd. Pp. 29-38.
- Esteva L., 1970, Seismic risk and seismic design decisions, in *Seismic Design for Nuclear Power Plants*, R. J. Hansen (Editor), MIT Press, Cambridge, Massachusetts, 142-182.
- G.S.I., 2000, *Seismotectonic atlas of India and its environs*, Geol Soc India 43, eds. Dasgupta S., Pande P., Ganguly D, Iqbal Z., Sanyal E., Venkatraman N.V., Dasgupta S., Sural B., Harendranath L., Mazumdar K., Sanyal S., Roy A., Das L.K., Mishra P.S. and Gupta.
- Joshi A., 1997, Modelling of peak ground acceleration for Uttarkashi earthquake of 20th October, 1991, *Bull. Ind. Soc. Earthquake Tech.* 34, 75-96.
- Joshi A., 1998, Study of the Uttarkashi earthquake in terms of rupture model and isoseismals, *J. Geophys.* 19, 133-140.
- Joshi A., 2001, Strong motion envelope modelling of the source of the Chamoli earthquake of March 28, 1999 in the Garhwal Himalaya, India, *J. Seismol.*, 5, pp. 499-518.
- Joshi A., 2006, Use of acceleration spectra for determining frequency dependent attenuation coefficient and source parameters, *Bull. Seism. Soc. Am.*, 96, 2165- 2180.
- Joshi A., Patel R.C., 1997, Modeling of active lineaments for predicting possible earthquake scenario around Dehradun, Garhwal Himalaya, India, *Tectonophysics* 283, 289-310.
- Joshi A., Singh S., Kavita G., 2001, The simulation of ground motions using envelope summations, *P Pure and applied Geophysics*, 158, pp. 877-901.
- Joshi A., Mohan K., Patel R.C., 2007, A deterministic approach for preparation of seismic hazard maps in North East India. *Nat Hazards* 43, 129-146.
- Joshi A., Mohan K., 2010, Expected peak ground acceleration in Uttarakhand Himalaya, India region from a deterministic hazard model. *Natural Hazards* 52, 299-317.
- Joshi A., Ashvini Kumar, Sinvhal A., 2011, Attenuation relation for the Kumaon and Garhwal Himalaya, Uttarakhand, India, *Proceeding of International symposium on The 2001 Bhuj earthquake and advances in earthquake sciences - AES 2011*, ISR, Gandhinagar, Gujart, India, January 22-24.
- Joyner W.B., Boore D.M., 1981, Peak horizontal acceleration and velocity from strong-motion records including records from the 1979 Imperial Valley, California, earthquake, *Bull. Seism. Soc. Am.* 71, 6, 2,011-2,038.
- Kanamori H., 1977, The energy release in great earthquakes, *J. Geophys.*, Res. 82, 2,981-298.

- Kanamori H., Anderson D.L., 1975, Theoretical basis of some empirical relation in seismology, *Bull. Seismol. Soc. Am.*, 65, pp. 1,073-1,095.
- Kumar D., Teotia S.S., Khattri K.N., Rai S.S., 1998, Modeling of accelerograms of two Himalayan earthquakes using a novel semi-empirical method and estimation of accelerograms for a hypothetical great earthquake in the Himalaya.
- Lee W.K.H., Lahr J.C., 1972, HYPO71: A computer program for determination of hypocenter, magnitude, and first motion pattern of local earthquakes", Open File Report, U.S. Geological Survey, 100pp.
- McGuire R.K., 1976, FORTRAN computer program for seismic risk analysis, U.S. Geol. Surv. Open-File Rept, 76-67.
- McGuire R.K., 1977, Seismic design spectra and mapping procedures using hazard analysis based directly on oscillator response, *Earthquake Engineering and Structural Dynamics*, 5, 211-234.
- McGuire R.K., 1978, FRISK-Computer program for seismic risk analysis using faults as earthquake sources United States Geological Survey-open file report, 78-110.
- Montgomery D.C., Peck E.A., Vining G.G., 2003, Introduction to linear regression analysis, John Wiley and Sons (ASIA) Ptv Ltd, Clementi Loop, Singapore.
- Power M., Chiou B., Abrahamson N., Bozorgnia Y., Shantz T., Rooblee C., 2008, An overview of the NGA project, *Earthquake Spectra*, 24 p. 3-21.
- Wells D.L., Coppersmith K.J., 1994, New empirical relationships among magnitude, rupture length, rupture width, and surface displacements, *Bull. Seismol. Soc. Am.*, 84, pp. 974-1002.

Hydrostratigraphy of Haftad Gholle Karst, Markazi province, Iran, optimized by Fuzzy Logic

Mostafa Yousefi Rad*

Received: October 05, 2011; accepted: April 10, 2012; published on line: September 28, 2012

Resumen

Este trabajo presenta la litología kárstica de la región de Haftad Gholle en el SE de Arak, Irán empleando el enfoque de lógica borrosa. El área fue dividida en 7 mitades litológicas. El resultado permitió identificar los recursos del agua óptimos en las calizas macizas del Cretácico Inferior.

Palabras clave: Karst, hidroestratigrafía, lógica borrosa, Arak.

Abstract

The objective of this study is to optimize the karstic lithology in the Haftad Gholle area located of South-eastern Arak, NW Iran, using fuzzy logic. The karst of Haftad Gholle area was divided into seven lithologic units; information on effective properties including thickness, RQD (Rock Quality Designation), opening joints, joint distance, porosity, permeability, and bedding were obtained. Using Similarity to Ideal Solution approach, the data were transformed to fuzzy numbers, and the analysis was performed. The results showed that the best karstic water resources correspond to a unit which includes lower massive limestone karstic units (KL1) belonging to the Lower Cretaceous.

Keywords: Karst, Hydrostratigraphy, Fuzzy logic, Arak.

M. Yousefi Rad*
Department of Geology
Faculty of Earth Sciences
Payam Noor University
Tehran, Iran.

*Corresponding author: mostafa.yousefirad@yahoo.com

Introduction

A Hydrostratigraphic unit includes all or part of a petrologic set which is separated from other units by hydrogeologic properties (Maxey, 1964).

Seaber (1988) proposed that porosity and permeability are the most important feature in determining a hydrostratigraphic unit, but Van Wagoner (1988) involves other properties such as usual hydrodynamic coefficients in the aquifers to define the properties of a hydrostratigraphic unit. The study area is located 40 km to the southeast of Arak, city in the Markazi province (Figure 1).

Main water resources in the area include Anjadan springs, with a water discharge of about 20 liters per second, and a deep well drilled into the lower Cretaceous with a water discharge of about 10 liters per second.

This study has been done to survey the hydrostratigraphic units belonging to the karstic water resources of Haftad Gholle to the Southeast of Arak in Markazi Province, Iran. The best karstic water resources were determined by the Similarity to Ideal Solution method.

Methodology

Usual methods were used to determine the lithostratigraphy and biostratigraphic properties. A Lugeon test was first performed in seven boreholes drilled in each lithologic unit to determine the permeability and other relevant hydrostratigraphical properties of the lithologic.

All boreholes were sampled to obtain the degree of effective porosity by estimating the amount of drainable water in the laboratory. As the karstic aquifer is open, the storage coefficient was actually determined by effective porosity and total porosity. Also, its water transfer capability of lithologic units were estimated by assuming full saturation from permeability, and thickness of each lithologic unit. Finally, the type of aquifer per lithologic unit was identified using the available information.

Geology

From the geology viewpoint, the study area is located between two central geologic provinces; Iran and Sanandaj-Sirjan (Emami, 1992). The Tabarteh fault forms the border separating these two geologic provinces zones (Figure 2).

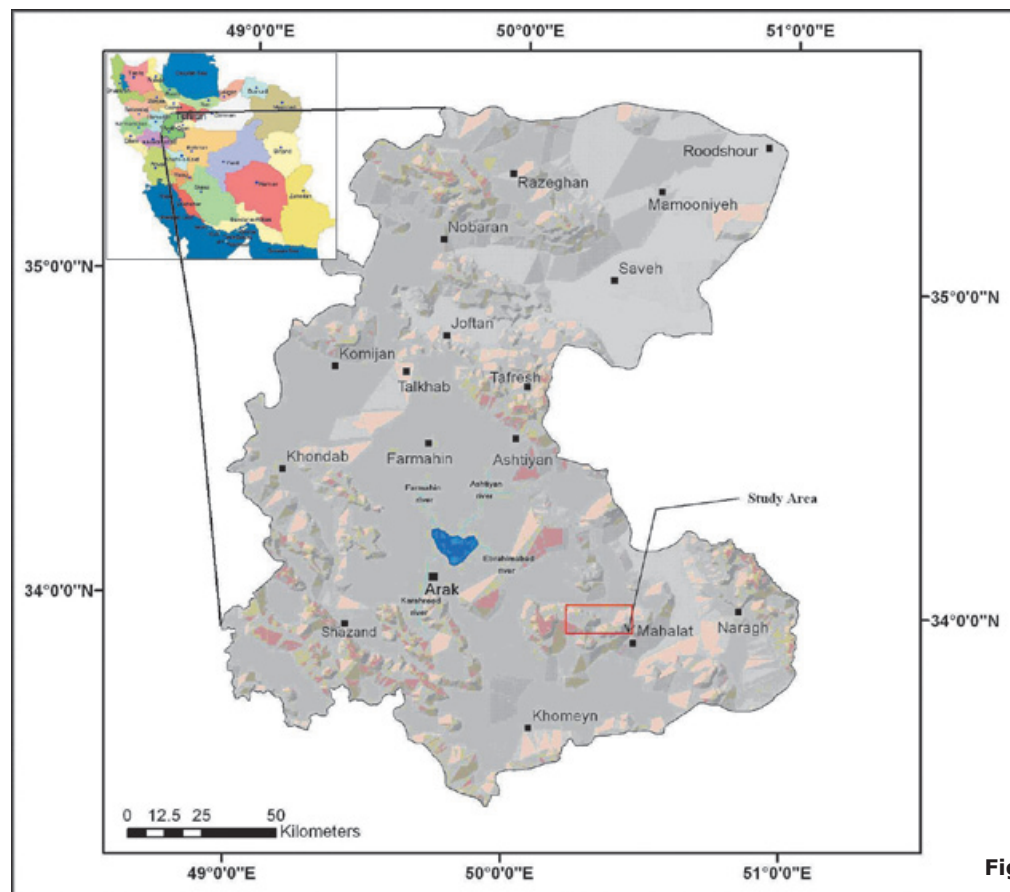
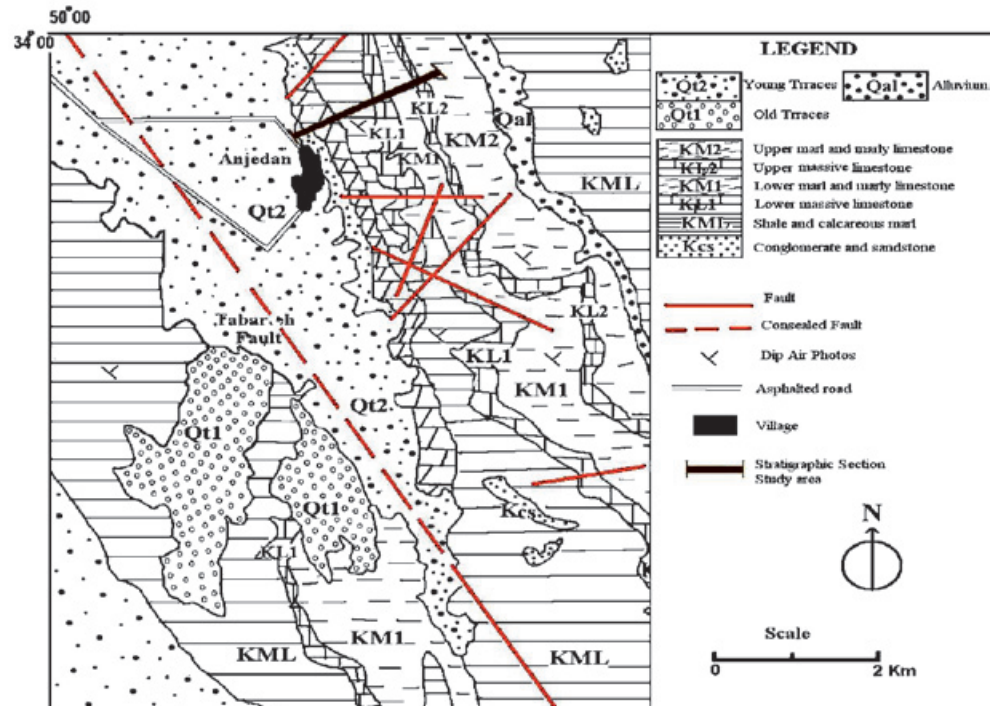


Figure 1. Location of the study area.

Figure 2. Geological map of the study area.



Petrology

A stratigraphic section location in (Figure 2) shows that in the study area, there age of the lower Cretaceous age outcropped and these units are subdivided into conglomerates and sandstones (Kcs); dolomites and limey dolomites (Kd); shales and calcareous marls (KML); lower massive limestones (KL1); lower marls and marly limestones (KM1); upper massive limestones (KL2); and upper marls and marly limestones (KM2) from top to bottom respectively.

The carbonate lithologic units are among the most important lithologic units because of more dissolubility, and they contain the principal underground water reserves in the area. The major stratigraphic units are shown in Figure 3.

Structural Properties

Structural features in southeastern Arak are considered determinant for the formation and development of the karst. Tabarteh fault activity has given rise to several sub-faults in the lithologic units (Figure 2).

This fault has also caused joints and fracture systems in lithologic units. Faulting and fracturing

are also effective in increasing the effective porosity and developing and accelerating the karst process.

This is evident from the tests of permeability and will not be mentioned further.

But there are other structural properties including thickness of layers, surface RQD,

Figure 3. Lithostratigraphic properties of the Cretaceous sequence.

Age	Thickness	Stratigraphic	Sample	Lithology
Cenomanian	400	[Stratigraphic column]	A10	Marl and marly limestone
			A9	Massive limestone
Albian	300	[Stratigraphic column]	A8	Marl and marly limestone
			A7	
			A6	Massive limestone
A5				
Aptian	200	[Stratigraphic column]	A4	Massive limestone
			A3	
Barremian	100	[Stratigraphic column]	A2	Dolomite and dolomitic limestone
			A1	Conglomerate and sandstone

opening joints, joint distance, porosity, permeability, bedding, which have been effective in the formation and development of a karstic aquifer in the area.

The greater the thickness of lithologic units with karstic capability the larger the aquifer (Seaber, 1988). Table 1 summarizes these properties for the lithologic units in the study area.

Hydraulic Properties

The most important purpose of the study is to identify the hydraulic properties of the lithologic units.

This section of the study attempts to identify the hydrostratigraphic unites and determine the role of main lithologic units in forming the karstic aquifer. This provides the best data to classify the hydrostratigraphic units for their contribution in formation of karstic aquifer (Van Wagoner, 1990).

The hydraulic properties in each lithologic units were determined by Lugeon tests and other required tests (Agassi and Afrasiabi, 2004).

Results of these experiments for the lithology of the cretaceous sequence have been presented in Table 1.

According to Table 1, lithologic units KL1 and KL2 are distinguished other units, so that is hydrostratigraphic unit has very good structural and hydraulic properties to form the karstic aquifer in the area.

Finally, we determine the best karstic water resources storage units using the Similarity to Ideal Solution method (TOPSIS).

This method is a popular approach to multiple criteria decision making (MCDM). It has been widely used in the literature. TOPSIS is a technique for order preference by similarity to ideal solution

proposed by Hwang and Yoon(1981), Agrawal *et al.*(1991), Lai, *et al.*(1994), Kim *et al.*(1997), Parkan and Wu,(1997), Zanakis *et al.*(1998), Deng, *et al.*(2000), Jee and Kang(2000), Feng and Wang(2001), Cheng *et al.*(2003), Liao(2003), Olson(2004), Opricovic and Tzeng(2004), Abo-Sinna and Amer(2005),Tzeng, *et al.* (2005).

The Fuzzy Technique for Order Preference by Similarity to Ideal Solution (FTOPSIS) (Triantaphyllou and Lin, 1996) is a fuzzy multi-objective decision technique based on simple geometric concepts: the best alternative exhibits the shortest distance from the Best Ideal Solution (BIS) and the farthest distance from the Worst Ideal Solution (WIS) in a Euclidean sense. Just as the LW method, this approach requires as input data the $m \times n$ decision matrix **DM** and the weights w_j with $j=1, \dots, n$ measuring the criteria importance. Moreover, a fuzzification process associates to each value dm_{ij} of **DM** a fuzzy value d'_{ij} , with $0 \leq d'_{ij} \leq 1$, defining the $m \times n$ fuzzified decision matrix **D'**, depending on the user satisfaction degree with respect to the criteria.

There are seven called alternative hydrostratigraphic units to select the best aquiferous layer, where the hydrostratigraphic units are conglomerate and sandstone (Kcs); dolomite and limey dolomite (Kd); shale and calcareous marl (KML); lower massive limestone (KL1); lower marl and marly limestone (KM1); upper massive limestone (KL2); upper marl and marly limestone (KM1) from lower to upper respectively.

We want to select one of these seven units based on seven criteria (thickness, surface RQD, opening joints, joints distance, porosity, permeability, and bedding). The thickness, porosity, permeability, and bedding criteria have positive aspects and the surface RQD, opening joints and joints distance criteria have negative aspects, where the hierarchical structure for the decision is shown in Figure 4.

Table 1. Structural and Hydraulic properties of lithologic units in the study area.

KM2	KL2	KM1	KL1	KML	Kd	KCS	Lithologic unit Properties
55	25	115	105	36	45	123	Thickness
69.3	42.6	59.3	41.5	68.2	48.2	61.2	RQD
2	6	3	7	3	4	4	Opening Joint
15	40	20	31	20	40	15	Joint distance
18.7	32.1	19.1	37.6	15.7	14.8	13.1	porosity
3.06	11.49	2.59	10.31	6.72	3.7	4900	permeability
7	105	20	105	20	65	65	Bedding

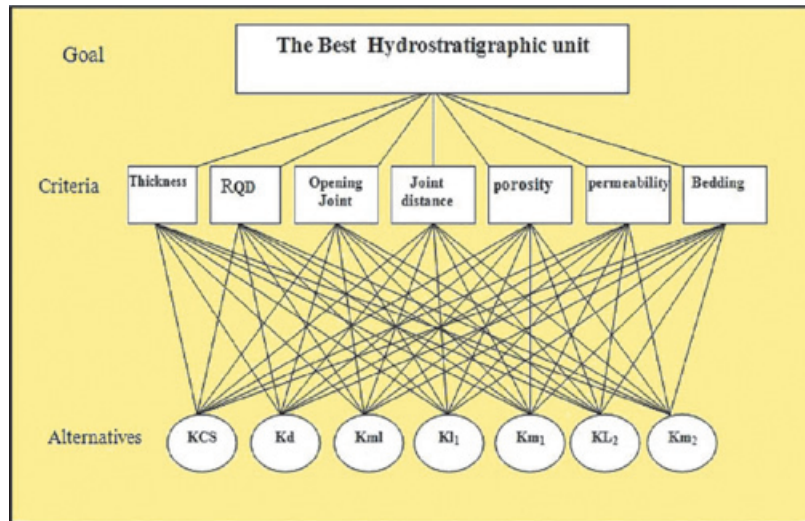


Figure 4. The Hierarchical structure for selecting the best aquiferous layer.

Step 1: Decision matrix and weights vector of criteria

The alternatives have been evaluated by different criteria and the results as decision matrix is presented as Table 2.

Table 2. The results of evaluated criteria (Decision Matrix).

							Criteria
Bedding	Permeability	Porosity	Joint distance	Opening Joint	RQD	Thickness	Alternative
Thick layer	With high permeability	Very good	high	Very high	Average	high	Kcs
Thick layer	With high permeability	Average	Average	Very high	Weak	Average	Kd
Middle layer	With very high permeability	good	high	Very high	Average	Average	KML
Mass	With very high permeability	Very good	Average	high	Weak	Very high	KL1
Middle layer	With high permeability	good	high	Very high	Average	high	KM1
Mass	With very high permeability	Very good	Average	high	Weak	Average	KL2
Thin layer	With high permeability	good	high	Very high	Average	high	KM2

The weight vector of criteria is shown in Table 3.

Table 3. The weight vector of criteria.

Bedding	Permeability	Porosity	Joint distance	Opening Joint	RQD	Thickness	Criteria
Somewhat less important	Very important	Important	Indifferent	Somewhat important	Important	Somewhat less important	Weight

Tables 4 to 10 are used to form the fuzzy decision matrix and weight vector.

Table 4. The classification of lithologic units based on bedding.

Linguistic Variable	Bedding		Corresponding Fuzzy Number
	Qualitative	Qualitative	
Very important	>100 cm	Mass	(9,10,10)
Important	30-100	Thick layer	(7,9,10)
Somewhat important	10-30	Middle layer	(5,7,9)
Indifferent	3-10	Thin layer	(3,5,7)
Somewhat less important	1-3	Very thin layer	(1,3,5)
Low importance	0.3-1	Laminate	(0,1,3)
Very low importance	<0.3	Very Laminate	(0,0,1)

Table 5. The classification of lithologic units based on permeability.

Linguistic Variable	Permeability		Corresponding Fuzzy Number
	Qualitative	Qualitative	
Very low importance	< 0.001	Impermeable	(0,0,1)
Low importance	0.001-0.01	With low permeability	(0,1,3)
Somewhat less important	0.01-0.1	Permeable	(1,3,5)
Indifferent	0.1-1	With average permeability	(3,5,7)
Somewhat important	1-10	With high permeability	(5,7,9)
Important	10-100	With very high permeability	(7,9,10)
Very important	100-1000	With extremely high permeability	(9,10,10)

Table 6. The classification of lithologic units based on porosity.

Linguistic Variable	porosity %t	Corresponding Fuzzy Number
Very good	20-25	(9,10,10)
Good	15-20	(5,7,9)
Average	10-15	(3,5,7)
Weak	5-10	(1,3,5)
Very weak	0-5	(0,1,3)

Table 7. The classification of lithologic units based on thickness.

Linguistic Variable	Thickness	Corresponding Fuzzy Number
Very high	100 m More than	(9,10,10)
High	30-100 cm	(5,7,9)
Average	10 -30 cm	(3,5,7)
Low	3- 10 cm	(1,3,5)
Very low	Less than 3 cm	(0,0,1)

Table 8. The classification of lithologic units based on opening joints.

Linguistic Variable	Opening Joint	Corresponding Fuzzy Number
Very low	25	(9,10,10)
Low	20	(5,7,9)
Average	12	(3,5,7)
High	6	(1,3,5)
Very high	0	(0,1,3)

Table 9. The classification of lithologic units based on surface RQD.

Linguistic Variable	RQD	Corresponding Fuzzy Number
Very important	91-100	(9,10,10)
Important	76-90	(5,7,9)
Average	51-75	(3,5,7)
Weak	26-50	(1,3,5)
Very weak	0-25	(0,1,3)

Table 10. The classification of lithologic units based on joint distance.

Linguistic Variable	Joint distance	Corresponding Fuzzy Number
Very low	>3	(8,10,10)
Low	1-3	(6,7,8)
Average	0.3-1	(4,5,6)
High	0.5-0.3	(2,3,4)
Very high	0.05	(0,1,2)

Using the above tables, the fuzzy weight vector is obtained as Table 11:

Table 11. Fuzzy weight vector.

Bedding	permeability	porosity	Joint distance	Opening Joint	RQD	Thickness Alternative	Criteria
(7 th Criteria)	(6 th Criteria)	(5 th Criteria)	(4 th Criteria)	(3 th Criteria)	(2 nd Criteria)	(1 st Criteria)	weight
(0.1,0.3,0.5)	(0.9,1,1)	(0.7,0.9,0.1)	(0.3,0.5,0.7)	(0.5,0.7,0.9)	(0.7,0.9,0.1)	(0.1,0.3,0.5)	

Using the above tables, the fuzzy decision matrix is obtained (table 12).

Table 12. The results of fuzzy decision matrix.

Bedding	permeability	porosity	Joint distance	Opening Joint	RQD	Thickness	Criteria
(7 th Criteria)	(6 th Criteria)	(5 th Criteria)	(4 th Criteria)	(3 th Criteria)	(2 nd Criteria)	(1 st Criteria)	Alternative
(7,9,10)	(3,5,7)	(3,5,7)	(2,3,4)	(0,1,3)	(3,5,7)	(5,7,9)	Kcs
(7,9,10)	(5,7,9)	(3,5,7)	(4,5,6)	(0,1,3)	(1,3,5)	(3,5,7)	Kd
(5,7,9)	(5,7,9)	(5,7,9)	(2,3,4)	(0,1,3)	(3,5,7)	(3,5,7)	KML
(9,10,10)	(7,9,10)	(9,10,10)	(4,5,6)	(1,3,5)	(1,3,5)	(9,10,10)	KL1
(5,7,9)	(5,7,9)	(5,7,9)	(2,3,4)	(0,1,3)	(3,5,7)	(5,7,9)	KM1
(9,10,10)	(7,9,10)	(9,10,10)	(4,5,6)	(1,3,5)	(1,3,5)	(3,5,7)	KL2
(3,5,7)	(5,7,9)	(5,7,9)	(2,3,4)	(0,1,3)	(3,5,7)	(5,7,9)	KM2

Step 2: Unscaling the decision matrix

The first, Second, Third, fifth, sixth and seventh criteria have a positive aspect, and the following equation is used to unscaling the decision matrix.

$$\tilde{r}_{ij} = \left(\frac{a_{ij}}{c_j^*}, \frac{b_{ij}}{c_j^*}, \frac{c_{ij}}{c_j^*} \right) \tag{1}$$

Where

$$c_j^* = \max_i c_{ij}$$

$a_{i,j}$ stands for the first component of vector in position column i , and row j , $b_{i,j}$ for the second component of the triade, and so forth.

For example, in the first row and column of the decision matrix, we have:

$$\tilde{r}_{22} = \left(\frac{5}{10}, \frac{7}{10}, \frac{9}{10} \right) = (0.5, 0.7, 0.9)$$

The second, third and fourth criteria have a negative aspect, and following equation is used to unscaling the decision matrix.

$$\tilde{r}_{ij} = \left(\frac{a_j^-}{c_{ij}}, \frac{a_j^-}{b_{ij}}, \frac{a_j^-}{a_{ij}} \right) \tag{2}$$

Where

$$a_j^- = \min_i a_{ij}$$

For example, in the array for second row and fourth column of the decision matrix, we have:

$$\tilde{r}_{24} = \left(\frac{2}{6}, \frac{2}{5}, \frac{2}{4} \right) = (0.33, 0.4, 0.5)$$

Other arrays for the unscaled decision matrix are calculated by the same calculations that the results would be as table 13.

Table 13. The results of the unscaled decision matrix.

Bedding	Permeability	porosity	Joint distance	Opening Joint	RQD	Thickness	Criteria
							Alternative
(0.7,0.9,1)	(0.5,0.7,0.9)	(0.9,1,1)	(0.25,0.333,0.5)	(0.333,1,0)	(0.143,0.2,0.33)	(0.5,0.7,0.9)	Kcs
(0.7,0.9,1)	(0.5,0.7,0.9)	(0.3,0.5,0.7)	(0.166,0.2,0.25)	(0.333,1,0)	(0.2,0.333, 1)	(0.3,0.5,0.7)	Kd
(0.5,0.7,0.9)	(0.5,0.7,0.9)	(0.5,0.7,0.9)	(0.25,0.333,0.5)	(0.333,1,0)	(0.143,0.2,0.33)	(0.3,0.5,0.7)	KML
(0.9,1,1)	(0.7,0.9,1)	(0.9,1,1)	(0.166,0.2,0.25)	(0.2,0.33,1)	(0.2,0.333, 1)	(0.9, 1,1)	KL1
(0.5,0.7,0.9)	(0.5,0.7,0.9)	(0.5,0.7,0.9)	(0.25,0.333,0.5)	(0.333,1,0)	(0.143,0.2,0.33)	(0.5,0.7,0.9)	KM1
(0.9,1,1)	(0.7,0.9,1)	(0.9,1,1)	(0.166,0.2,0.25)	(0.2,0.333,1)	(0.2,0.333, 1)	(0.3,0.5,0.7)	KL2
(0.3,0.5,0.7)	(0.5,0.7,0.9)	(0.5,0.7,0.9)	(0.25,0.333,0.5)	(0.333,1,0)	(0.143,0.2,0.33)	(0.5,0.7,0.9)	KM2

Table 14. The results of the weighted unscaled decision matrix.

Bedding	Permeability	porosity	Joint distance	Opening Joint	RQD	Thickness	Criteria
							Alternative
(0.07,0.27,0.5)	(0.27,0.5,0.7)	(0.21,0.45,0.7)	(0.075,0.166,0.35)	(0.166,0.7,0)	(0.1,0.18,0.333)	(0.05,0.21,0.45)	Kcs
(0.07,0.27,0.5)	(0.45,0.7,0.9)	(0.21,0.45,0.7)	(0.05,0.1,0.175)	(0.166,0.7,0)	(0.14,0.30, 1)	(0.03,0.15,0.35)	Kd
(0.5,0.21,0.45)	(0.45,0.7,0.9)	(0.35,0.63,0.9)	(0.075,0.166,0.35)	(0.166,0.7,0)	(0.1,0.18,0.333)	(0.03,0.15,0.35)	KML
(0.09,0.3,0.5)	(0.63,0.9,1)	(0.63,0.9,1)	(0.05,0.1,0.175)	(0.1,0.233,0)	(0.14,0.30, 1)	(0.09,0. 3,0.5)	KL1
(0.5,0.21,0.45)	(0.45,0.7,0.9)	(0.35,0.63,0.9)	(0.075,0.166,0.35)	(0.166,0.7,0)	(0.1,0.18,0.333)	(0.05,0.21,0.45)	KM1
(0.09,0.3,0.5)	(0.63,0.9,1)	(0.63,0.9,1)	(0.05,0.1,0.175)	(0.1,0.233,0)	(0.14,0.30, 1)	(0.03,0.15,0.35)	KL2
(0.03,0.15,0.35)	(0.45,0.7,0.9)	(0.35,0.63,0.9)	(0.075,0.166,0.35)	(0.166,0.7,0)	(0.1,0.18,0.333)	(0.05,0.21,0.45)	KM2

Step 3: Obtain the weighted unscaled decision matrix

The method of calculating a few arrays of the matrix is as follows:

$$\tilde{v}_i = \tilde{r}_{ij} \cdot \tilde{w}_j \quad (3)$$

$$\tilde{V}_{ij} = [\tilde{v}_{ij}]_{m \times n} \quad i = 1, 2, \dots, m, j = 1, 2, \dots, n \quad (4)$$

Where $w_j, j=1, 2, \dots, n$ is the importance degree of each criterion and v_{ij} is Weighted normalized matrix element.

For example for v_{17} (Kcs Thckiness) and v_{23} (KML Permeability):

$$\tilde{v}_{17} = (0.5, 0.7, 0.9)(0.1, 0.3, 0.5) = (0.05, 0.21, 0.45)$$

$$\tilde{v}_{23} = (0.5, 0.7, 0.9)(0.9, 1, 1) = (0.45, 0.7, 0.9)$$

Other arrays for the unscaled decision matrix are calculated by the same calculations that the results would be as Table 14.

Step 4: Calculate the ideal (A*) and anti-ideal (A-) alternatives

The method of calculating a few arrays for the matrix is as follows:

$$\tilde{V}_j^* = \max_i \{ \tilde{V}_{ij} \} \quad i = 1, 2, \dots, m, j = 1, 2, \dots, n \quad (5)$$

$$\tilde{V}_j^- = \min_i \{ \tilde{V}_{ij} \} \quad i = 1, 2, \dots, m, j = 1, 2, \dots, n \quad (6)$$

For example for v_7^* (The maximum amount of Thickness) and \tilde{v}_7^- (The minimum amount of Thickness):

$$v_7^* = \left(\begin{matrix} \max(0.45, 0.35, 0.35, 0.5, 0.45, 0.35, 0.45), (0.45, 0.35, 0.35, 0.5, 0.45, 0.35, 0.45) \\ (0.45, 0.35, 0.35, 0.5, 0.45, 0.35, 0.45) = (0.5, 0.5, 0.5) \end{matrix} \right)$$

$$\tilde{v}_7^- = \left(\begin{matrix} \min(0.05, 0.03, 0.03, 0.09, 0.05, 0.03, 0.05), (0.05, 0.03, 0.03, 0.09, 0.05, 0.03, 0.05) \\ (0.05, 0.03, 0.03, 0.09, 0.05, 0.03, 0.05) = (0.03, 0.03, 0.03) \end{matrix} \right)$$

Similar calculations have been done for other alternatives with results as follows:

$$\begin{aligned} v_2^* &= (1, 1, 1) \\ v_3^* &= (0.9, 0.9, 0.9) \\ v_4^* &= (0.7, 0.7, 0.7) \\ v_5^* &= (1, 1, 1) \\ v_6^* &= (1, 1, 1) \end{aligned}$$

$$\begin{aligned} v_7^* &= (0.5, 0.5, 0.5) \\ \tilde{v}_2^- &= (0.1, 0.1, 0.1) \\ \tilde{v}_3^- &= (0, 0, 0) \\ \tilde{v}_4^- &= (0.01, 0.01, 0.01) \\ \tilde{v}_5^- &= (0.21, 0.21, 0.21) \\ \tilde{v}_6^- &= (0.27, 0.27, 0.27) \\ \tilde{v}_7^- &= (0.03, 0.03, 0.03) \end{aligned}$$

The fuzzy ideal (A*) and anti-ideal (A-) alternatives are defined as follows:

$$A^* = \{ \tilde{v}_1^*, \tilde{v}_2^*, \dots, \tilde{v}_n^* \} \quad (7)$$

$$A^- = \{ \tilde{v}_1^-, \tilde{v}_2^-, \dots, \tilde{v}_n^- \} \quad (8)$$

For example for A* and A- :

$$A^* = [(0.05, 0.05, 0.05), (1, 1, 1), (0.7, 0.7, 0.7), (0.35, 0.35, 0.35), (1, 1, 1), (1, 1, 1), (0.5, 0.5, 0.5)]$$

$$A^- = [(0.03, 0.03, 0.03), (0.1, 0.1, 0.1), (0, 0, 0), (0.05, 0.05, 0.05), (0.21, 0.21, 0.21), (0.27, 0.27, 0.27), (0.03, 0.03, 0.03)]$$

Step 5: Determine the distance of any alternative from the ideal and anti-ideal (S* and S-) alternative and similarity attribute.

The distance of first alternative from the fuzzy ideal alternative of each of the criteria is calculated as follows:

$$S_i^* = \sum_{j=1}^n d(\tilde{v}_{ij}, \tilde{v}_j^*), \quad i = 1, 2, \dots, m \quad (9)$$

Where d , represents the distance measurement between two fuzzy numbers. For example for S*11 - S*17 :

$$S_{17}^* = \sqrt{\frac{1}{3}[(0.05 - 0.5)^2 + (0.21 - 0.5)^2 + (0.45 - 0.5)^2]} = 0.32$$

$$S_{12}^* = 0.45, S_{13}^* = 0.70, S_{14}^* = 0.38, S_{15}^* = 0.582, S_{16}^* = 0.583, \text{ and } S_{17}^* = 0.28$$

As a result, the distance of first alternative from the fuzzy ideal alternative is equal to:

$$S_j^* = 0.28 + 0.58 + 0.58 + 0.38 + 0.70 + 0.45 + 0.32 = 3.3$$

The distance of first alternative from the fuzzy anti-ideal alternative of each of the criteria is calculated as follows:

Table 15. the values of any alternative distance from the ideal alternative.

$d(A_i, A^*)$	Bedding	permeability	porosity	Joint distance	Opening Joint	RQD	Thickness	S *
$d(A_1, A^*)$	0.28	0.58	0.58	0.38	0.70	0.45	0.32	3.3
$d(A_2, A^*)$	0.28	0.37	0.58	0.49	0.70	0.65	0.36	3.43
$d(A_3, A^*)$	0.31	0.37	0.44	0.38	0.70	0.45	0.36	3.01
$d(A_4, A^*)$	0.26	0.221	0.22	0.49	0.54	0.65	0.27	2.65
$d(A_5, A^*)$	0.31	0.366	0.44	0.38	0.70	0.45	0.32	2.97
$d(A_6, A^*)$	0.26	0.221	0.22	0.49	0.54	0.65	0.36	2.74
$d(A_7, A^*)$	0.36	0.366	0.44	0.38	0.70	0.45	0.32	3.02

Table 16. The values of any alternative distance from the anti-ideal alternative.

$d(A_i, \bar{A})$	Bedding	permeability	porosity	Joint distance	Opening Joint	RQD	Thickness	S
$d(A_1, \bar{A})$	0.31	0.28	0.33	0.42	0.37	0.61	0.26	2.58
$d(A_2, \bar{A})$	0.31	0.45	0.33	0.16	0.37	0.39	0.19	2.2
$d(A_3, \bar{A})$	0.26	0.45	0.48	0.42	0.37	0.61	0.19	2.78
$d(A_4, \bar{A})$	0.31	0.76	0.65	0.42	0.57	0.39	0.33	3.17
$d(A_5, \bar{A})$	0.26	0.45	0.48	0.16	0.37	0.61	0.26	2.86
$d(A_6, \bar{A})$	0.31	0.76	0.65	0.42	0.57	0.39	0.19	3.03
$d(A_7, \bar{A})$	0.19	0.45	0.48	0.42	0.37	0.61	0.26	2.78

Table 17. The values of distance from the ideal and anti-ideal alternative and the similarity attribute for any alternative.

KM2	KI1	KM1	KI2	KM2	Kd	Kcs	
3.02	2.74	2.97	2.65	3.01	3.43	3.3	the distance of alternative from the ideal alternative
2.78	3.03	2.86	3.17	2.78	2.2	2.58	the distance of alternative from the anti-ideal alternative
0.479	0.525	0.491	0.545	0.481	0.391	0.439	similarity index

$$S_i^- = \sum_{j=1}^n (\tilde{v}_{ij}^-, \tilde{v}_j^-), \quad i = 1, 2, \dots, m \tag{10}$$

For example for $S_{11}^- - S_{17}^-$:

$$S_{17}^- = \sqrt{\frac{1}{3}[(0.05 - 0.03)^2 + (0.2 - 0.03)^2 + (0.45 - 0.03)^2]} = 0.263$$

$$\begin{matrix} S_{11}^- = 0.31, & S_{12}^- = 0.28, & S_{13}^- = 0.33, \\ S_{14}^- = 0.42, & S_{15}^- = 0.33, & S_{16}^- = 0.61 \end{matrix}$$

Consequently, the distance of first alternative from the fuzzy ideal alternative or the closeness coefficients(similarity index) of each supplier according to distance from the fuzzy positive-ideal solution (FPIS), S^* and the fuzzy negative-ideal solution (FNIS), S^- , can be calculated as follows:

$$CC_i = \frac{S_i^-}{S_i^* + S_i^-} \quad i = 1, 2, \dots, m \tag{11}$$

For example S_{11}^- and CC_1 (For Conglomerate and Sandstone Unit or Kcs) is calculated as follows:

$$S_{11} = 0.31 + 0.28 + 0.33 + 0.42 + 0.37 + 0.61 + 0.26 = 2.58$$

$$CC_{1(Kcs)} = \frac{2.58}{3.3 + 2.58} = 0.439$$

Thus, the similarity attribute for the alternative is equal to:

$$\begin{matrix} CC_{2(Kd)} = 0.391, & CC_{3(KML)} = 0.481, & CC_{4(KL1)} = 0.545, \\ CC_{5(KM1)} = 0.491, & CC_{6(KL2)} = 0.525, & CC_{7(KML2)} = 0.479 \end{matrix}$$

Similar calculation have been done for the other alternatives, and the calculation results for the distance of any alternative from the ideal and anti-ideal alternative has been inserted in the Tables 15-17.

Each of the lithologic units whose its similarity attribute is better than the other units, has more potential unit to become the karstic aquifer. Thus, according to the results obtained from Table 17, the unit KL1 and KL2 are the best units to form the karstic aquifer, and the other units in the area have moderate and weak karstic aquifer conditions.

Conclusions

The objective of present research is to identify the most developed karstic lithologic unit

of Haftad Gholleh area in South-eastern Arak in Iran, and the study has been done using the Similarity to Ideal Solution method.

This research indicates that the karst of Haftad Gholleh area can be classified into seven separate lithologic units which they are different by structural and hydraulic properties.

According to the research, the lower massive limestone or KL1 unit is the most important lithologic unit to form the karst of the area and after that, KL2 unit has been effective in forming the karst. Also, Base Lithologic unit of Cretaceous, include conglomerate and sandstone, the least karstic water reservoirs, does not play a important role to form the karst of Haftad Gholleh.

Bibliography

- Abo-Sinna M.A., Amer A.H., 2005, Extensions of TOPSIS for multiobjective large-scale nonlinear programming problems. *Applied Mathematics and Computation*, 162, 243-256.
- Agassi A.W., Afrasiabi A., 2004, Karst Hydrology", translation, publication *The Design of Providing the Water Engineering Standards in the Country*, 207. p.
- Agrawal V. P., Kohli V., Gupta S., 1991, Computer aided robot selection: The multiple attribute decision making approach. *International Journal of Production Research*, 29, 1629-1644.
- Cheng S., Chan C.W., Huang G.H., 2003, An integrated multi-criteria decision analysis and inexact mixed integer linear programming approach for solid waste management. *Engineering Applications of Artificial Intelligence*, 16, 543-554.
- Deng H., Yeh C.H., Willis R.J., 2000, Inter-company comparison using modified TOPSIS with objective weights. *Computers and Operations Research*, 27, 963-973.
- Emami H., 1992, Exploration of Qom Quadrangle, scale 1/250000, *Geology survey of Iran*, 4. p.
- Feng C. M. & Wang R. T., 2001, Considering the financial ratios on the performance evaluation of highway bus industry. *Transport Reviews*, 21, 449-467.
- Hwang C.L., Yoon K., 1981, *Multiple attribute decision making: Methods and applications*. Springer. Berlin.

- Jee D.H., Kang K.J., 2000, A method for optimal material selection aided with decision making theory. *Materials and Design*, 21, 199–206.
- Kim G., Park C.S., Yoon K.P., 1997, Identifying investment opportunities for advanced manufacturing systems with comparative integrated performance measurement. *International Journal of Production Economics*, 50, 23–33.
- Lai Y.J., Liu T.Y., Hwang C.L., 1994, TOPSIS for MODM. *European Journal of Operational Research*, 76, 486–500.
- Liao H.C., 2003, Using PCR-TOPSIS to optimize Taguchi's multi-response problem. *The International Journal of Advanced Manufacturing Technology*, 22, 649–655.
- Maxey G.B., 1964, Hydrostratigraphic units, *Journal of Hydrology*, 2, 124–129.
- Olson D.L., 2004, Comparison of weights in TOPSIS models. *Mathematical and Computer Modelling*, 40, 721–727.
- Opricovic S., Tzeng G.H., 2004, Compromise alternative by MCDM methods: A comparative analysis of VIKOR and TOPSIS. *European Journal of Operational Research*, 156, 445–455.
- Parkan C., Wu M.L., 1997, On the equivalence of operational performance measurement and multiple attribute decision making. *International Journal of Production Research*, 35, 2, 963–2,988.
- Seaber P.R., 1988, Hydrostratigraphic units, The Geology of North America, *Geological Society of America*, 2, 9–14.
- Tong L.I., Su C.T., 1997, Optimizing multi-response problems in the Taguchi method by fuzzy multiple attribute decision making. *Quality and Reliability Engineering International*, 13, 25–34.
- Triantaphyllou E., Lin C., 1996, Development and evaluation of five fuzzy multiattribute decision-making methods, *International Journal of Approximate Reasoning*, 14, 281–310.
- Van Wagoner R.M., Mitchum R.M., Campion K.M., Rahmanian V.D., 1990, *Siliclastic sequence stratigraphy in well logs, cores, and outcrops: Concepts for high-resolution correlation of time and facies*, *American Association of Petroleum Geologists Methods in Exploration Series*, 7, 55–59.
- Zanakis S.H., Solomon A., Wishart N., Dubish S., 1998, Multi-attribute decision making: A simulation comparison of select methods. *European Journal of Operational Research*, 107, 507–529.

Viscoelastic modeling and factor Q for reflection data

Vladimir Sabinin*

Received: October 27, 2011; accepted: June 10, 2012; published on line: September 28, 2012

Resumen

Los modelos numéricos viscoelásticos, basados en el concepto de mecanismos de dispersión, toman en cuenta las variables de memoria y algunos parámetros de dispersión, a saber los tiempos de relajación de tensión. En la práctica de la geofísica, el factor de calidad Q se usa normalmente para describir una propiedad de atenuación de medios viscoelásticos. Para el modelado numérico, es útil saber qué dependencia existe entre el factor Q y los tiempos de relajación.

En lugar de derivar la dependencia teóricamente, en el reciente trabajo, esta se evalúa de los resultados de un experimento numérico para la estimación del factor Q de datos sintéticos de reflexión. Para obtener los sismogramas sintéticos, un nuevo modelo 3D numérico de propagación de las ondas en medios viscoelásticos se desarrolló, difiriendo de los anteriores en que utiliza los valores medios de parámetros de relajación en los casos de mecanismos de dispersión múltiples y aplicando una nueva modificación del límite absorbente PML. Para la estimación del factor Q , se usaron métodos numéricos con la opción manual de ventanas espectrales. Estos métodos se adaptaron para los datos de reflexión. La fórmula desarrollada de la dependencia de Q en los tiempos de relajación es cualitativamente buena en la gama amplia de los tiempos de relajación.

Palabras clave: medios viscoelásticos, mecanismo de dispersión, tiempos de relajación, modelo numérico, PML, factor de calidad Q .

Abstract

Viscoelastic numerical models, based on a concept of dissipation mechanisms, take into account memory variables, and some dissipation parameters, namely stress and strain relaxation times. In geophysical practice, the quality factor Q is widely used for describing an attenuation property of viscoelastic media. For numerical modeling, it is useful to know what dependence exists between the factor Q , and the relaxation times.

Instead of deriving this dependence theoretically, in recent work, it is evaluated from results of numerical experiment for estimating the factor Q in synthetic reflection data. For obtaining the synthetic seismograms, a new 3D numerical model of wave propagation in viscoelastic media is developed, differing from previous ones by utilizing average values of relaxation parameters in cases of multiple dissipation mechanisms, and by applying a new modification of PML absorbing boundary. For the estimation of factor Q , numerical methods are used with manual choice of spectral windows. These methods are adapted for surface reflection data. The developed formula of the dependence Q on relaxation times is qualitatively good in a wide range of relaxation times.

Key words: viscoelastic media, dissipation mechanism, relaxation times, numerical model, PML, quality factor Q .

V. Sabinin*
Instituto Mexicano del Petróleo
Eje Central Lázaro Cárdenas 152
Col. San Bartolo Atepehuacan
C.P. 07730
México D.F., México
*Corresponding author: vsabinin@yahoo.com

Introduction

Viscoelastic properties of oil-gas reservoirs cause high attenuation of seismic waves. Mathematical models of wave propagation in viscoelastic media can be useful for investigation of seismic attenuation in oil-gas reservoirs. The attenuation can be introduced into an elastic model in different ways. One of the most theoretically interesting is the method of dissipation mechanisms (Carcione *et al.*, 1988; Robertsson *et al.*, 1994; Xu and McMechan, 1998; Mikhailenko *et al.*, 2003; Sabinin *et al.*, 2003). It supposes that the viscoelastic property can be described by action of some dissipation mechanisms which are characterized by stress and strain relaxation times, and by type of interaction.

In the practice, it is more convenient to have lesser number of parameters for describing attenuation, for instance, one - the quality factor Q . Definition of the dependence between the relaxation times and the factor Q will facilitate an application of the models. It is known that the Q factor is nearly independent on frequency (Knopoff, 1964) in seismic spectrum, and it can be composed by some (>1) dissipation mechanisms with suitably fitted values of relaxation times (Emmerich, 1992; Blanch *et al.*, 1995; Xu and McMechan, 1995, 1998). But nobody did comparison the composed input values of factor Q with the output values obtained from viscoelastic modeling. This issue may be also connected namely with a problem of correct definition of the factor Q .

Below, an attempt is made to derive the formula for dependence of the factor Q on relaxation times by estimating directly the factor Q output from synthetic seismograms computed by the viscoelastic numerical model. For the correct modeling, I revised the numerical model Virieux (1986), and Robertsson *et al.* (1994), and added to it my modification of the absorbing boundary layer by Collino and Tsogka (2001). Additionally, I developed a methodology of correct estimation of factor Q in surface reflection data for using this typical problem of seismology in numerical experiment.

Viscoelastic Model

In the linear theory of viscoelasticity, for the standard linear solid model of relaxation, stress σ_{ij} depends on strain ε_{ij} by the following modified Hooke's law:

$$\sigma_{ij} + \tau_{\sigma} \dot{\sigma}_{ij} = G_{ijkl} (\varepsilon_{kl} + \tau_{\varepsilon} \dot{\varepsilon}_{kl}) \quad (1)$$

where G_{ijkl} - the stiffness tensor, τ_{ε} and τ_{σ} the strain and stress relaxation times.

Following Liu *et al.* (1976), one can derive the Boltzmann's after-effect equation directly from (1):

$$\dot{\sigma}_{ij} * \phi(t) = G_{ijkl} \varepsilon_{kl} \quad (2)$$

where $*$ denotes the convolution in time, and $\phi(t)$ is the specific creep function. For one dissipation mechanism,

$$\phi(t) = [1 - \tau \exp(-t / \tau_{\varepsilon})] \theta(t) \quad (3)$$

where θ - the Heaviside function, and $\tau = 1 - \tau_{\sigma} / \tau_{\varepsilon}$, provided $\tau_{\varepsilon} > \tau_{\sigma}$. For small $t << \tau_{\varepsilon}$, it corresponds to the hyperbolic creep function used by Lomnitz (1957).

By taking the time derivative of (2), and substituting the dependence of strain on the particle velocity

$$\dot{\varepsilon}_{ij} = \frac{1}{2} (\partial_i v_j + \partial_j v_i) \quad (4)$$

one can get:

$$\dot{\sigma}_{ij} * \dot{\phi} = L_{ij} \quad (5)$$

where following Carcione (1993), and Xu and McMechan (1995) :

$$L_{ii} \equiv (\lambda + 2\mu) \partial_i v_i + \lambda \partial_j v_j, \quad j \neq i,$$

$$L_{ij} \equiv \mu (\partial_i v_j + \partial_j v_i), \quad i \neq j,$$

where λ and μ - Lamé elastic constants, $\{i=x,z; j=x,z\}$ for two-dimensional viscoelastic media, and $\{i=x,y,z; j=x,y,z\}$ for three-dimensional viscoelastic media.

By expanding in the convolution the time derivative of ϕ (see Robertsson *et al.*, 1994), one can get from (5):

$$(1 - \tau) \dot{\sigma}_{ij} = L_{ij} - \tau r_{ij} \quad (6)$$

where r_{ij} - the so-called memory variable:

$$\tau_{\varepsilon} r_{ij} = \exp(-t / \tau_{\varepsilon}) \theta(t) * \dot{\sigma} \quad (7)$$

By taking the time derivative of (7), one can get the equation for the memory variable:

$$\tau_{\sigma} \dot{r}_{ij} + r_{ij} = L_{ij} \quad (8)$$

Combining (6) and (8), one can obtain a more convenient form of (6):

$$\dot{\sigma}_{ij} = L_{ij} + (\tau_{\varepsilon} - \tau_{\sigma})\dot{r}_{ij} \quad (9)$$

Adding Newton's second law

$$\rho\dot{v}_i = \partial_j \sigma_{ij} \quad (10)$$

yields the system of equations (8)–(10) for the seismic wave propagation in the viscoelastic media, which governs the stress σ_{ij} , the particle velocity v_i , and the memory variable r_{ij} in the area of modeling for the case of one dissipation mechanism.

In the case of $\tau_{\sigma} = \tau_{\varepsilon}$, the system (8)–(10) becomes the system for elastic media.

By substituting $E_{ij} = \sigma_{ij} - (\tau_{\varepsilon} - \tau_{\sigma})r_{ij}$, one can transform (9) into the equation for elastic media $\dot{E}_{ij} = L_{ij}$, and obtain from (8):

$$\tau_{\sigma}\dot{\sigma}_{ij} + \sigma_{ij} = \tau_{\varepsilon}\dot{E}_{ij} + E_{ij} \quad (11)$$

The equation (11) is similar to equation (1), and can be derived directly from it by defining $E_{ij} = G_{ijkl}\varepsilon_{kl}$. Therefore, the value E has a sense of the elastic part of the stress σ . Thus, the equation (11) governs an effect of viscosity, and it is an equation on only time.

Possibly, we ought to consider two sets of relaxation times: for shear and compressional waves, and modify the equations (8) and (9) by a way following Carcione (1995), for example. But Xu and McMechan (1995) simplified the problem by supposing equal relaxation times for shear and compressional waves. Another way of simplification is to consider cases of multiple dissipation mechanisms which can be transformed to the case of one dissipation mechanism, as below.

Extention of the model to N dissipation mechanisms

For the general case of N dissipation mechanisms which differ only by values of τ_{ε} , and τ_{σ} , we should write equations (1) and (2) for each n -th dissipation mechanism as follows:

$$\sigma_{nij} + \tau_{\sigma n}\dot{\sigma}_{nij} = G_{ijkl}(\varepsilon_{nkl} + \tau_{\varepsilon n}\dot{\varepsilon}_{nkl}) \quad (12)$$

$$\dot{\sigma}_{nij} * \phi_n(t) = G_{ijkl}\varepsilon_{nkl} \quad (13)$$

Values of total σ_{ij} and ε_{ij} over N dissipation mechanisms depend on scheme of interactions (interconnections) of the mechanisms: which mechanisms interact as parallel or as sequential,

and which groups of mechanisms interact with other groups as parallel or sequential.

Really, the scheme of interactions of mechanisms is not known beforehand, and the problem of modeling does not need such fine developing.

For three simple cases below, it is possible to reduce the system of equations for N mechanisms to the case of one mechanism. They are: 1) N mechanisms interacting sequentially, 2) N mechanisms interacting in parallel, and 3) two independent groups: one including N_1 mechanisms interacting sequentially, and the second including N_2 mechanisms interacting in parallel, $N_1 + N_2 = N$. These are general enough cases.

For the case 1), the creep function can be represented as follows (for details see Appendix A):

$$\phi(t) = [1 - \frac{1}{N} \sum_{n=1}^N \tau_n \exp(-t/\tau_{\varepsilon n})]\theta(t) \quad (14)$$

If introduce the average values of relaxation times:

$$\bar{\tau}_{\varepsilon} = \frac{1}{N} \sum_{n=1}^N \tau_{\varepsilon n}, \quad \bar{\tau}_{\sigma} = \frac{1}{N} \sum_{n=1}^N \tau_{\sigma n}, \quad \bar{\tau} = 1 - \frac{\bar{\tau}_{\sigma}}{\bar{\tau}_{\varepsilon}},$$

then, from (5) with (14), one can derive (for details see Appendix B) similar equation to (6):

$$(1 - \bar{\tau})\dot{\sigma}_{ij} = L_{ij} - \bar{\tau}R_{ij} \quad (15)$$

where R_{ij} is the average memory variable, which can be found from the following similar equation to (8):

$$\bar{\tau}_{\sigma}\dot{R}_{ij} + R_{ij} = L_{ij} \quad (16)$$

For the case 2), the equation (5) becomes as follows:

$$\dot{\sigma}_{ij} = \dot{\phi}_1 * L_{ij} \quad (17)$$

in which the creep function is (see Appendix A, and Carcione, 1995)

$$\phi_1 = [1 + \frac{1}{N} \sum_{n=1}^N \tau_{1n} \exp(-t/\tau_{\sigma n})]\theta(t) \quad (18)$$

where $\tau_{1n} = \frac{\tau_{\varepsilon n}}{\tau_{\sigma n}} - 1$.

For the case 3), the equation (5) is valid for the first group, and the equation (17) is valid for the second group.

In the case 2), from (17) with (18), and in the case 3), from (5) with (14), and from (17) with (18), one can derive the same equations (15) and (16) for the stress, and for the average memory variable (see Appendix B).

Consequently, (if use is done the average memory variable and the average values of relaxation times), one may clearly see that the equations for the considered cases of N mechanisms (15)–(16) are equivalent to equations (6) and (8) for the case of one dissipation mechanism.

From this equivalence, it follows that, for a fixed geometry of the problem, the value of Q depends only on values of $\bar{\tau}$, and $\bar{\tau}_\sigma$, and on the source of seismic wave.

Anyway, the solution of equation (11), which is similar to (1), is basic for the case of N mechanisms. Therefore, we will consider the equations for one dissipation mechanism (8) and (9) as the basic equations, and for this case, will calculate the dependence of factor Q on the average relaxation times of the media.

Solution method for the model

The system of equations (8)–(10) is solved by the finite-difference method with using the PML for boundary conditions. The finite-difference scheme has the following form:

$$\tau_\sigma \dot{R}_{ij}^n + R_{ij}^n = L_{ij}(v_i^n), \quad (19a)$$

$$\frac{\sigma_{ij}^{n+1} - \sigma_{ij}^n}{\Delta t} = L_{ij}(v_i^n) + (\tau_\varepsilon - \tau_\sigma) \dot{R}_{ij}^n, \quad (19b)$$

$$\rho \frac{v_i^{n+1} - v_i^n}{\Delta t} = \partial_i \sigma_{ii}^{n+1} + \check{\partial}_j \sigma_{ij}^{n+1}, \quad j \neq i, \quad (19c)$$

where

$$L_{ij}(v_i^n) = (\check{\lambda}_i + 2\check{\mu}_i) \check{\partial}_i v_i^n + \check{\lambda}_j \check{\partial}_j v_j^n, \\ L_{ij}(v_i^n) = \check{\mu}_i \partial_i v_i^n + \check{\mu}_j \partial_j v_j^n, \quad j \neq i$$

Here $i, j=1,2,3$ – are the indexes of direction, $n=0,1,2,\dots$ – the mesh index in time, Δt – the time increment. Space derivatives are defined as follows:

$$\partial_i u = (u_{k-1} - 27u_k + 27u_{k+1} - u_{k+2}) / (24h_i), \\ \check{\partial}_i u = (u_{k-2} - 27u_{k-1} + 27u_k - u_{k+1}) / (24h_i),$$

where h_i – the space step in the i -direction, and k – the space mesh index in the i -direction. If an inner boundary of the area coincides with a middle line between the nodes, the average coefficients $\check{\mu}_i$, $\check{\lambda}_i$, and $\check{\mu}_i$ for the inner boundary are calculated as follows:

$$\check{\mu}_i = 2\mu_k \mu_{k-1} / (\mu_k + \mu_{k-1}), \\ \check{\mu}_i = 2\mu_k \mu_{k+1} / (\mu_k + \mu_{k+1}).$$

The scheme (19) is written for a fixed grid ($k_i=0, \dots, I; k_j=0, \dots, J; k_k=0, \dots, K; n=0, 1, 2, \dots$), and has the order of approximation $O(\Delta t^2, h^4)$. It is practically equivalent to the “staggered” scheme used by Virieux (1986), and by Robertsson *et al.* (1994), but it operates only with integer values of indexes, as classical schemes, what is achieved by appropriate shift of “staggered” indexes.

The equation (19a) can be solved by implicit scheme. It gives:

$$R_{ij}^n = [\Delta t L_{ij}(v_i^n) + \tau_\sigma R_{ij}^{n-1}] / (\Delta t + \tau_\sigma) \quad (20)$$

The necessary stability condition for the scheme (19)–(20) in the 3D case is:

$$\sqrt{3.5} V_p \sqrt{\frac{\Delta t + 2\tau_\varepsilon}{\Delta t + 2\tau_\sigma}} \frac{\Delta t}{h} \leq 1,$$

where $h = \sqrt{3 / (h_x^{-2} + h_y^{-2} + h_z^{-2})}$.

If applying the Ricker wavelet for a seismic source, the following condition is used additionally:

$$\max(\Delta x, \Delta y, \Delta z) < \min(V_s) / (16f), \quad (21)$$

where f – the Ricker wavelet frequency. This condition provides the undamaged form of PP, PS, and SS waves in seismograms. The coefficient 16 is empirical and can be explained by 4-point approximation of space derivatives and 4-slope form of the Ricker wavelet. It should not be less than 4 points at each slope. Other authors suggest different values of the coefficient for schemes of different accuracy: 10 – Virieux (1986), 12 – Moczo *et al.* (1997), 15–20 – Xu and McMechan (1998).

Above, V_p and V_s are velocities of the compressional and shear waves used in definition of the Lamé constants.

In the nodes of the PML absorbing layer, the equations (19b)–(19c) are modified by Collino

and Tsogka (2001). Indeed, I apply another formula for absorbing sink (S_a) in the left hand side of the modified equations (19b,c). It forms the implicit (not centered) scheme with the finite-difference time derivative (Sabinin *et al.*, 2003):

$$S_a = du^{n+1}, \quad (22)$$

where u – the same variable that is in the finite-difference time derivative of the corresponding equation of the system (19).

The parameter d in (22) is calculated by a new formula ($k = x, y, z$ – index of direction):

$$d_k = d_{0k} \left[\exp\left(a \frac{n_k - 0.5}{m_k}\right) + \exp\left(-a \frac{n_k - 0.5}{m_k}\right) - 2 \right]$$

$$d_{0k} = \frac{baV_p}{m_k (e^a - e^{-a} - 2a)} \quad (23),$$

where m_k – the thickness of PML in mesh steps in k -th direction, n_k – number of the node across the PML, $1 \leq n_k \leq m_k$, a, b – matching coefficients (approximately, $a=1, b=10$). The formula (23) is not sensitive to values of the parameters a, b . The PML thickness m_k is recommended to be 20, or more.

Advantage of the finite-difference scheme (19)–(23) is its convenience for parallel computations what are easily done with instructions of Open MP.

Estimation of factor Q

For obtaining dependence of the quality factor Q on relaxation times, let us consider a formula by Liu *et al.* (1976), which is valid under the assumption that τ_ε and τ_σ do not depend on frequency $\omega=2\pi f$ at the specified bandwidth:

$$\tau Q(\omega) = \omega \tau_\sigma + \frac{1}{\omega \tau_\varepsilon}$$

Taking an integral from this expression over some interval of frequency, one can get the formula

$$\tau Q = a\tau_\sigma + \frac{(1-\tau)b}{\tau_\sigma}, \quad (24)$$

where the constant coefficients a , and b are to be evaluated from a numerical experiment. The formula (24) is derived without the assumption $\tau \ll 1$ used by Blanch *et al.* (1995).

From different methods of estimation for factor Q (see, for example, Tonn, 1991), two methods seem as more reliable.

The Spectral Ratio method (SR) will be applied in the following form. From the theory, the ratio of spectral amplitudes of waves reflected from the bottom and from the top of target layer can be expressed as follows:

$$s \equiv \frac{A_b}{A_t} = s_0 \exp(-\beta r),$$

where A_t, A_b – amplitudes of spectra of reflection waves from top and bottom of the target layer in the same ray path, r is a travel distance, and β is an absorption coefficient.

Futterman (1962) defined the quality factor Q as

$$\frac{2\pi}{Q} = 1 - e^{-2d}, \quad (25)$$

where

$$d = \frac{\beta r}{\tau_0 f},$$

f is frequency, and τ_0 is a travel time. It means that $Q > 2\pi$.

From the other hand, one can approximate a logarithm of the same spectral ratio by a line function over a proper interval of f by the least squares method:

$$\ln(s) = -\eta f + \eta_0$$

It means, that estimated d in the interval is:

$$d = \eta / \tau_0 \quad (26)$$

The art of application of this method consists in proper choice of a window for impulse in the time domain, and a window (interval) for the least squares method in the spectral domain.

For the Ricker wavelet which will be used further, the time window must include all three phases of the impulse up to visible noise at the edges. It is a visible width of impulse at the seismogram.

The spectrum of the Ricker impulse has a shape of a bell, and a logarithm of the spectral ratio has a near line part (see Fig. 1). The spectral

window should be chosen inside this line part. It can be made manually. For automatic choice, by observing synthetic seismograms, it was found that a good choice is the window between 0.8 of the peak frequency for the bottom spectrum and the peak frequency for the top spectrum.

The second method used is the Centroid Frequency Shift (FS) method (Quan and Harris, 1993). Here the coefficient η for the formula (26) is calculated by the following formulas:

$$a = \sum_f A_t, \quad b = \sum_f A_b, \quad f_t = \frac{1}{a} \sum_f f A_t, \quad f_b = \frac{1}{b} \sum_f f A_b, \quad v = \frac{1}{a} \sum_f (f - f_t)^2 A_t, \quad \eta = s \frac{f_t - f_b}{v}, \quad (27)$$

where s depends on the shape of spectra, for Gaussian spectra $s=1$ (Quan and Harris, 1993).

The FS method operates with integral values, therefore it is less sensitive to the noise than the SR method, but it is more sensitive to the shape of spectra.

Because of influence of errors on the shape of spectra, it is used the same spectral window for the FS method as for the SR method.

For estimating Q from equations (25)-(26), the value of travel time τ_0 must be calculated, too.

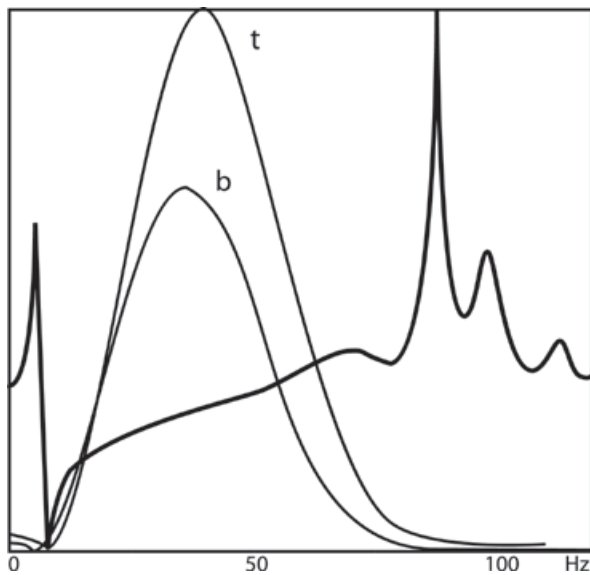


Figure 1. Spectra and a logarithm of its ratio. b: bottom, t: top.

To calculate τ_0 in a multilayered reservoir, a system of non-linear equations can be derived by the ray-tracing method (see Appendix C).

If the target layer is the second from the surface, then the calculations become simpler. Ray paths for this case are presented in Figure 2. One can see that

$$0.5\Delta t = \frac{r_1 - r_0}{V_1} + \frac{r_2}{V_2}, \quad (28)$$

where indexes 1, and 2 denote the number of layer from above, V is V_p , r_0 is the path from a source to the top of target layer for the impulse reflected from the top, r_1 is the same for the impulse reflected from the bottom, r_2 is the path inside the second layer from the top to the bottom of target layer, and Δt is time between the reflected impulses at the trace.

For reflection data, the receivers are at the surface, therefore τ_0 is twice more than travel time between points x , and x_0 .

Using Snell's law, one excludes the velocity V_2 of the target layer from (28):

$$p = \frac{z_1}{\cos \theta_1} + \frac{z_2 \sin \theta_1}{\cos \theta_2 \sin \theta_2}, \quad (29)$$

where $p = 0.5\Delta t V_1 + \sqrt{x_0^2 + z_1^2}$, x_0 is the half of the offset, z_1, z_2 are thicknesses of the layers, and θ_1, θ_2 are travel (incidence) angles.

Denoting the offset value of refraction point for the bottom ray as x (see Fig. 2), one obtains:

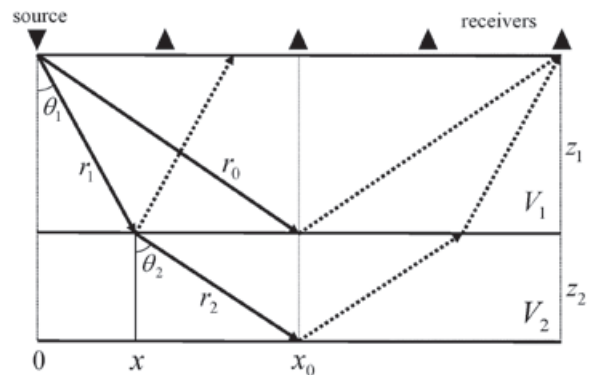


Figure 2. Scheme of P-wave reflections in a three-layer medium.

$$(x_0 - x)(p\sqrt{x^2 + z_1^2} - xx_0 - z_1^2) = xz_2^2 \quad (30)$$

The non-linear equation (30) is solved numerically. The obtained value x is used to calculate the travel time $\tau_0=2r_2/V_2$ of the ray inside the target layer. From (28),

$$\tau_0 = \Delta t + 2(\sqrt{x_0^2 + z_1^2} - \sqrt{x^2 + z_1^2}) / V_1, \quad (31)$$

where V_1 is V_p of the upper layer. The value Δt can be calculated by the correlation function between the impulses at the trace.

Difference between Δt and τ_0 is illustrated in Figure 3. The difference increases with offset significantly.

An advantage of the method (30)-(31) is the exclusion of the unknown velocity V_2 from consideration.

As can be also seen from Fig. 2, for more exact estimating the factor Q , one should use the wave reflected from the point x at the top of target layer to calculate spectral amplitude A_r , but not from the point x_0 which is commonly used for this purpose. Knowing value x from (30), one may obtain this wave (or its spectrum) by interpolation from waves (or spectra) of adjacent traces, with taking into account different values of geometrical spreading.

Another possible problem in estimating Q of the target layer is how to exclude from the consideration the coefficients of reflection and refraction at the boundaries of the viscoelastic target layer. It will be the best result in the estimation of Q if the spectral amplitudes will

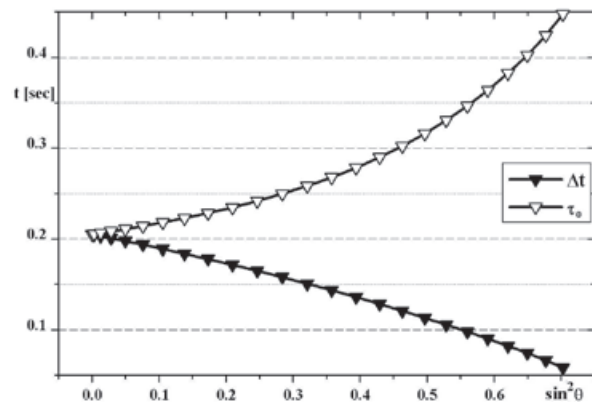


Figure 3. Travel time τ_0 and difference Δt of arrival times calculated in one of the variants for different incidence angles.

differ only because of viscoelastic attenuation inside the layer. Really, the reflection and refraction at the boundaries of the layer may also act:

$$\frac{A_b^R}{A_t^R} = \frac{A_b R_b P_{tb} P_{bt}}{A_t R_t},$$

where A^R - real amplitude, R - coefficient of reflection, P - coefficient of refraction.

If R and P would depend on f then they influenced on value of Q . However, practice shows that influence of reflection/refraction coefficients on the estimated values of Q is less than difference in estimated values Q caused by different smart choices of the time and spectral windows.

Both methods SR and FS give close values Q but FS insufficiently less.

Numerical simulation

I use the developed numerical model for obtaining the synthetic seismograms of waves reflected from the top and bottom boundaries of a horizontal viscoelastic layer. Then I estimate the factor Q from the seismograms with different τ , and τ_{σ} , and put these values into the left-hand side of the formula (24) to estimate the values of the coefficients a, b of the formula (24) by least squares method.

The computation of synthetic seismograms by the viscoelastic model was performed at a workstation which gave possibility to parallelize calculations into 24 threads. But it was too slow for a 3D model. For economy, a 2D problem was chosen for the numerical experiment, as follows.

At the earth surface, there was one wave source, and a set of equally spaced (every 100 meters) receivers (the common source point observation system). The area of width 5000 m and depth 2250 m consisted of three homogeneous layers, the target viscoelastic layer was the second, beginning at the depth 1500 m, and had the thickness 400 m. The other layers were considered as elastic, with $\tau = 0$.

The density, and the elastic velocities of compressional and shear waves were as in Table 1.

Table 1. Media parameters.

Layer	V_p m/sec	V_s m/sec	ρ kg/m ³
1	3500	2000	2000
2	3800	1600	2500
3	2000	1200	2000

Seismic wave source of explosion type was the Ricker wavelet in time, its frequency f_r was set to 15, 30, 45, and 60 Hz, duration of the impulse – 160, 80, 53.3, and 40 ms correspondingly.

The mesh sizes of the finite-difference grid were $h_x=5m$, $h_z=2.5m$, and the time step was 0.2 ms. The PML thickness was equal to 40 nodes. The PML was not mounted at the earth surface where the source was set.

The typical seismogram of v_z obtained for this 2D problem is shown in Figure 4. First two fronts of PP-waves were used for estimating the factor Q . PP waves reflected from the bottom of area (1400–1500 ms), and direct waves reflected from the vertical sides of area are not visible. It means a good effectiveness of applied modification of PML absorbing boundaries.

For comparison, the 3D problem was computed in the variant of $f_r = 30$ Hz, $\tau = 0.7$, and $\tau_\sigma = 0.625$ ms. The 3D area had an additionally y-direction with thickness 2000 m. The receivers were spaced in the middle line. For saving time of computation, a rough grid was used: $h_x=h_y=20$ m, and the time step 0.4ms.

The seismogram of v_z obtained for the 3D problem is shown in the Figure 5. Visible distortions are caused by the roughness of grid

The Figure 5 corresponds to the variant of Figure 4. Values of factor Q calculated for seismograms of Figures 4, and 5 are practically the same, and are equal to 14.8.

The comparison is good enough to decide to apply more economical 2D model in the numerical experiment.

Numerical results

Factor Q was calculated with the SR method for all offsets and did not show any stable or significant dependence on the offset. Existing errors were caused by small distortions of waves by interference with waves reflected from the sides of area, and by errors in setting the time windows.

Difference in Q on offsets was up to 6% of magnitude for small values $\tau_\sigma (<0.0002)$, and up to 12% for large values $\tau_\sigma (>0.01)$, with 0.5%–3% for a middle values, what can be adopted as an error for the estimation of Q .

Difficulty in calculation of the factor Q is that the linear part of logarithm of spectral ratio which one can see in Figure 1 is not clearly present for extreme values of relaxation times. For example, it is a curve for large values τ_σ . Therefore, this gave unreliable values of Q sometimes.

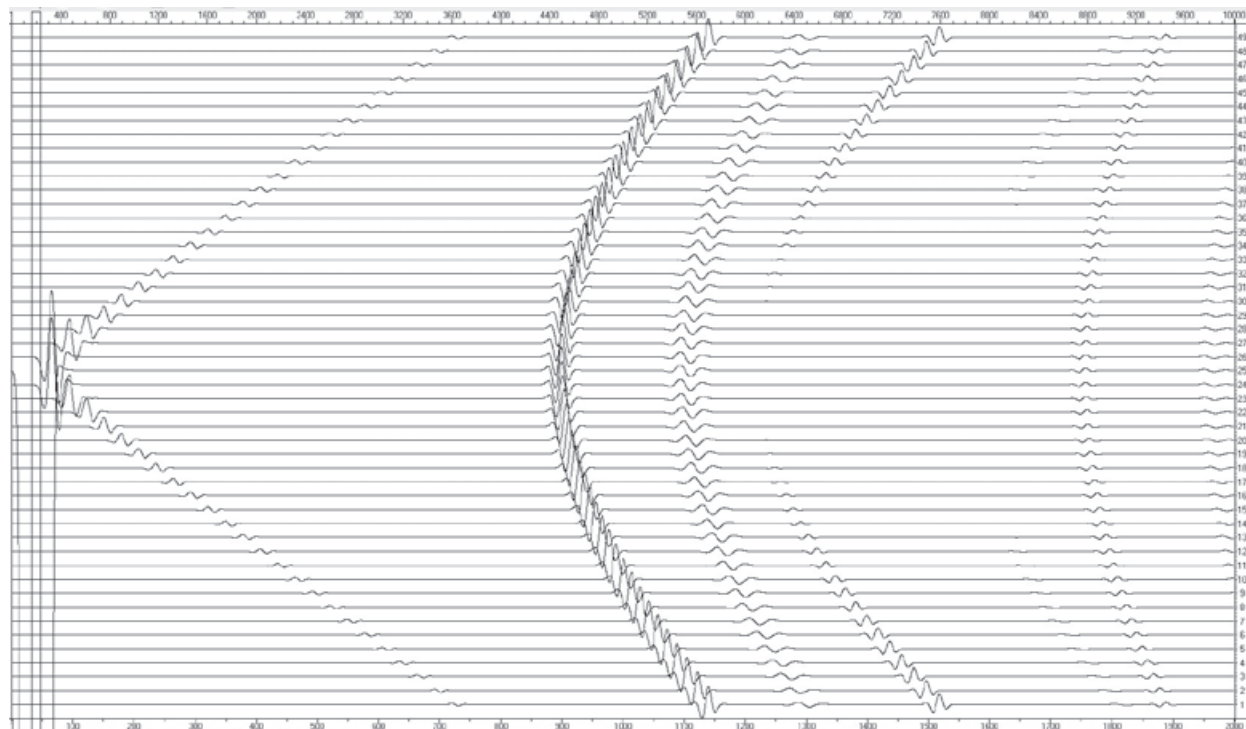


Figure 4. Seismogram of direct P, and reflected PP, and PS waves (v_z) for the 2D problem.

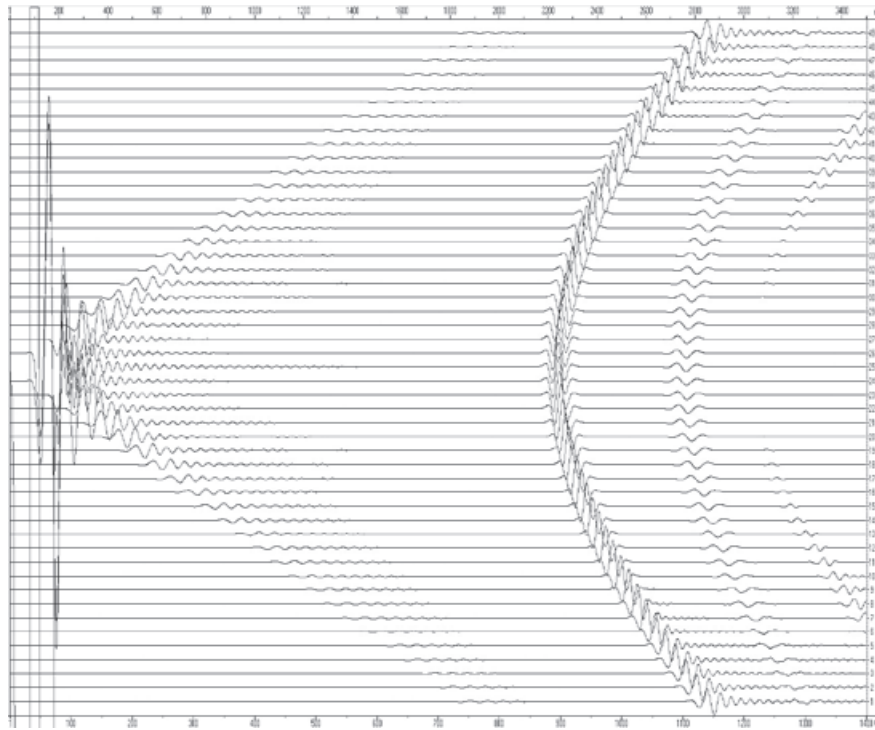


Figure 5. Seismogram of direct P, and reflected PP waves (v_r) for the 3D problem.

Table 2. Computed values of Q for $f_r=15$, and different values of τ , and τ_σ .

$\tau \setminus 3/(f_r \tau_\sigma)$	10	20	40	80	160	320
0.05	172	61	46.5	63.3	115	190
0.1	107	34.1	25.5	35.4	64.2	115
0.2	68.7	24.2	16.9	21.5	36.8	66
0.3	57	16.9	13.5	15.9	26.8	46.6
0.4	51.4	14.3	10.4	13.1	21.3	37.5
0.5	48.3	12.7	9.35	11.3	18.1	31.6
0.6	47.5	11.5	8.6	10.4	15.1	25.8
0.7	43.4	10.7	8.0	9.9	14.1	23.9
0.8	33.9	10.3	7.7	9.4	13.2	21.3
0.9	31.9	10.1	7.4	9.1	12.1	19.6
0.95	29.9	9.7	6.8	8.8	11.6	18.6

Table 3. Computed values of Q for $f_r=30$, and different values of τ , and τ_σ .

$\tau \setminus 3/(f_r \tau_\sigma)$	10	20	40	80	160	320
0.05	201	59.9	48.7	73	128	236
0.1	115	43.7	31	40.6	72	132
0.2	67	22.5	17.9	23.3	39.6	72.2
0.3	51.8	14.8	13.14	17.3	28.3	52.5
0.4	47.7	11.5	10.65	14.7	22.6	39.2
0.5	42.6	9.73	9.72	12.4	19.3	33.3
0.6	41	8.46	8.85	11.7	17.5	29.9
0.7	39.6	7.97	8.2	11.2	15.6	26.1
0.8	38.4	7.38	7.81	9.55	14.7	23.8
0.9	37.8	7.02	7.35	9.44	13.8	22.5
0.95	37.2	7.02	7.31	9.08	13.2	21.4

Table 4. Computed values of Q for $f_r=45$, and different values of τ , and τ_σ .

$\tau \setminus 3/(f_r \tau_\sigma)$	10	20	40	80	160	320
0.05	196	84	46	74	128	221
0.1	128	43	32	41.8	72.2	131
0.2	73	18.6	18.5	24.2	41.1	71.4
0.3	55.6	12.8	13.45	17.4	30.6	52.8
0.4	46.8	10	11.4	14.8	24.5	41.2
0.5	43	8.9	9.8	14.4	21	36.2
0.6	41.8	7.8	9.1	12	17.7	31.3
0.7	41	7.4	8.5	11.3	16.8	27.8
0.8	40	7.0	8.0	10.4	15.1	25.2
0.9	39.9	6.8	7.5	9.85	14.35	23.4
0.95	39.7	6.7	7.2	9.77	13.8	22.6

Table 5. Computed values of Q for $f_r=60$, and different values of τ , and τ_σ .

$\tau \setminus 3/(f_r \tau_\sigma)$	10	20	40	80	160	320
0.05	197	79	61.2	74.8	129	211
0.1	128	34.4	35.2	44.5	78.8	132
0.2	71	16.8	20.1	23.5	43.7	75.5
0.3	55.5	11.7	14.2	21.4	31.7	55.9
0.4	48.8	9.45	11.84	17.4	26.9	44.8
0.5	47	8.1	10.4	15.4	22	36.6
0.6	46	7.5	9.4	13.1	18.5	31.6
0.7	44	7.15	8.9	11.9	17.4	28.5
0.8	42.3	6.88	8.35	11.3	16.1	26.2
0.9	41.4	6.7	8.2	10.6	15.2	22.6
0.95	41.1	6.65	7.7	10.1	14.7	21.4

The results of calculation of factor Q in a wide range near normal incidence are presented in Tables 2–5 for the source frequencies of $f_r=15, 30, 45, 60$ Hz respectively.

As equations (8), (9) depend on τ and τ_σ , so the values Q in the Tables 2–5 are presented depending on these parameters. Also, the results depend on the frequency of the source significantly.

It was found that equation (24) does not match satisfactory to Tables 2–5. Instead, the following similar equation was derived for this:

$$l/d = A/(xy) + B/y + C/y, \tag{32}$$

where d depends on Q by formula (25), $x = \tau^\alpha$, $y = [3/(f_r \tau_\sigma)]^\beta$. Values $\alpha=0.7$, and $\beta=1.2$ represent a near optimal choice.

The obtained coefficients A, B , and C of (32) are presented in Table 6 with values of relative estimation error by (32).

One can compare values Q calculated by (32) for $f_r=45$ in Table 7 with values from Table 4.

For practical use, one can apply Tables 2–5, or equation (32), or derive an own approximation formula.

Table 6. Coefficients for equation (32).

f_r	A	B	C	Rel. error
15	100.4	0.0079	0.0040	0.138
30	108.1	0.0096	0.0058	0.138
45	113.2	0.0091	0.0045	0.135
60	113.9	0.0089	0.0036	0.156

Discussion

Some authors (Blanch *et al.*, 1995; Xu and McMechan, 1998) guess that the constant value Q over some interval of spectral frequency, which one can usually see, is equal to a near constant value Q on an average graphic consisting of the separate theoretical graphics Q (as by Liu *et*

Table 7. Estimated values of Q by (32) for $f_r=45$.

$\tau \setminus 3/(f_r \tau_\sigma)$	10	20	40	80	160	320
0.05	189	90.7	56.1	60.3	106	228
0.1	118	56.9	35.4	37.4	64.3	136
0.2	73.6	36.1	22.6	23.3	38.5	79.5
0.3	56.2	27.9	17.6	17.7	28.3	57.1
0.4	46.5	23.3	14.9	14.7	22.6	44.7
0.5	40.2	20.4	13.1	12.7	19.0	36.7
0.6	35.8	18.3	11.9	11.4	16.4	31.0
0.7	32.4	16.8	10.9	10.4	14.5	26.7
0.8	29.8	15.5	10.2	9.58	13.0	23.4
0.9	27.7	14.6	9.66	8.97	11.8	20.7
0.95	26.8	14.1	9.42	8.71	11.3	19.5

al., 1976) for $N > 1$ dissipation mechanisms with different relaxation times. As one can see from (25), this method of obtaining constant Q fails in the case of one dissipation mechanism. Contrary, the experimental formula (32) does not depend on the number of dissipation mechanisms.

Although the formulas (25) – (27) of methods for estimating factor Q are simple, they have several sources for errors. At first, it is a non-linear form of the “line” part of the logarithm of spectral ratio which can be clearly seen in field data. It is necessary smoothing seismograms with noise, and developing new methods of Q -estimation for synthetic seismograms obtained at large τ_σ .

Second, insignificantly different sizes and positions of time windows can give significantly different spectra what is caused by increased role of noise at the edges of impulses. Suitable automatic algorithms for generating the time windows are needed.

Third, a correct estimation of the travel time is needed as one can see from Figure 3.

Finally, a good estimation for the usually unknown impulses reflected from the top of target layer in the point x of Fig.2 is necessary.

Errors from these four sources can give significantly incorrect values Q , up to 50% and more.

I have solved these problems for synthetic seismograms in case of fine spacing the receivers and not large values τ_σ . As the result, Q values calculated here do not depend on offset what must be theoretically for isotropic media, because factor Q is a property of medium only. This is a good criterion for correctness of methods for estimating Q . If one sees a factor Q depending

on offset (see for example Dasgupta and Clark, 1998), it means that the medium is anisotropic or there are the errors in algorithm of estimating Q .

As known, PML absorbing boundary does not exclude completely reflections from the boundaries of area for finite-difference problems. The modification of PML presented here decreases the reflections in comparison with classical PML by Collino and Tsogka (2001) due to lucky choice of exponent functions for approximation (23).

Errors of the approximated formula (32) for dependence Q on relaxation times are in agreement with errors of estimating Q . For example, if it is excluded the first and ultimate columns from Table 2, then the error of estimation by (32) becomes twice less.

Conclusion

A numerical 3D model for seismic wave propagation in viscoelastic media is developed, which differs from the previous (Robertsson *et al.* 1994) by modification of the finite-difference scheme, and by including the improved variant of PML absorbing boundary.

It is shown that the numerical model for one dissipation mechanism can be directly applied to three simple schemes of interaction of N dissipation mechanisms by using average relaxation times.

The synthetic seismograms are obtained for 3D, and 2D variants of a reservoir which show close values of factor Q in the viscoelastic layer.

The methodology of estimation of factor Q for surface reflection data is developed which differs from previous by more exact calculation of travel times for reflected waves, and by manual choice of spectral windows.

The viscoelastic model and the method of Q -estimation are applied to obtaining experimental dependences of factor Q on relaxation times. The approximate formula is suggested for such dependence.

Appendix "A"

Creep functions for N dissipation mechanisms

From the theory of viscoelasticity, for one mechanism of the standard linear solid, the stress response can be written as $G = [k_2 + k_1 \exp(-k_1 t / \eta)] \theta(t)$, where k and η are coefficients in stress expressions for elastic and viscose elements: $\sigma = k \varepsilon$, and $\sigma = \eta \dot{\varepsilon}$ (see Fig. A1).

For N mechanisms interacting in parallel, one can write:

$$G = \sum_{n=1}^N [k_{2n} + k_{1n} \exp(-k_{1n} t / \eta_n)] \theta(t).$$

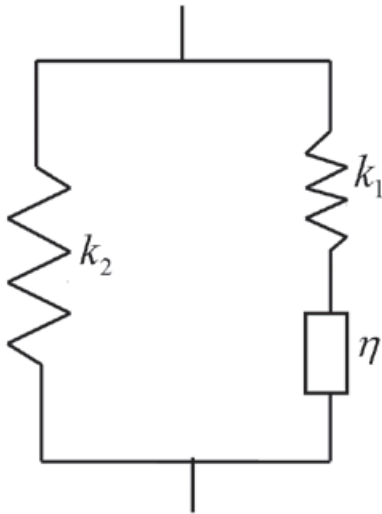


Figure A1. Scheme of standard linear solid.

In this case, the scheme of interactions of mechanisms is equivalent to a parallel scheme with equal values $k_2 = \frac{1}{N} \sum_{n=1}^N k_{2n}$ for elastic elements.

Therefore, defining the relaxation times for each mechanism as

$$\tau_{\sigma n} = \eta_n / k_{1n}, \quad \tau_{\varepsilon n} = \eta_n \left(\frac{1}{k_{1n}} + \frac{1}{k_2} \right),$$

one obtains $k_{1n} = k_2 \left(\frac{\tau_{\varepsilon n}}{\tau_{\sigma n}} - 1 \right)$, and

$$G = k_2 N \left[1 + \frac{1}{N} \sum_{n=1}^N \left(\frac{\tau_{\varepsilon n}}{\tau_{\sigma n}} - 1 \right) \exp(-t / \tau_{\sigma n}) \right].$$

This definition is equivalent to formula (18) for the creep function.

For N mechanisms interacting sequentially, one can write by analogy:

$$J = \sum_{n=1}^N \left[\frac{1}{k_{2n}} + \frac{1}{k_{1n}} - \frac{1}{k_{1n}} \exp(-k_{1n} t / \eta_n) \right] \theta(t).$$

The scheme of interactions is equivalent to a sequential scheme with equal values $2/k = \frac{1}{N} \sum_{n=1}^N (1/k_{1n} + 1/k_{2n})$ for elastic elements.

Defining the relaxation times for each mechanism as

$$\tau_{\varepsilon n} = \eta_n / k_{1n}, \quad \tau_{\sigma n} = \eta_n / (k_{1n} + k_{2n}),$$

one obtains $\frac{1}{k_{1n}} = \frac{2}{k} \left(1 - \frac{\tau_{\sigma n}}{\tau_{\varepsilon n}} \right)$, and

$$J = \frac{2N}{k} \left[1 - \frac{1}{N} \sum_{n=1}^N \left(1 - \frac{\tau_{\sigma n}}{\tau_{\varepsilon n}} \right) \exp(-t / \tau_{\varepsilon n}) \right]$$

what gives formula (14) for the creep function.

Appendix "B"

Model equations for N dissipation mechanisms

By expanding the time derivative in the convolution in (5), with using the formula (14), one can get:

$$\dot{\sigma}_{ij} = L_{ij} - \frac{1}{N} \sum_{n=1}^N \tau_n (m_n - \dot{\sigma}_{ij}), \quad (B1)$$

where $m_n = \frac{1}{\tau_{\varepsilon n}} \exp(-t / \tau_{\varepsilon n}) \theta(t) * \dot{\sigma}_{ij}$.

By taking the time derivative of m_n , one can get:

$$\tau_{\varepsilon n} \dot{m}_n = -m_n + \dot{\sigma}_{ij}. \quad (B2)$$

Substituting this equation into (B1) gives:

$$\dot{M}_{ij} = \dot{\sigma}_{ij} - L_{ij}, \quad (B3)$$

where $M_{ij} = \frac{1}{N} \sum_{n=1}^N (\tau_{\varepsilon n} - \tau_{\sigma n}) m_n$.

The equation (B1) can be rewritten in the form

$$\frac{1}{N} \sum_{n=1}^N [(1 - \tau_n) \dot{\sigma}_{ij} = L_{ij} - \tau_n m_n] \quad (B4)$$

As it follows from (6), the equality in brackets inside the sum of (B4) is valid for each dissipation mechanism, i.e., for each value of index n . Therefore, one can multiply it by $\tau_{\varepsilon n}$ inside the sum what gives the equation:

$$\bar{\tau}_{\sigma} \dot{\sigma}_{ij} = \bar{\tau}_{\varepsilon} L_{ij} - M_{ij} \quad (B5)$$

Defining $R_{ij} = M_{ij} / (\bar{\tau}_{\varepsilon})$, one obtains equations (15) and (16) from (B5) and (B3).

In the case of parallel mechanisms, the time derivative in the convolution in (17) is expanded with using the formula (18) that gives:

$$\dot{\sigma}_{ij} = L_{ij} - \frac{1}{N} \sum_{n=1}^N \tau_{1n} (m_{1n} - L_{ij}), \quad (B6)$$

where $m_{1n} = \frac{1}{\tau_{\sigma n}} \exp(-t / \tau_{\sigma n}) \theta(t) * L_{ij}$.

By taking the time derivative of m_{1n} , one can get:

$$\tau_{\sigma n} \dot{m}_{1n} = -m_{1n} + L_{ij} \quad (B7)$$

Substituting this equation into (B6) gives equation (B3) in which $M_{ij} = \frac{1}{N} \sum_{n=1}^N (\tau_{\varepsilon n} - \tau_{\sigma n}) m_{1n}$.

The equation (B6) can be rewritten in the form

$$\frac{1}{N} \sum_{n=1}^N [\dot{\sigma}_{ij} = L_{ij} + \tau_{1n} L_{ij} - \tau_{1n} m_n] \quad (B8)$$

The equality in brackets inside the sum of (B8) is valid for each dissipation mechanism, i.e., for each value of index n . Therefore, one can multiply it by $\tau_{\sigma n}$ inside the sum what gives the equation (B5). As above, (B3) and (B5) lead to (15) and (16) by defining $R_{ij} = M / (\bar{\tau}_{\varepsilon})$.

In the case 3), by the same way, one can obtain the equation (B3) with the definition

$$M_{ij} = \frac{1}{N} \left[\sum_{n=1}^{N_1} (\tau_{\varepsilon n} - \tau_{\sigma n}) m_n + \sum_{n=1}^{N_2} (\tau_{\varepsilon n} - \tau_{\sigma n}) m_{1n} \right].$$

For the first group, the equation

$$\sum_{n=1}^{N_1} [(1 - \tau_n) \dot{\sigma}_{ij} = L_{ij} - \tau_n m_n] \quad (B9)$$

is valid which can be multiplied by $\tau_{\varepsilon n}$ inside the sum, and for the second group, the equation

$$\sum_{n=1}^{N_2} [\dot{\sigma}_{ij} = L_{ij} + \tau_{1n} L_{ij} - \tau_{1n} m_{1n}] \quad (B10)$$

is valid which can be multiplied by $\tau_{\sigma n}$ inside the sum. After these multiplications, the sum of (B9), and (B10), divided by N , gives again the equation (B5).

Unfortunately, in the case of N parallel mechanisms, some authors use instead of (17) and (18) the widely known formulae (Carcione *et al.*, 1988; Carcione, 1993; Robertsson *et al.*, 1994; Xu and McMechan, 1998; Komatitsch and Tromp, 2002, Mikhailenko *et al.*, 2003):

$$\begin{aligned} \dot{\sigma}_{ij} &= \dot{\phi}_2 * L_{ij} \\ \phi_2(t) &= [1 + \sum_{n=1}^N \tau_{1n} \exp(-t / \tau_{\sigma n})] \theta(t), \end{aligned}$$

In this case, one will obtain the equation (B3) with definition $M_{ij} = \frac{1}{A} \sum_{n=1}^N \tau_{1n} m_{1n}$, where $A = \frac{1}{N} \sum_{n=1}^N \frac{1}{\tau_{\sigma n}}$.

Instead of (B5), one will obtain the similar equation:

$$\dot{\sigma}_{ij} = (1 + NB) L_{ij} - A M_{ij}, \quad (B11)$$

where $B = \frac{1}{N} \sum_{n=1}^N \tau_{1n}$. In essence, A and B are average values.

Scarcely likely, (B11) looks better than (B5). Equation (B11) depends explicitly on number of relaxation mechanisms N , but (B5) does not. For example, it is easily seen in the case of proportional values $\tau_{\sigma n} = 2\tau_{\varepsilon n}$ for all relaxation mechanisms.

Independence on N of (B5) is more correct from the point of view of Physics. Therefore, I use and recommend the creep functions ϕ , and ϕ_1 , but not ϕ_2 .

Appendix "C" Travel time estimation for multilayered media

Suppose that there are n layers above the target one. Then (see Fig. 2),

$$x_0 = \sum_{i=1}^n z_i \operatorname{tg}(\beta_i), \quad (\text{C1})$$

where z_i is the thickness of i -th layer, and β_i is the incidence angle in it.

From Snell's law, $a_0 = \frac{\sin(\beta_i)}{V_i}$ is a constant, and

from (C1), one can derive a nonlinear equation for obtaining it (V_i is the ray velocity):

$$x_0 = a_0 \sum_{i=1}^n \frac{z_i V_i}{\sqrt{1 - a_0^2 V_i^2}} \quad (\text{C2})$$

Consequently, knowing a_0 from (C2), one can calculate a half of the travel time for upper ray:

$$t_0 = \sum_{i=1}^n \frac{z_i}{V_i \sqrt{1 - a_0^2 V_i^2}} \quad (\text{C3})$$

By analogy, for the down ray, one can write:

$$x = a \sum_{i=1}^n \frac{z_i V_i}{\sqrt{1 - a^2 V_i^2}} \quad (\text{C4})$$

where $a = \frac{\sin(\alpha_i)}{V_i}$, and α_i is the incidence angle for it.

The half of the travel time for down ray in the n upper layers

$$t_1 = \sum_{i=1}^n \frac{z_i}{V_i \sqrt{1 - a^2 V_i^2}} \quad (\text{C5})$$

From definitions,

$$0.5\Delta t = t_1 - t_0 + \frac{z}{V \cos(\alpha)} \quad (\text{C6})$$

where z , V , and α without indexes belong to the target layer.

From (C6) with (C4), using substitution $w = x_0 - x$, one finds out a nonlinear equation for calculating value a :

$$t_0 + 0.5\Delta t = t_1 + \frac{a(z^2 + w^2)}{w}$$

Finally, knowing a , one calculates t_1 from (C5), and the travel time in the target layer

$$\tau_0 = 2(t_0 - t_1) + \Delta t$$

Bibliography

- Blanch J.O, Robertsson J.O.A., Symes W.W., 1995, Modeling of constant Q: Methodology and algorithm for an efficient and optimally inexpensive viscoelastic technique, *Geophysics*, 60, 1, p.176-184.
- Carcione J.M., 1993, Seismic modeling in viscoelastic media, *Geophysics*, 58, 1, p.110-120.
- Carcione J.M., 1995, Constitutive model and wave equations for linear, viscoelastic, anisotropic media, *Geophysics*, 60, 2, p.537-548.
- Carcione J.M., Kosloff D., Kosloff R., 1988, Wave propagation in a linear viscoelastic medium, *Geophysical Journal*, 95, p.597-611.
- Collino F., Tsogka C., 2001, Application of the PML Absorbing Layer Model to the Linear Elastodynamic Problem in Anisotropic Heterogeneous Media, *Geophysics*, 66, 1, 294-307.
- Dasgupta R., Clark R.A., 1998, Estimation of Q from surface seismic reflection data. *Geophysics*, 63, 2120-2128.
- Emmerich H., 1992, PSV-wave propagation in a medium with local heterogeneities: a hybrid formulation and its application, *Geophys. J. Int.*, 109, 54 - 64.
- Futterman W.I., 1962, Dispersive body waves. *J. Geophys. Res.*, 67, 5279-5291.
- Knopoff L., 1964, Q. *Revs. Geophys.*, 2, 625-660.
- Komatitsch D., Tromp J., 2002, Spectral-element simulations of global seismic wave propagation - I. Validation. *Geophys. J. Int.*, 149, p.390 - 412.
- Liu H.-P., Anderson D.L., Kanamori H., 1976, Velocity dispersion due to anelasticity;

- implications for seismology and mantle composition, *Geophys. J. R. Astr. Soc.*, 47, 41-58.
- Lomnitz C., 1957, Linear dissipation in solids. *J. Appl. Phys.*, 28, 201-205.
- Mikhailenko B., Mikhailov A., Reshetova G., 2003, Spectral Laguerre method for viscoelastic seismic modeling. *Mathematical and Numerical Aspects of Wave Propagation WAVES 2003*, Springer-Verlag, p.891-896.
- Moczo P., Bystricky E., Kristek J., Carcione J.M., Bouchon M., 1997, Hybrid modeling of P-SV seismic motion at inhomogeneous viscoelastic topographic structures, *Bulletin of the Seismological Society of America*, 87, 5, p.1305-1323.
- Quan Y., Harris J.M., 1993, Seismic attenuation tomography based on centroid frequency shift, *Exp. Abs.*, 63-rd Ann. Internat. SEG Mtg., Washington, Paper BG2.3.
- Robertsson J.O.A., Blanch J.O., Symes W.W., 1994, Viscoelastic finite-difference modeling. *Geophysics*, 59, 9, p.1444 - 1456.
- Sabinin V., Chichinina T., Ronquillo Jarillo G., 2003, Numerical model of seismic wave propagation in viscoelastic media. *Mathematical and Numerical Aspects of Wave Propagation WAVES 2003*, Springer-Verlag, p.922-927.
- Tonn R., 1991, The determination of the seismic quality factor Q from VSP data: a comparison of different computational methods, *Geophysical Prospecting*, 39, 1-37.
- Virieux J., 1986, P-SV wave propagation in heterogeneous media: Velocity-stress finite-difference method. *Geophysics*, 51, 4, p.889 - 901.
- Xu T., McMechan G.A., 1995, Composite memory variables for viscoelastic synthetic seismograms. *Geophys. J. Int*, 121, p.634 - 639.
- Xu T., McMechan G.A., 1998, Efficient 3-D viscoelastic modeling with application to near-surface data. *Geophysics*, 63, 2, p.601 - 612.

Gas Hydrates in the southern Jalisco subduction zone as evidenced by bottom simulating reflectors in Multichannel Seismic Reflection Data of the 2002 BART/FAMEX campaign

William L. Bandy* and Carlos A. Mortera Gutiérrez

Received: April 25, 2012; accepted: August 07, 2012; published on line: September 28, 2012

Resumen

Evidencia de la presencia de hidratos de gas en forma de un reflector que simula el fondo marino (BSR) es observado en un perfil sísmico multicanal en el talud continental del área sur de la zona de subducción en Jalisco, frente a Manzanillo, México. Los reflectores son encontrados a 0.4 segundos (en el tiempo de viaje doble) bajo el reflector del fondo marino y se extiende a lo largo de 7 km del perfil. Este resultado aunado a otros resultados previos en la parte norte de la zona de subducción de Jalisco sugiere que los hidratos de gas pudieran existir en la región del talud continental de toda la zona de subducción de Jalisco, sin embargo se necesitan más datos de reflexión sísmica para verificar esta aseveración.

Palabras clave: Hidratos de Metano, BSR, Zona de Subucción de Jalisco, reflexión Sísmica.

Abstract

Evidence, in the form of bottom simulating reflectors (BSRs), for gas hydrates is observed on a multichannel seismic reflection profile in the continental slope area of the southern Jalisco Subduction Zone, off Manzanillo, Mexico. The reflectors are found at 0.4 sec (two-way travel time) below the seafloor reflector and extend for about 7 km along the profile. This result along with previous results in the northern part of the Jalisco Subduction Zone suggests that gas hydrates may exist in the continental slope region of the entire Jalisco Subduction Zone, however, more seismic reflection data needs to be collected to verify this assertion.

Key words: gas hydrate, BSR, Jalisco subduction zone, seismic reflection.

W. L. Bandy*
Departamento de Geomagnetismo y Exploración
Instituto de Geofísica
Universidad Nacional Autónoma de México
Ciudad Universitaria
Delegación Coyoacan, 04510
México D.F., México
**Corresponding autor: bandy@geofisica.unam.mx*

C. A. Mortera Gutiérrez
Departamento de Sismología
Instituto de Geofísica
Universidad Nacional Autónoma de México
Ciudad Universitaria
Delegación Coyoacán, 04510
México D.F., México

Introduction

Gas hydrates trapped within the sediments of continental slopes are thought to represent a significant worldwide, source of energy for the future (e.g. Max *et al.*, 2006; Allison and Ray, 2007). Although gas hydrates have been recovered in sediment cores, their presence is normally inferred from observations of bottom simulating reflections (BSRs) on seismic reflection profiles (e.g. Stoll *et al.*, 1971; Hyndman and Spence, 1992; Laberg *et al.*, 1998; Posewang and Mienert, 1999). Presently, there is a scarcity of published seismic reflection data along the Pacific margin of Mexico from which one could adequately analyze the gas hydrate potential of this region. However, BSRs have been reported in several areas including off the Pacific margin of Baja California Sur (Cruz-Melo, 2008) and along the Middle America Trench off southern Mexico (Shipley *et al.*, 1979). Gas hydrates were observed off Acapulco in cores from holes 490, 490 and 492 collected during Leg 66 of the Deep Sea Drilling Project (Shipley and Didyk, 1981). In the Jalisco Subduction Zone, at which the Rivera plate subducts beneath the North American plate (Figure 1), a few single channel seismic reflection profiles have been presented by Ross and Shor (1965), Bourgois *et al.* (1988), Bourgois and Michaud (1991), Bandy (1992), Khutorskoy *et al.* (1994), and Michaud *et al.* (1996). Khutorskoy *et al.* (1994) observed several BSRs in their data

located within the continental slope area in the offshore extension of the Tecoman Graben within the southern Colima Rift. Multichannel data are particularly scarce in the Jalisco Subduction Zone where the only published multichannel data are those collected during the 1996 CORTES P96 campaign (Minshull *et al.*, 2005; Bartolomé *et al.*, 2011) and the 2002 BART/FAMEX campaign (Bandy *et al.*, 2005). Minshull *et al.* (2005) and Bartolomé *et al.* (2011) report the presences of BSRs in the northern part of the Jalisco Subduction Zone off Puerto Vallarta between 20° and 20.5°N. Thus, there is evidence to suggest that the Pacific margin of Mexico may contain significant gas reserves in the form of gas hydrates, However, much of the margin has yet to be explored so that a full evaluation of this potential cannot presently be determined.

In this paper we present some previously unreported evidence for gas hydrate accumulations in the southernmost part of the Jalisco subduction zone off Manzanillo found on a multichannel seismic reflection profile collected during the 2002 BART/FAMEX campaign of the N/O L'Atalante. On this profile, BSRs are clearly observed in the continental slope region. These data and observations should be of value to other investigators interested in evaluating the gas hydrate potential of the Jalisco Subduction Zone in particular and worldwide distribution of gas hydrates in general.

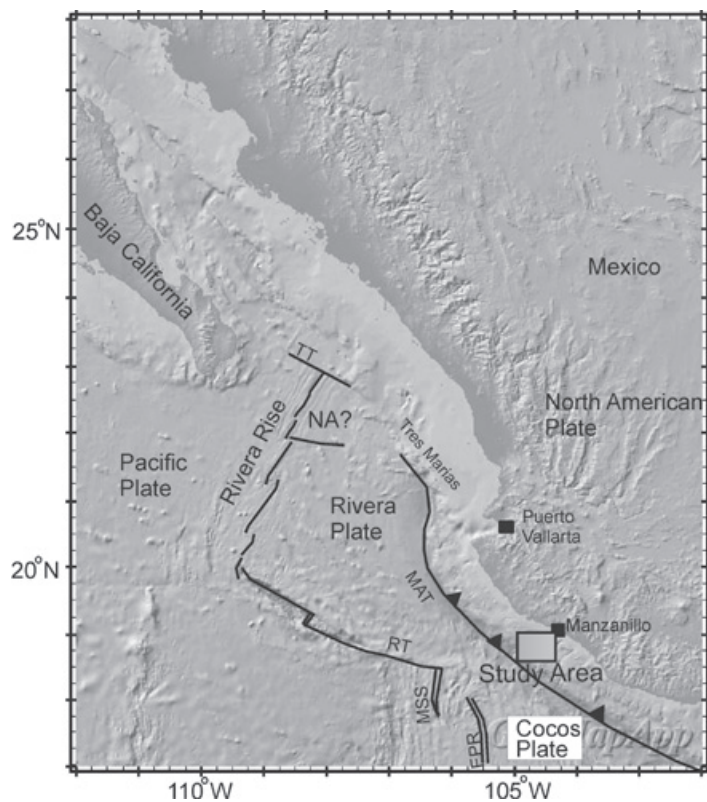


Figure 1. Study area location. Abbreviations are: MAT=Middle America Trench; NA= North American Plate; MSS=Moctezuma Spreading Segment; EPR=East Pacific Rise; TT=Tamayo Transform; RT=Rivera Transform. Background image from GeoMapApp.

Geologic setting

The Jalisco Subduction Zone comprises the northernmost part of the Middle America Trench (MAT), north of Manzanillo, Colima (Figure 1). This zone is an active continental margin at which the Rivera plate is subducting beneath the North American plate. The offshore part of this continental margin, from the coastline to the trench axis, is on average 80 km wide. Although no drilling has been done in the offshore area of this margin, seismic reflection data indicate that, offshore, the subsurface consists of a thick sequence of marine sediments along the entire margin (Ross and Shor, 1965; Bourgois *et al.*, 1988; Bourgois and Michaud 1991; Bandy, 1992; Khutorskoy *et al.* 1994; Michaud *et al.*, 1996; Minshull *et al.*, 2005; Bandy *et al.*, 2005; Bartolomé *et al.*, 2011). In the southernmost part of the Jalisco Subduction Zone, within the Tecoman trough and over the Manzanillo Horst (Figure 2) these sediments are observed in submersible dives to unconformably overlie pre-Eocene plutonic rocks: granodiorites and gabbros (Mercier de Lépinay *et al.*, 1997).

Bottom simulating reflectors and gas hydrates

The association between BSRs and gas hydrate accumulations is illustrated in Figure 3. Briefly, gas hydrates form within the uppermost part of the sedimentary column within the "gas hydrate

stability zone", which is the zone within which the physical conditions within the sediments (i.e. pressure, temperature, interstitial water salinity, etc.) allow for the formation of gas hydrates. Below this zone the physical conditions do not permit hydrate formation, consequently, the gas is in a free state and collects within the pore spaces of the sediments. Since the gas hydrates form a seal, the upward migrating free gas is trapped at the base of the gas hydrate stability zone. This free gas lowers the acoustic impedance of the gas charged sediments below the base of the hydrates, which normally results in a negative acoustic impedance contrast as well as an increase in the absolute value of the acoustic impedance contrast. Thus, the seismic reflections (BSRs) from the base of the gas hydrate stability zone are expected to be of high amplitude and to have a polarity that is the reverse of the down-going seismic pulse.

As the name implies, a BSR in general mimics the shape of the seafloor reflector (Stoll *et al.*, 1971). The depth of the base the gas-hydrate stability zone is controlled by temperature, pressure, gas chemistry and salinity of the interstitial fluids; therefore if these parameters do not vary drastically within a given area, then the depth of the base of the hydrate layer below the seafloor should remain fairly constant and hence the BSR should mimic the seafloor reflector (Zatsepena and Buffer, 1997; Max, *et al.*, 2006).

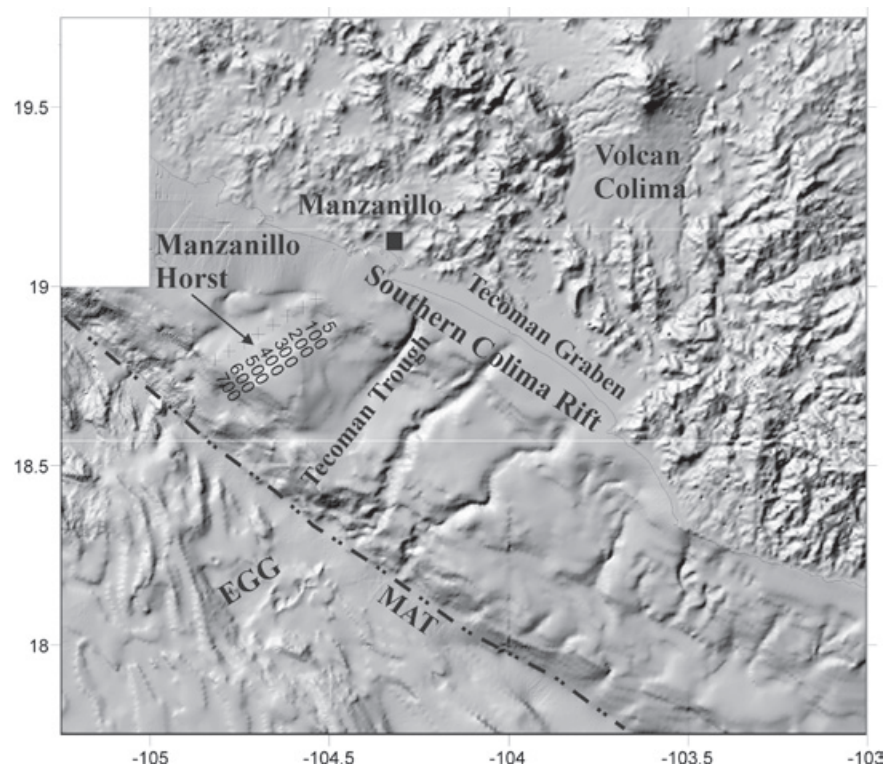


Figure 2. Relief map illustrating location of Seismic reflection profile shown in Figure 4. Numbers refer to CMP locations. Abbreviations are: EGG=El Gordo Graben; MAT=Middle America Trench. (Modified from Bandy *et al.*, 2005).

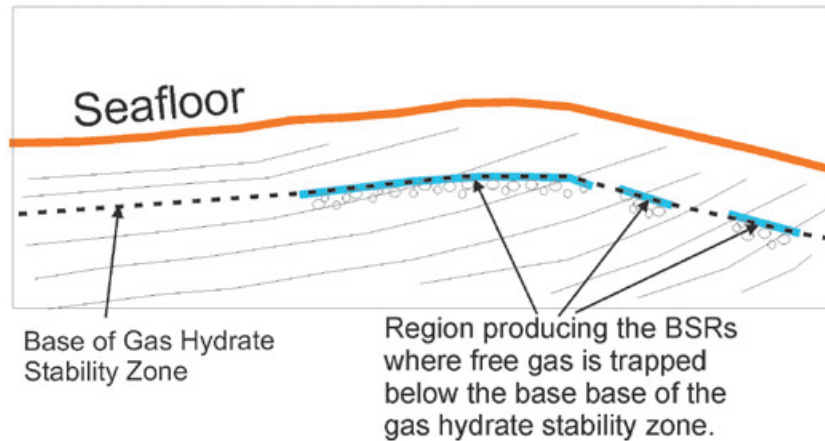


Figure 3. Drawing illustrating how the BSR is produced. Note how the BSR (Blue lines) can cut across the sediment layers (thin lines). Circles represent free gas within the sediments.

In summary, a BSR should exhibit the following characteristics:

- (1) It should exhibit high amplitudes,
- (2) It should have reverse polarity (i.e. the reflected pulse should be 180 degrees out of phase with that of the down-going pulse).
- (3) It should mimic the shape of the seafloor reflector.

Another distinguishing characteristic of the BSR is that in areas where the sediment layers are inclined relative to the seafloor, the BSR will cut across the reflections from the sediment layers. For more details about the underlying physics of gas hydrates and BSRs, the reader is referred to one of the many publications that deal in depth with this subject, such as Max *et al.* (2006).

Data

The seismic reflection data used in this study were collected along a profile (see Figure 2 for profile location) during the BART/FAMEX campaigns conducted during April 2002 aboard the N/O L'Atalante. Three-fold data were acquired employing 300 in.³ Gas injection (GI) guns tuned in harmonic mode and a hydrophone streamer with 6 hydrophone groups (48 hydrophones per group) spaced 50 m apart. The spacing between stacked traces is 25 m. The data was sampled at 4 ms and recorded using SEG-Y format. During processing, the distance between Common Mid Point (CMP) locations was set at 50 m.

The data was processed using the following processing sequence:

1. Geometry assignment
2. Spherical divergence correction

3. 10-70 Hz band-pass filter with a high and low rolloff rate of 18 dB/octave
4. Normal Moveout (NMO) correction
5. Stack
6. Migrated using the Gazdag phase-shift method (Gazdag, 1978) employing a constant velocity of 1500 m/s.

Results and discussion

The upper continental slope along the profile (Figure 4) consists of a sequence of relatively undisturbed sediments that were deposited on a subsiding, seaward tilting seafloor (Bandy *et al.*, 2005). This unit extends down to water depths of about 750 m. No BSRs are observed in this area. At the seaward end of this unit (at CMP 131), the water depth increases rapidly to about 1200 m and a mid-slope terrace is present between CMPs 195 to 720. Water depths gradually increase from 1200m to 1500m seaward across this terrace. The terrace is disrupted in its northeastern part (between CMPs 250 to 551) by a series of anticlines. No BSRs are clearly observed in this area; however, the complex deformation might be masking these reflectors if present.

Seaward of CMP 551 the terrace is underlain by relatively undisturbed sediments typical for a mid-slope terrace (Figures 5 and 6). A prominent BSR is present in the undisrupted SW part of the terrace between CMP 580 to CMP 720 at a depth of about 400ms TWTT (two-way travel time) below the seafloor reflection. This represents a distance of about 7 km. The BSR is of high amplitude, it cuts across the more steeply dipping reflectors from the sedimentary units, and the reflector mimics the seafloor (i.e. it consistently lies at about 400 ms TWTT below the seafloor). Thus, it clearly exhibits three of the requirements for being a BSR. Also, the polarity of the BSR (peak-

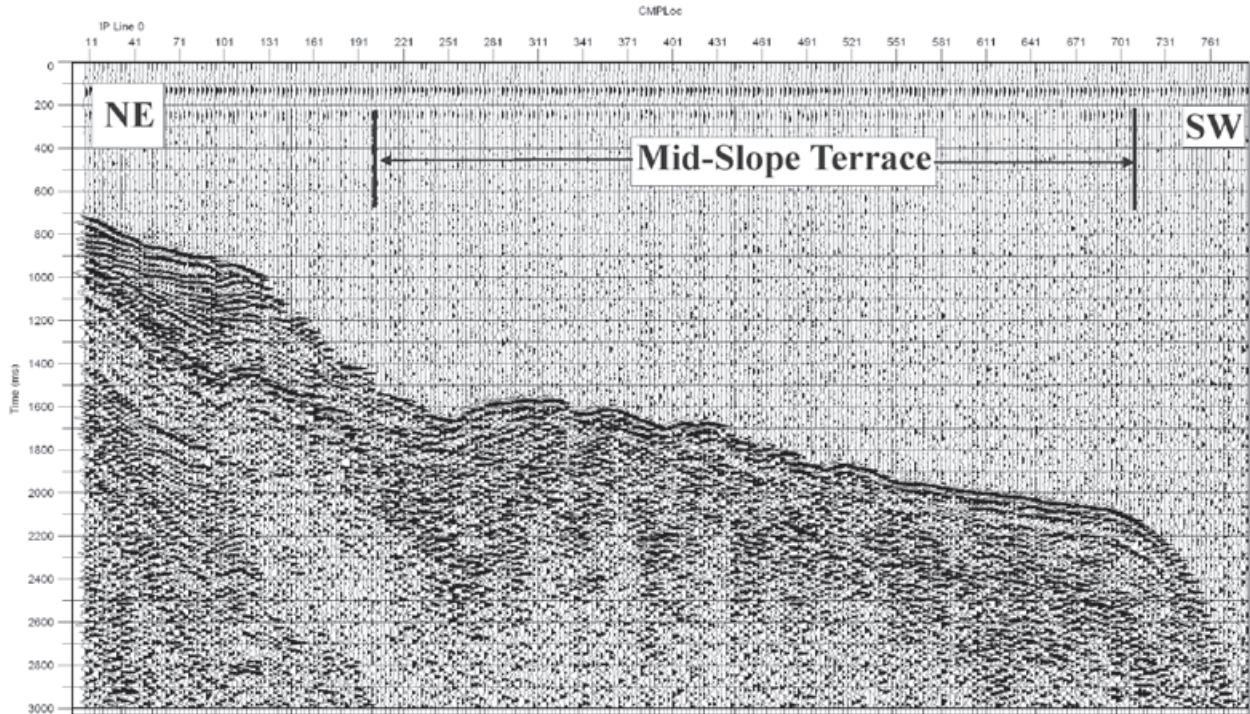


Figure 4. Seismic reflection profile illustrating the character of the mid-slope terrace off Manzanillo. Every 10th trace is plotted. The Middle America Trench is located to the SW. Time plotted is two-way travel time (modified from Bandy *et al.*, 2005).

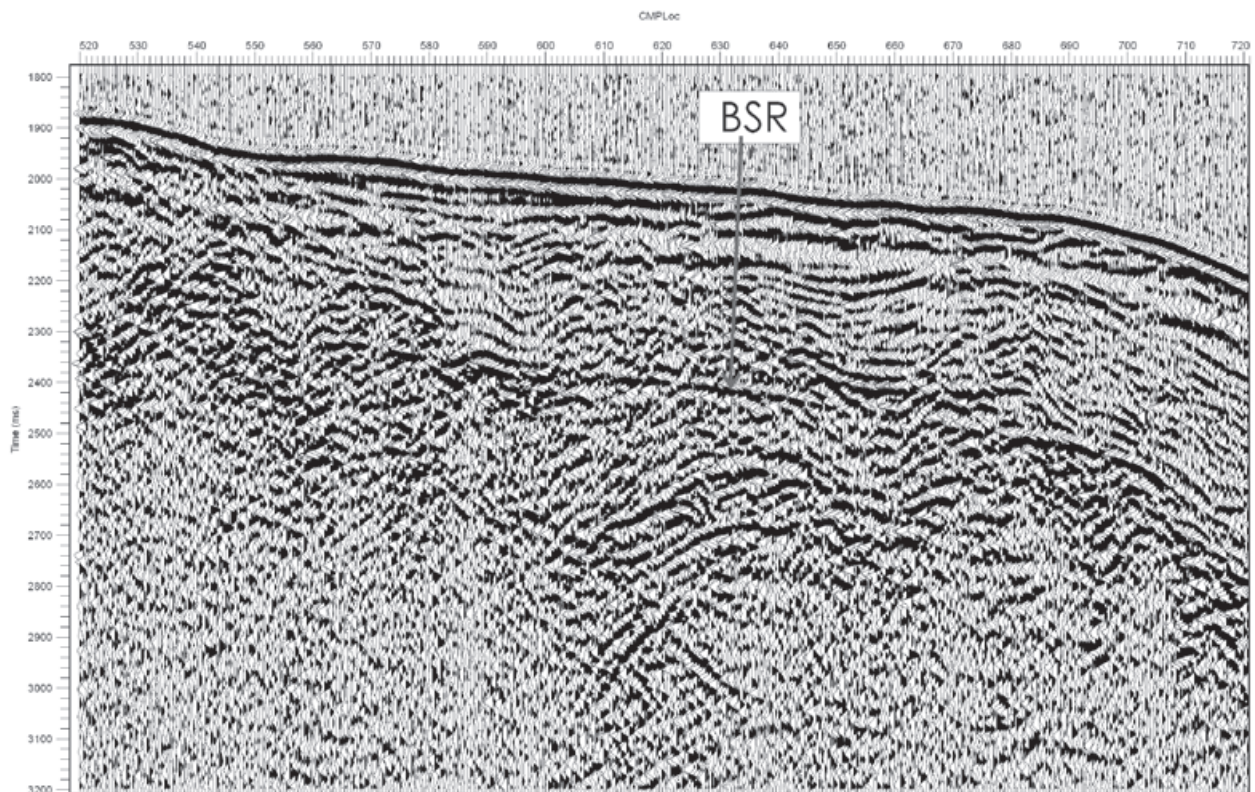


Figure 5. Uninterpreted blowup of the seaward part of the profile shown in Figure 4 illustrating the BSR.

trough-peak) appears to be 180 degrees out of phase with the seafloor reflector (trough-peak-trough), however this is not entirely clear.

Trying to quantify the amount of gas in the sediments is quite difficult. However, one can obtain a very rough estimate of the volume of gas present in the outer part of the mid slope terrace over the Manzanillo Horst as follows. The width of the Manzanillo Horst is about 20 km and the BSR covers the outer 7 km of the horst. Now, assuming that the p-wave velocity in the sediments is 2 km/sec, and assuming that the gas hydrates extend from the seafloor to the BSR, then the thickness of the gas hydrate layer can be estimated to be 400 meters. Thus, the volume of sediments containing the gas is 66 km³. Assuming that the sediments have a porosity of 10% (a value which may be quite low given that these sediments are most likely unconsolidated) then the volume of gas is estimated to be 6.6 km³. One needs to add to this value the volume of the free gas trapped beneath the base of the gas hydrates, unfortunately there is no way to estimate this from the seismic data as even a very small amount of gas in the pore space will produce a high amplitude reflection (e.g., Domenico, 1977).

Our results provide additional seismic evidence for significant accumulations of gas hydrates in the continental slope region on the southern part of the Jalisco Subduction Zone. This result in conjunction with the BSRs observed in the continental slope region of the northern part of the Jalisco Subduction Zone suggests that the continental slope area along the entire Jalisco Subduction Zone may contain significant accumulations of gas hydrates. Therefore, a more extensive seismic reflection survey of the rest of the Jalisco Subduction Zone may be warranted to fully evaluate the potential gas reserves in this area.

Conclusions

- (1) In the continental slope area of the Jalisco Subduction Zone off Manzanillo, the multichannel data of the 2002 BART/FAMEX campaign reveal a high amplitude, possibly reversed polarity, reflector that mimics the seafloor reflector and cuts across the more steeply dipping sedimentary reflectors.
- (2) The characteristics of this reflector are consistent with it being a BSR, and thus, strongly indicate the presence of gas hydrates.

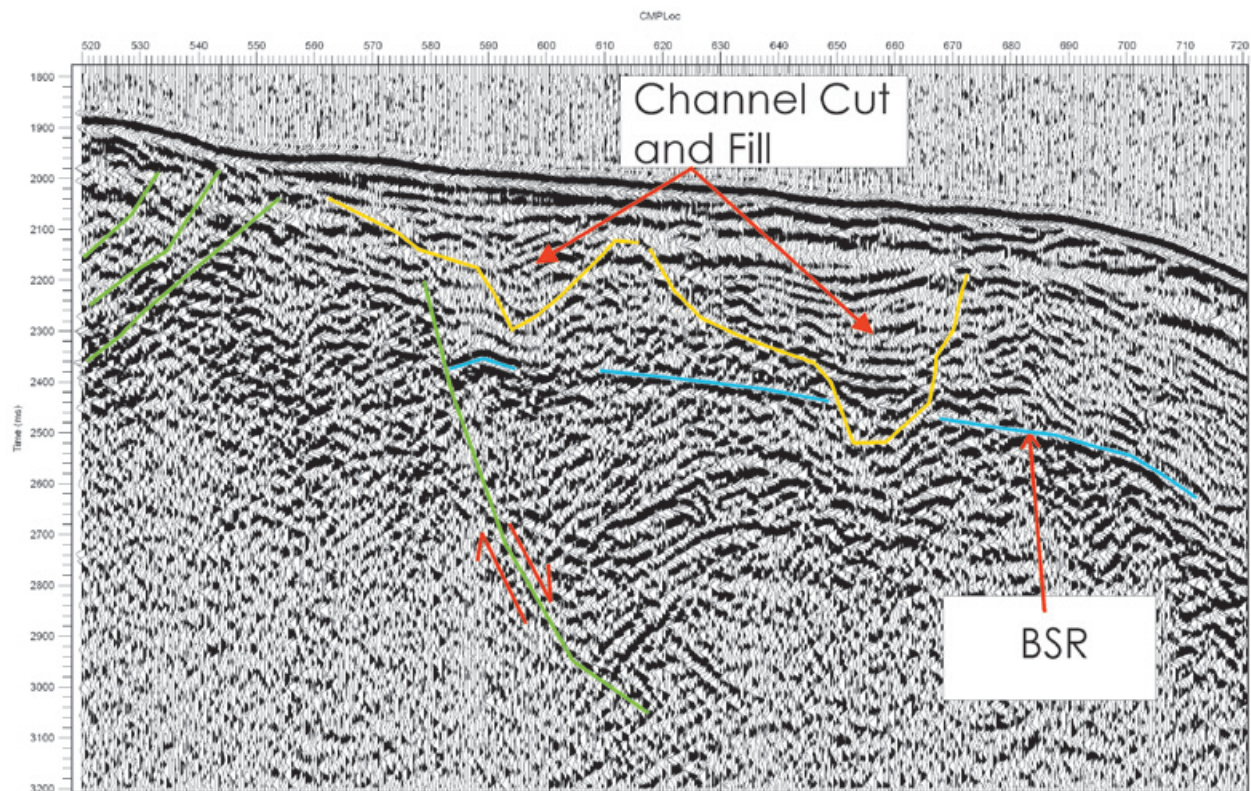


Figure 6. Interpretation of the profile shown in Figure 5. Green line marks faults, blue line is the BSR, and yellow lines mark unconformities interpreted to be the base of channel fill sequences.

- (3) The BSR consistently lies at 400 ms (TWTT) below the seafloor reflector and extends for a distance of 7 km along the profile, which suggests that a substantial accumulation of gas hydrates (greater than 6.6 km³) may be present in this area.
- (4) Our results, in conjunction with the BSRs observed in the northern part of the Jalisco Subduction Zone during the CORTES-96 campaign, indicate that a more extensive seismic reflection survey is warranted and needed to fully evaluate the gas potential of the continental shelf area of the Jalisco Subduction Zone.

Acknowledgments

We thank the captain and crew of the N/O L'Atalante and the onboard technical staff for their assistance in the collection of the data during the BART /FAMEX cruise. Financial support was provided by Centre National de la Recherche Scientifique (CNRS), and by CONACyT grants 36681-T, #50235, and UNAM DGAPA grants IN104707, IN108110, IN117305, IN114410 and IN102507. We thank the two anonymous reviewers for their comments which helped to improve the manuscript.

Bibliography

- Allison, E., and Ray, B., 2007, Methane Hydrate: Future Energy within our grasp, a review, 20 pp., US Department of Energy, Washington, D.C. 20585.
- Bandy, W.L., 1992, Geological and Geophysical Investigation of the Rivera-Cocos plate boundary: implications for plate fragmentation. Ph.D. dissertation, Texas A&M University, College Station, 195 p.
- Bandy, W.L., and 16 others, 2005, Subsidence and strike-slip tectonism of the upper continental slope off Manzanillo Mexico. *Tectonophysics*, 398, 115-140.
- Bartolomé, R., Dañobeitia, J., Michaud, F., Córdoba, D., and Delgado-Argote, L.A., 2011, in Geodynamics of the Mexican Pacific Margin, Bandy, W.L., Taran, Y., Mortera Gutiérrez, C., and Kostoglodov, V. (eds.), Pageoph Topical Volumes, Birkhäuser, 123-139, ISBN 978-3-0348-0196-6.
- Bourgeois, J., and Michaud, F., 1991, Active fragmentation of the North American plate at the Mexican Triple Junction Area off Manzanillo (Mexico). *Geomarine Letters*, 11, 59-65.
- Bourgeois, J. and 11 others, 1988, Fragmentation en cours du continent Nord Américain: les frontières sous marines du bloc de Jalisco (Mexico). *C.R. Acad. Sc.Paris*, 307 II, 1121-1130.
- Cruz Melo, C.E., 2008, Análisis de la presencia de hidratos de metano con los horizontes sísmicos BSR al suroeste de la Península de Baja California, México. Tesis de Maestría, Instituto de Geofísica, UNAM, Mexico, D.F., 110pp.
- Domenico, S.N., 1977, Elastic properties of unconsolidated porous sand reservoirs. *Geophysics*, 42, 1339-1368.
- Gazdag, J., 1978, Wave-equation migration by phase-shift, *Geophysics*, 43, 1342-1351.
- Hyndman, R.D., and Spence, G.D., 1992; A seismic study of methane hydrate marine bottom simulating reflectors. *J. Geophys. Res.*, 97, 6683-6698.
- Khutorskoy, M.D., Delgado-Argote, L.A., Fernández, R., Kononov, V.I. and Polyak, B.G., 1994, Tectonics of the offshore Manzanillo and Tecpan basins, Mexican Pacific, from heat flow, bathymetric and seismic data. *Geofísica Internacional*, 33, 161-185.
- Laberg, J.S., Andreassen, K., and Knutsen, S.-M., 1998, Inferred gas hydrate on the Barents Sea Shelf – a model for its formation and volume estimate. *Geo-Marine Letters*, 18, 26-33.
- Max, M.D., Johnson, A.H., and Dillon, W.P., 2006, Economic Geology of Natural Gas Hydrates, *Springer*, The Netherlands, 341pp.
- Mercier de Lépinay, B., and 11 others, 1997, Large Neogene subsidence event along the Middle America Trench off Mexico (18° -19°N): Evidence from submersible observations, *Geology*, 25, 387-390.
- Michaud, F., Mercier de Lépinay, B., Bourgeois, J., and Calmus, T., 1996, Evidence for active extensional tectonic features within the Acapulco trench fill at the Rivera-North America plate boundary. *C.R. Acad. Sc.Paris*, t. 321 série IIa, 521-528.
- Minshull, T.A., Bartolomé, R., Byrne, S., and Dañobeitia, J., 2005, Low heat flow from young oceanic lithosphere at the Middle America Trench off Mexico. *Earth and Planetary Science Letters*, 239, 33-41.

- Posewang, J., and Mienert, J., 1999, High-resolution seismic studies of gas hydrates west of Svalbard. *Geo-Marine Letters*, 19, 150-166.
- Ross, D.A., and Shor Jr., G.G., 1965, Reflection profiles across the Middle American Trench, *J. Geophys. Res.* 70, 5551-5572.
- Shipley, T.H., and Didyk, B.M., 1981, Occurrence of methane hydrates offshore southern Mexico, in Watkins, J.S., Moore, J.C., *et al.*, Init. Repts. *DSDP*, 66: Washington (U.S. Govt. Printing Office), 547-556.
- Shipley, T.H. *et al.*, 1979, Seismic reflection evidence for widespread occurrence of possible gas-hydrate horizons on continental slopes and rises. *Am. Assoc. Pet. Geol. Bull.*, 63, 2204-2213.
- Stoll, R.D., Ewing, J., and Bryan, G.M., 1971, Anomalous velocities in sediments containing gas hydrates. *J. Geophys. Res.*, 76, 2090-2094.
- Zatsepena, O.Y., and Buffer, B.A., 1997, Phase equilibrium: Implications for the formation of hydrate in the deep seafloor *Geophys. Res. Lett.*, 24, 1567-1570.